Magnetisation Transfer Effects at Ultra High Field MRI

By

Simon Michael Shah, M.Sci

The University of Nottingham

UNITED KINGDOM · CHINA · MALAYSIA

Thesis submitted to the
University of Nottingham
for the degree of Doctor of Philosophy

December 2016

Abstract

Increased signal to noise ratio in ultra high field Magnetic Resonance Imaging (MRI) has allowed the development of quantitative imaging techniques and new contrast mechanisms, such as Chemical Exchange Saturation Transfer (CEST) to be probed.

The development of CEST contrast imaging has involved overcoming a number of technical challenges associated with ultra high field MRI. The B_1 transmit field was, and still is, a major challenge. Presented in this thesis, the B_1 transmit field in regions of low B_1 are improved with the use of dielectric pads and a simulation study shows that the overall B_1 transmit field homogeneity is significantly improved when multi-transmit slice-selective RF spokes pulse sequences are used.

Multiple methods have been developed to quantify the chemical exchange from slow exchanging proton pools seen in CEST contrast imaging. However, magnetisation transfer (MT) from the macromolecular bound pool contaminates current quantification methods, and presented in this thesis is a method whereby the CEST and MT are simultaneously saturated using dual frequency saturation pulses, allowing the CEST contrast in z-spectra to be separated from the MT and to enhance visualisation of the CEST effects.

Despite the considerable interest in CEST, only one study has probed the CEST effects in blood, and interestingly high levels of CEST signals can be observed from the superior sagittal sinus. To investigate these effects, z-spectra from *ex vivo* blood samples considering the effects of oxygenation, haematocrit levels and cell structure were quantified. Quantification shows that the main source of the CEST signals was from the cells within the blood.

Contents

Acknowledgements

I would like to take this opportunity to thank everyone who has helped and supported me during the course of my PhD. Firstly I would like to thank my supervisor Professor Penny Gowland for her time, effort and knowledge over the last 4 years. Secondly a special thanks to *Team MT/CEST* members Dr. Oliver Mougin, Nicolas Geades and Andrew Carradus for their invaluable help and assistance during experiments. Also a special mention to Richard Dury for all this help during the blood experiments. Also thanks to Dr. Andrew Peters for teaching me the ins and outs of the 7T.

I'd also like to thank everyone at Sir Peter Mansfield Imaging Centre who have made the last four years so enjoyable, in particular the residents of The Barn (& Downstairs Office) and anyone who has joined me in the JA for a beer or few.

Away from work, I'd like thank my housemates and close friends; Chris, Gilbert, Alex, Anna, Nat, Natalie and Stubbs for helping to take my mind off work, with plenty of games of the *drawing game*.

Finally, but not the least, I would like to thank my parents, brother and sister for their love and support.

Abbreviations

AREX Apparent Relaxation Compensated Contrast

APT Amide Proton Transfer

CEST Chemical Exchange Saturation Transfer

CNR Contrast to Noise Ratio

CW Continuous Wave

DS Direct Water Saturation

EPI Echo Planar Imaging

FA Flip Angle

FOV Field of View

FID Free Induction Decay

FWHM Full Width Half Maximum

GE Gradient-Echo

GM Grey Matter

IR Inversion Recovery

LUT Look-Up-Table

MPRAGE Magnetisation Prepared Rapid Gradient Echo

MRI Magnetic Resonance Imaging

MRS Magnetic Resonance Spectroscopy

MT Magnetisation Transfer

MTR Magnetisation Transfer Ratio

NMR Nuclear Magnetic Resonance

NOE Nuclear Overhauser Enhancement

PET Positron Emission Tomography

PNS Peripheral Nerve Stimulation

PTR Proton Transfer Rate

RF Radio Frequency

RBC Red Blood Cell

ROI Region of Interest

SAR Specific Absorption Rate

SNR Signal to Noise Ratio

SENSE Sensitivity Encoding

SE Spin-Echo

sO$_2$ Saturation of Oxygen

SS Sagittal Sinus

TE Echo Time

TFE Turbo-Field-Echo

TI Inversion Time

TR Repetition Time

UHF Ultra High Field

WM White Matter

WASSR Water Saturation Shift Resonance

Introduction

Magnetic Resonance Imaging (MRI) is a non-invasive technique used to produce high resolution images of soft tissues in the human body. Unlike other medical imaging techniques, such as computed tomography (CT) or positron emission tomography (PET), MRI does not use any ionising radiation. The versatility of MRI offers a vast range of applications from high resolution anatomical imaging to spectroscopy and molecular imaging.

Ultra high field MRI offers increased signal to noise ratio, making possible submillimetre isotropic imaging of the human brain, which is very difficult at lower fields. In addition it also provides new contrast mechanisms, such as Chemical Exchange Saturation Transfer (CEST) imaging, which are limited at lower fields. There are many advantages to ultra high field MRI over lower field strengths, but there are technical challenges associated with the move from lower fields, including cost of the scanner and B_1 field inhomogeneity. However, these technical challenges have been overcome and have led to the pioneering of new MR contrasts like CEST. This thesis presents the two techniques to overcome B_1 inhomogeneity at ultra high field, the development of new RF saturation pulses to enhance the visualisation of CEST effects, and finally an investigation into the CEST effects seen in blood.

Overview of Thesis

Chapter 1 provides a theoretical overview of the principles of Nuclear Magnetic Resonance (NMR) and Magnetic Resonance Imaging (MRI). This includes the interactions nuclei have with an external magnetic field, nuclear relaxation processes and MR imaging techniques.

Chapter 2 presents an overview of the instrumentation of an ultra high field

MRI scanner, including the advantages and technical challenges associated with ultra high field MRI. Lastly, dielectric pads are used to improve the B_1 transmit field in regions of interest which typically have low B_1, and simulations of slice-selective RF spokes pulse sequences are also presented to improve the B_1 homogeneity across the whole imaging plane.

Chapter 3 focuses on principles, imaging methods and quantifying the Magnetisation Transfer (MT), Chemical Exchange Saturation Transfer (CEST) and Nuclear Overhauser Enhancement (NOE) at ultra high field. MT from the macromolecules makes the quantification of the CEST and NOE challenging and so the design and development of dual frequency RF saturation pulses are presented as a method to suppress the MT signal contribution to improve visualisation of the CEST and NOE signals in z-spectra. Design and simulations of the dual frequency pulses are preceded by the validation of the new saturation sequence on a bovine serum albumin phantom and *in vivo* application.

Chapter 4 focuses on the MT and CEST effects observed in *ex vivo* human blood including the effects that oxygenation, haematocrit levels and cell structure have on the observed MT and CEST signals, and are quantified. It is hoped this will lead to a better understanding of the origin of the diverse CEST and NOE signal in healthy and pathological tissue.

Conclusion summarises the work presented in this thesis, highlighting the results and key findings obtained, and an outlook for future research projects is discussed.

Chapter 1

Principles of Magnetic Resonance Imaging

1.1 Outline

The following chapter will outline theoretical principles behind Nuclear Magnetic Resonance (NMR) and Magnetic Resonance Imaging (MRI).

1.2 Nuclear Magnetic Resonance

Nuclear Magnetic Resonance (NMR) describes the behaviour of nuclei in the presence of an external magnetic field. In 1946, NMR was first postulated by Bloch & Purcell, and both were awarded the joint Nobel Prize for Physics in 1952 for this work [1, 2]. The NMR phenomenon arises from the interaction between an external magnetic field and the intrinsic angular momentum of nuclei. Intrinsic angular momentum, commonly referred to as spin, is a fundamental property of all matter. Neutrons and protons, which make up nuclei, both possess a spin that can be positive or negative and is quantised. The magnitude of spin angular momentum $\mathbf{J}$ is quantified as,

$$|\mathbf{J}| = \hbar\sqrt{I\left(I+1\right)}, \tag{1.1}$$

where $\hbar$ is Planck's constant h divided by 2π and I is the spin quantum number. The spin quantum number can be integer or half integer only, and within nuclei spins are additive, such that paired spins can cancel each other out. In such a case, nuclei with multiple particles could possess a net spin of zero. Only nuclei with an odd number of protons and/or neutrons have a net spin which is not zero.

1.2.1 Nuclear Magnetisation

As the nucleus is constantly rotating and also possesses an electrical charge, an effective current loop is created, giving rise to a magnetic dipole moment $\boldsymbol{\mu}$,

$$\boldsymbol{\mu} = \gamma \mathbf{J}, \tag{1.2}$$

where γ is the gyromagnetic ratio for a given nucleus. The value of γ is dependant upon the mass and charge of the nucleus. Table 1.1 lists the gyromagnetic ratios for nuclei commonly used in magnetic resonance imaging. Hydrogen nuclei, most commonly used in MRI due to their high abundance in the human body, have a relatively high gyromagnetic ratio compared to other nuclei used in NMR.

Nucleus	Spin	Relative Sensitivity to ^{1}H	$\gamma \left[\text{MHz T}^{-1}\right]$
^{1}H	1/2	1	42.58
^{13}C	1/2	0.016	10.71
^{19}F	1/2	0.83	40.05
^{31}P	1/2	0.066	17.25
^{23}Na	3/2	0.093	11.27

Table 1.1: The gyromagnetic ratio γ for nuclei commonly used in NMR.

1.2.2 Nuclei Interaction with B_0 Field

In the absence of an external magnetic field the spins within a sample are randomly orientated and the net magnetisation is effectively zero. When an external magnetic field is applied, the spins either align parallel or anti-parallel to the direction of the field. The behaviour of the spins in the magnetic field can be described by quantum and classical mechanics.

(a) No external magnetic field   **(b)** Applied external magnetic field B_0
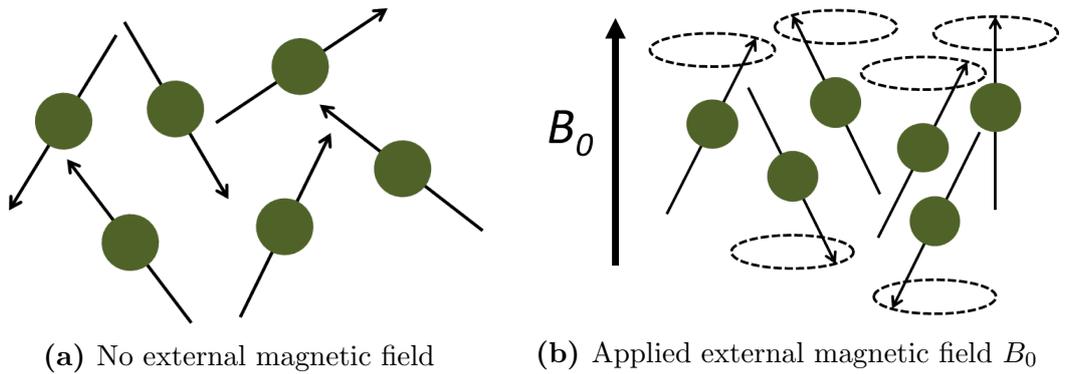
Figure 1.1: The nuclear magnetic moments are initially (a) randomly orientated. In an applied magnetic field B_0, (b) spins align parallel or antiparallel to the direction of the field and precess at the Larmor frequency ω_0.

Quantum Model

Conventionally, the direction of the applied static B_0 field is defined as the z-axis. The quantum model restricts the magnetic dipole moment to have only $(2I + 1)$ orientations, corresponding to the $(2I + 1)$ energy levels. The z-component of the magnetic dipole moment due to the magnetic field is,

$$\mu_z = \gamma \hbar m_I, \qquad (1.3)$$

where the quantum number m_I can only take values of,

$$m_I = -I, -I + 1, \cdots I. \qquad (1.4)$$

1.2. Nuclear Magnetic Resonance

For a spin $1/2$ system, such as the hydrogen proton, m_I can only take the value of $\pm\dfrac{1}{2}$ and therefore,

$$\mu_z = \pm\frac{1}{2}\gamma\hbar. \tag{1.5}$$

The nuclear magnetic moment has a transverse component since $|\boldsymbol{\mu}| > \mu_z$, which indicates that the nuclear magnetic moment cannot align exactly along the z-axis. The nuclear magnetic moment $\boldsymbol{\mu}$ precesses around B_0 at an angular frequency ω_0 as shown in Figure 1.2 and is also called the Larmor frequency ω_0, and this is given by,

$$\omega_0 = \gamma B_0. \tag{1.6}$$
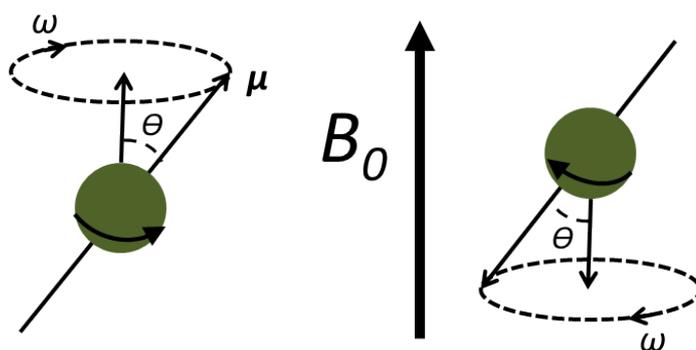
Figure 1.2: The precession (at Larmor frequency ω_0) of a proton's spins under the influence of an external magnetic field B_0.

Spins aligned with the magnetic field are in the lower of the two energy states, whilst spins aligned against the field reside in the higher energy state. The energy difference between the two states, seen in Figure 1.3, is given by,

$$\Delta E = \gamma\hbar B_0. \tag{1.7}$$

Since the spins prefer to occupy the lowest energy state, an imbalance between the spin states occurs, although this energy difference between the states is
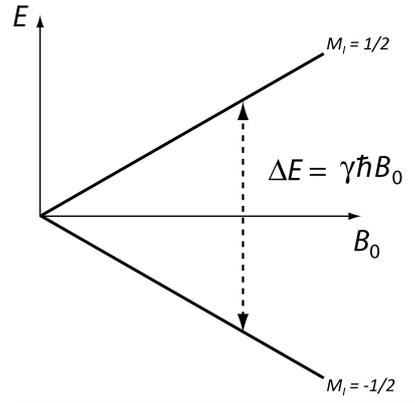
Figure 1.3: Energy level diagram for I $= 1/2$ system, such as a Hydrogen atom.

typically low. At equilibrium the ratio of the number of spins aligned with $(N_\downarrow)$ and against $(N_\uparrow)$ the field is described by the Boltzmann distribution, and is defined as,

$$\frac{N_\uparrow}{N_\downarrow} = \exp\left(\frac{\Delta E}{k_B T}\right), \tag{1.8}$$

where T is the temperature of the spin system and k_B is the Boltzmann's constant. As the energy difference is known to be small, $\Delta E \ll k_B T$, Equ. 1.8 can be approximated using a Taylor expansion to yield,

$$\frac{N_\uparrow}{N_\downarrow} \approx 1 + \frac{\Delta E}{k_B T}. \tag{1.9}$$

Using this, the population difference between the states can be approximated as,

$$N_\uparrow - N_\downarrow \approx N \frac{\gamma \hbar B_0}{2 k_B T}, \tag{1.10}$$

where N is the total number of spins. Each individual spin is a dipole moment and therefore contributes to the bulk magnetisation of the sample. The bulk magnetisation $\mathbf{M}_0$ can be defined as,

$$\mathbf{M}_0 = \sum_{n=1}^{N} \mu_{z,n}\widehat{\mathbf{z}}. \tag{1.11}$$

Substituting in Equ. 1.3 into 1.10, the bulk magnetisation along the applied field only has a longitudinal component. As the phase of the transverse components of the magnetic moments is random, they effectively sum to zero leaving,

$$\mathbf{M}_0 = \frac{\gamma^2 \hbar^2 B_0 N}{4k_B T}\widehat{\mathbf{z}}. \tag{1.12}$$

Classical Model

In the classical model, a magnetic moment $\mathbf{M}$ in an applied magnetic field experiences a torque τ, causing a rotation proportional to the change in angular momentum,

$$\tau = \frac{d\mathbf{J}}{dt} = \mathbf{M} \times \mathbf{B}. \tag{1.13}$$

Substituting Equ. 1.2 into Equ. 1.13 gives the standard form of the Bloch equation,

$$\frac{d\mathbf{M}}{dt} = \gamma \mathbf{M} \times \mathbf{B}. \tag{1.14}$$

This equation indicates that when the magnetisation $\mathbf{M}$ is not perfectly aligned with the magnetic field $\mathbf{B}$, it precesses about it with angular frequency ω_0. In its full form the Bloch equation describes the time evolution of the magnetisation. Including relaxation effects (T_1 and T_2) that govern the recovery of longitudinal magnetisation and the decay of transverse magnetisation respectively (outlined in Section 1.3), the equation becomes,

$$\frac{d\mathbf{M}}{dt} = \gamma \left(\mathbf{M} \times \mathbf{B} \right) - \frac{(M_z - M_0)}{T_1}\widehat{\mathbf{z}} - \frac{M_x\widehat{\mathbf{x}} + M_y\widehat{\mathbf{y}}}{T_2}. \tag{1.15}$$

1.2.3 The Rotating Frame of Reference

As the spins rotate about B_0 at the Larmor frequency ω_0, if a second magnetic field B_1 is applied, the spins in the sample will precess about the combined magnetic field axis. The magnitude of the B_1 field produced by a radio frequency (RF) pulse is significantly smaller than that of the B_0 field. However, when the RF pulse is on-resonance with the precession of the spins, it aligns the phases of the spins. In the static frame of reference it spirals down around the z-axis, Figure 1.4(a).

(a) Laboratory Frame
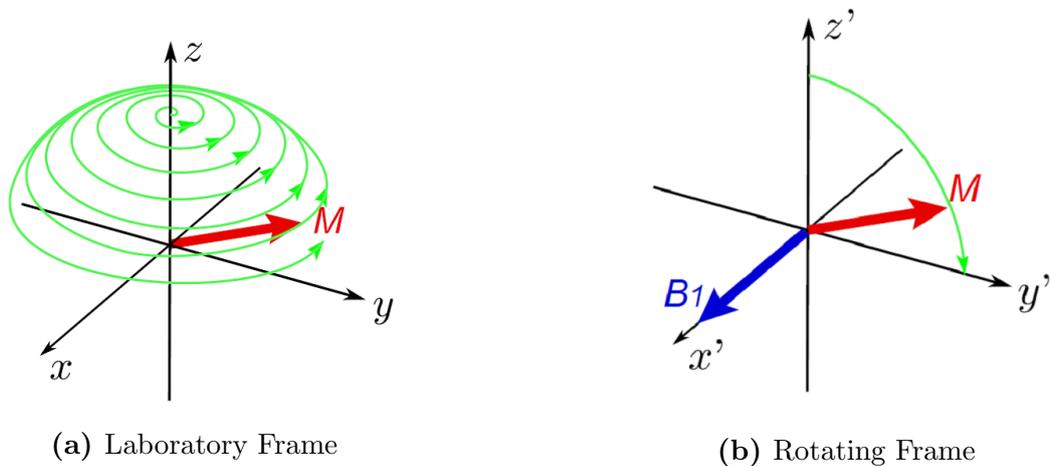
(b) Rotating Frame

Figure 1.4: The evolution of the bulk magnetisation **M** after the application of an on-resonance RF pulse in the (a) laboratory and the (b) rotating frame of reference.

For example, Figure 1.4 shows the evolution of the net magnetisation vector **M** in both the laboratory and rotating frame after the application of 90° RF excitation pulse. The magnetisation **M** is tipped into the transverse plane, M_{xy}, by the pulse away from the longitudinal axis which is parallel to the main magnetic field B_0. In (a) the laboratory frame the magnetisation vector **M** and the B_1 field both rotate about the longitudinal axis at the frequency ω_0. In (b) the rotating reference frame, rotating at the Larmor frequency ω_0, the B_1 field appears stationary. A quadrature B_1 field due to an RF pulse can be described by the following equation in the laboratory frame,

1.2. Nuclear Magnetic Resonance

$$\mathbf{B}_1(t) = \hat{x}B_1(t)\cos(\omega t) - \hat{y}B_1(t)\sin(\omega t).$$ (1.16)

To transform into the rotating frame of reference, a rotation matrix rotating at ω_0 about the z-axis is applied to Equ 1.16.

$$\begin{pmatrix} B_{1,x'}(t) \\ B_{1,y'}(t) \\ B_{1,z'}(t) \end{pmatrix} = \begin{pmatrix} \cos(\omega_0 t) & -\sin(\omega_0 t) & 0 \\ \sin(\omega_0 t) & \cos(\omega_0 t) & 0 \\ 0 & 0 & 1 \end{pmatrix} \begin{pmatrix} B_1(t)\cos(\omega t) \\ -B_1(t)\sin(\omega t) \\ 0 \end{pmatrix}.$$ (1.17)

In the case where the quadrature B_1 is exactly on-resonance, i.e. $\omega = \omega_0$, Equ. 1.17 reduces to,

$$\begin{pmatrix} B_{1,x'}(t) \\ B_{1,y'}(t) \\ B_{1,z'}(t) \end{pmatrix} = \begin{pmatrix} B_1(t)\cos^2(\omega t) + B_1(t)\sin^2(\omega t) \\ B_1(t)\sin(\omega t)B_1(t)\cos(\omega t) - B_1(t)\cos(\omega t)B_1(t)\sin(\omega t) \\ 0 \end{pmatrix},$$ (1.18a)

$$\begin{pmatrix} B_{1,x'}(t) \\ B_{1,y'}(t) \\ B_{1,z'}(t) \end{pmatrix} = \begin{pmatrix} B_1(t) \\ 0 \\ 0 \end{pmatrix}.$$ (1.18b)

Viewing the oscillating quadrature B_1 field in the rotating frame, the B_1 field becomes stationary along the x' axis that it is applied along. The angle α by which the magnetisation is tipped away from the longitudinal axis and into the $x'y'$ plane is a function of the amplitude and duration of the applied B_1 field,

$$\theta = \int_0^\tau \gamma B_1(t)\,dt,$$ (1.19)

where τ is the duration of the RF pulse. A 90° RF pulse tips the magnetisation

$\mathbf{M}$ fully into the $x'y'$ plane, whereas a 180° RF pulse inverts the bulk magnetisation. It is also possible to saturate the magnetisation, if a sufficiently long enough RF pulse is applied. In this case the spin system settles at a steady state of $M_z = 0$ nulling the net magnetisation.

1.2.4 Free Induction Decay (FID)

The most basic experiment in NMR is the generation of a Free Induction Decay (FID) signal. A sample is placed in a static uniform B_0 field, with a surrounding RF transmit coil which is used to generate an oscillating B_1 field. Before the RF field is applied, the sample's magnetisation aligns with the static B_0 magnetic field. Application of an RF pulse on-resonance, at the Larmor frequency, causes the spins to be tipped into the transverse plane. After the RF pulse is turned off, a voltage can be detected on the receive coil via Faraday induction. The resulting signal oscillates at the resonant frequency and decays exponentially. The rate of decay depends on the sample and is characterised by a rate constant T_2^* as shown in Figure 1.5. This signal gives information about the environment of the spins and is the basis of all NMR experiments.

1.3 Relaxation and Contrast

It is physically implausible that when the bulk magnetisation $\mathbf{M}$ is tipped from equilibrium it would stay in this state forever. In a real system, there are interaction and processes with the local environment which return $\mathbf{M}$ back to the thermal-equilibrium state. Longitudinal relaxation sees the z-component of the magnetisation return due to an exchange of energy between the spin system and the surrounding thermal reservoir, defined historically as the 'lattice', and transverse relaxation acts to return the magnetisation in the xy plane to zero. The time constants of these relaxation processes are referred to as T_1 and
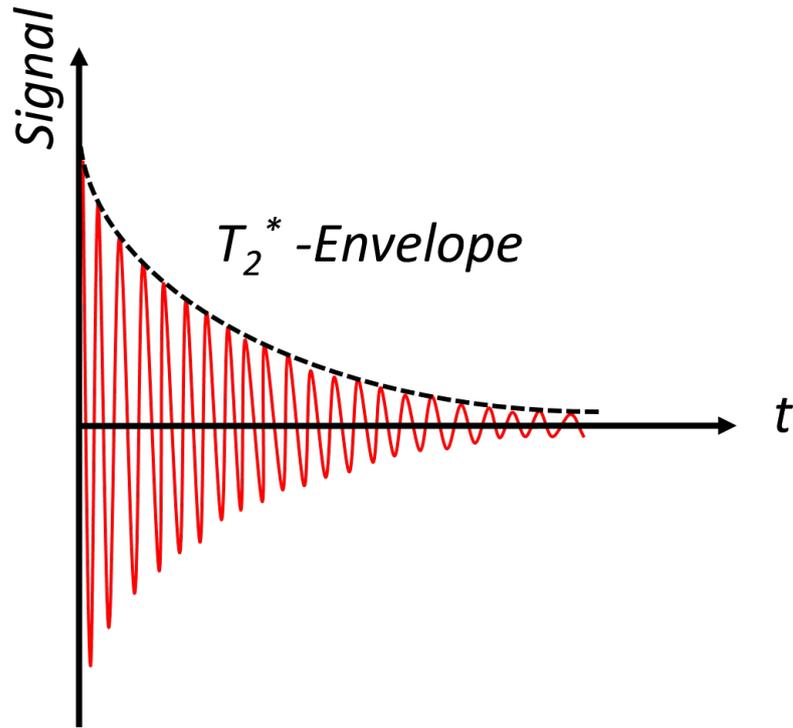
Figure 1.5: A free induction decay (FID) signal with a T_2^* envelope.

T_2, respectively and these relaxation processes are used in MRI as a source of contrast.

1.3.1   Longitudinal Relaxation Time T_1

The exchange of energy between the spin system and the surrounding environment, often termed the spin-lattice relaxation, results in the longitudinal magnetisation that has been modified by a RF pulse returning to its equilibrium position M_0. The time between the switching off of the RF pulse and the bulk magnetisation fully returning to M_0 is known as the longitudinal relaxation time T_1. The longitudinal relaxation contribution to the Bloch equation is given by,

$$\frac{dM_z(t)}{dt} = \frac{M_0 - M_z(t)}{T_1}. \tag{1.20}$$

The mechanisms that cause T_1 recovery are associated with the local magnetic

1.3. Relaxation and Contrast

fields fluctuating at the Larmor frequency due to the rotation and translation of nearby molecules via dipole-dipole interactions. The rate of energy loss relates to how closely the molecules are coupled together, and in brain tissue can indicate the mobility of the molecules, particularly water, and whether they are bound to other macromolecules. In the brain, white matter has shorter T_1 than grey matter due to the presence of myelin in white matter, to which water molecules are bound restricting their motion. The Cerebro-Spinal Fluid (CSF) which is made up mainly of free water molecules has a much longer T_1 time than white and grey matter [11].

Measuring T_1 Relaxation

Solving the Bloch equation (Equ. 1.20) the recovery of the longitudinal magnetisation M_z to thermal equilibrium immediately after an RF pulse, $t = 0$, is given by,

$$M_z(t) = M_0 \left[1 - \exp\left(-\frac{t}{T_1} \right) \right] + M_z(0) \exp\left(-\frac{t}{T_1} \right). \qquad (1.21)$$

In the saturation recovery experiment, Figure 1.6 (blue line), a 90° RF pulse is used to tip the magnetisation completely into the xy plane. So at $t = 0$, $M_z(0) = 0$ and therefore Equ. 1.21 reduces to,

$$M_z(t) = M_0 \left[1 - \exp\left(-\frac{t}{T_1} \right) \right]. \qquad (1.22)$$

The 'gold standard' technique for T_1 imaging in MR, is the inversion recovery experiment. Instead of a 90° pulse (saturation case) a 180° pulse is used to fully invert the magnetisation, such that $M_z(0) = -M_0$. The use of an inversion pulse reverses the magnetisation without the induction of phase coherence. The solution of the Bloch equation, Equ. 1.21, following an inversion pulse becomes,

$$M_z(t) = M_0 \left[1 - 2 \exp\left(-\frac{t}{T_1} \right) \right]. \tag{1.23}$$

To measure the T_1 after the inversion pulse at variable time intervals TI, the recovering longitudinal magnetisation is tipped into the transverse plane in order to measure its recovery.
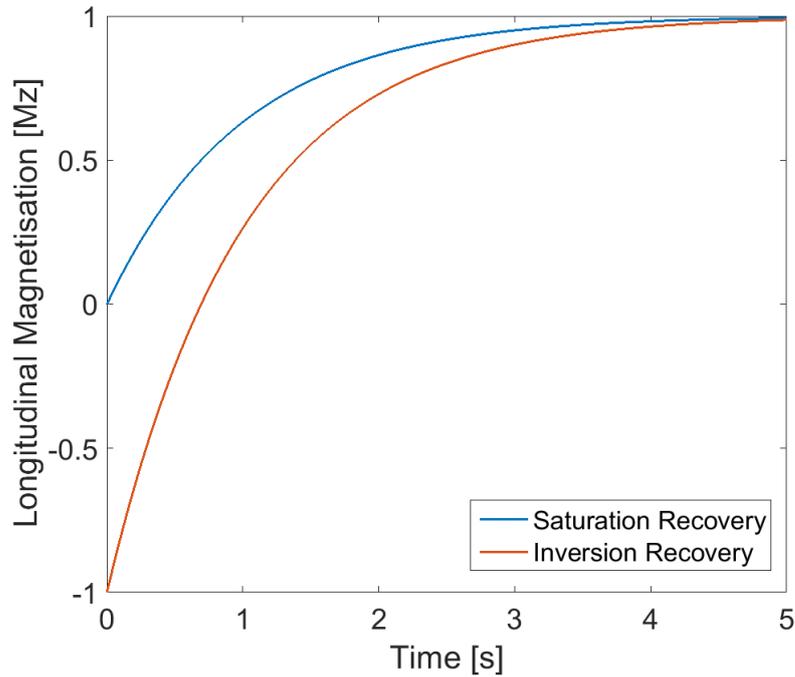
Figure 1.6: The longitudinal magnetisation signal recovery for $T_1 = 1$ s in a saturation and inversion recovery experiment (i.e. following a 90° or 180° pulse).

1.3.2 Transverse Relaxation Times T_2 and T_2^*

When a spin system undergoes a perfect 90° RF pulse, the net magnetisation $\mathbf{M}$ is fully tipped in the transverse plane M_{xy}. After the pulse, the spins will continue to process around the z-axis. However, random dipole-dipole interactions with neighbouring spins produce changes in the local magnetic field and thus slightly alter the precessional frequency of each of the individual spins, away from the Larmor frequency. This causes dephasing as spins process about the transverse plane at different rates, and eventually M_{xy} decays back to zero (i.e.

where no phase coherence remains), its equilibrium state, at a rate characterised by the time constant T_2. This mechanism is termed spin-spin relaxation and is caused by the exchange of energy between spins. The loss of phase coherency only affects the transverse component of the magnetisation and therefore the longitudinal magnetisation is unaffected. The transverse relaxation of $\mathbf{M}$ contribution to the Bloch equation (Equ. 1.15), is given by,

$$\frac{dM_{xy}(t)}{dt} = -\frac{M_{xy}(t)}{T_2}. \tag{1.24}$$

Solving this differential equation, the evolution of the transverse magnetisation M_{xy} after time t is given by,

$$M_{xy}(t) = M_{xy}(0) \exp\left(-\frac{t}{T_2}\right). \tag{1.25}$$

The measured signal after a $90°$ pulse decays faster than theoretically predicted in Equ. 1.25, as a result of B_0 inhomogeneities causing small shifts in the local resonance frequency and leading to additional spin dephasing which results in destruction of the transverse magnetisation. This faster transverse rate of decay, termed T_2^*, includes the effects of T_2 processes associated with spin-spin relaxation and T_2' accounting for dephasing due to inhomogeneity in the B_0 field,

$$\frac{1}{T_2^*} = \frac{1}{T_2} + \frac{1}{T_2'}. \tag{1.26}$$

Measuring T_2 Relaxation

In order to measure T_2, the effects of T_2' need to be removed. Signal dephasing contributing to T_2' remains constant over time, whereas the T_2 dephasing relates to factors that change over time. A simple spin-echo sequence can refocus the dephasing due to constant factors (T_2') and thus allows the quantitative

measurement of T_2.
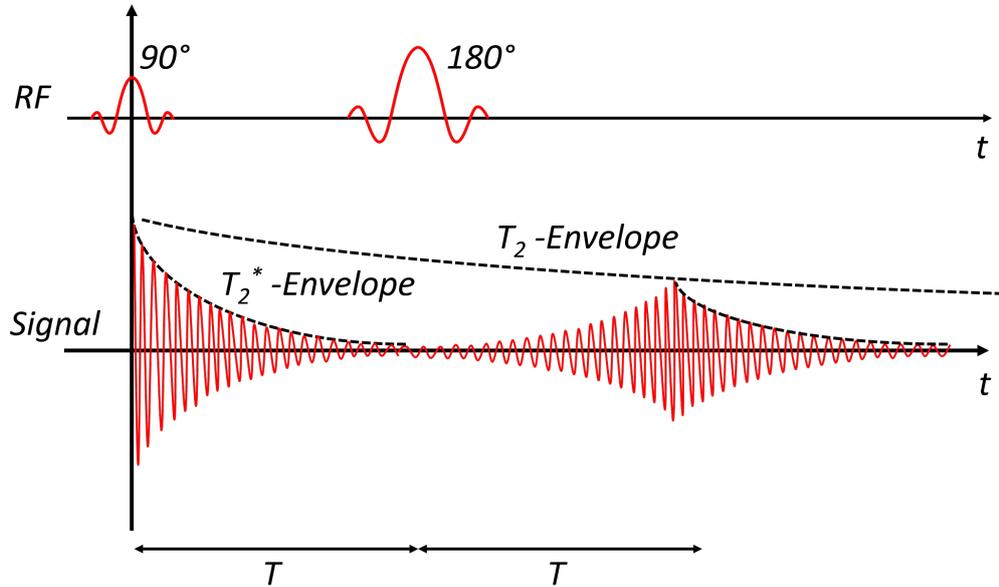
Figure 1.7: Schematic of spin-echo sequence consisting of a 90° excitation pulse and a 180° refocusing pulse to stimulate an echo used to measure T_2.

The spin-echo sequence seen in Figure 1.7 consists of a 90° excitation and 180° refocusing pulse separated by time $t = T$. A perfect 90° RF pulse tips magnetisation fully into transverse plane, Figure 1.8(a). Initially at time $t = 0$, the spins are coherently in phase. However, due to local B_0 field inhomogeneities spins have faster and slower precessional frequencies than the mean Larmor frequency. As a result the spins will fan out, Figure 1.8(b). The application of a 180° refocusing pulse at time $t = T$, causes the spins to be flipped so that the phase shift is reversed. During the time T each spin will accumulate a phase shift of ϕ. After the application of the 180° pulse and a further time T (such that $t = 2T$) the spins will accumulate a further phase shift of $-\phi$, therefore refocusing the signal, Figure 1.8(d).

In the spin echo sequence, any dephasing effects that remain constant between the application of the 90° pulse and the spin echo will be rephased, for example the effects of local B_0 inhomogeneities. Dephasing due to molecular motion, spin exchange or diffusion in local field gradients will not be refocused.

(a) M_{xy} initially after a 90° excitation

(b) Spins desphasing after time $t = T$

(c) M_{xy} after a 180° refocusing pulse

(d) Spins rephase to form an echo
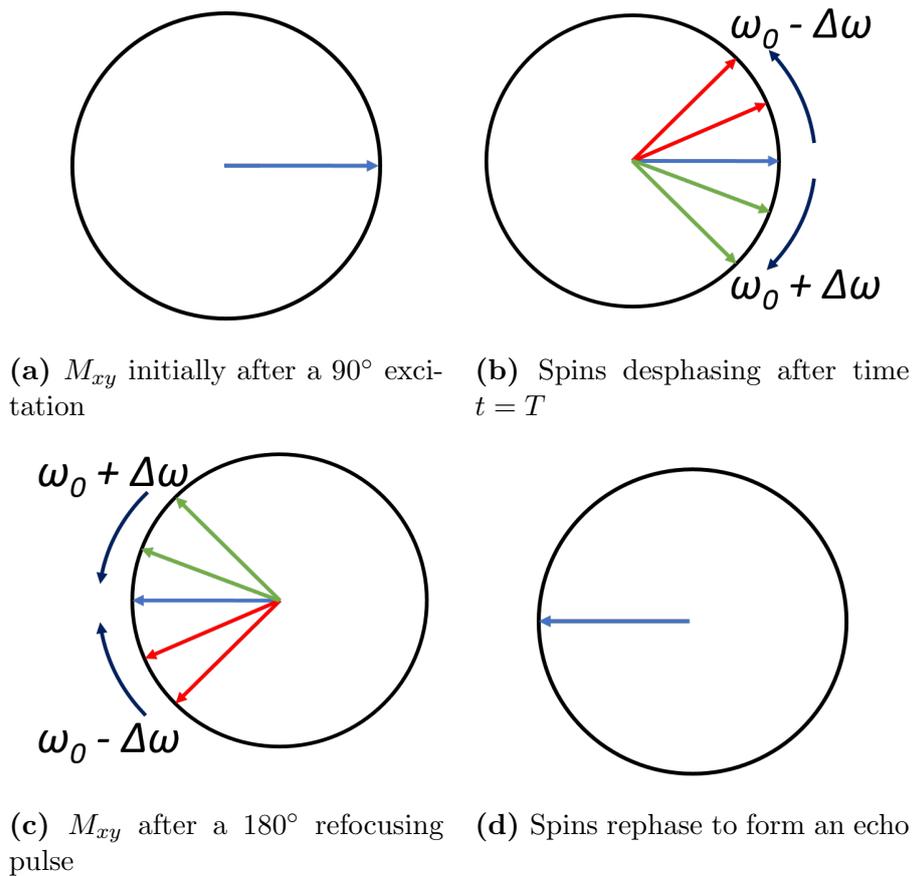
Figure 1.8: Schematic of the spin evolution in a spin-echo sequence.

The decay of the transverse magnetisation can be affected by diffusion and results in underestimation of T_2. At higher field strengths, as local field gradients increase, the relative diffusion contribution to the phasing increases. The Carr-Purcell Meilboom-Gill (CPMG) sequence [3] can be used to correct for the molecular diffusion, but is difficult to apply accurately *in vivo* because of the effects of B_1 inhomogeneities.

Measuring T_2^* Relaxation

After a 90° pulse, the envelope of the FID signal, Figure 1.5, can be described by the following equation $\exp(-t/T_2^*)$. Measuring the amplitude of the FID at different times t and applying an exponential fit, T_2^* can be quantified.

1.3.3 Correlation Time

Longitudinal magnetisation relaxation describes the recovery of the $\hat{z}$ component of the magnetisation, as spins flip from the higher energy state to the lower state. Longitudinal relaxation depends on the direction of the magnetic moment μ and therefore a magnetic interaction must take place to induce the transition between states. The magnetic field responsible is generated by the sample, via molecular tumbling, in the form of a random fluctuating background magnetic field B_r, that is superimposed onto the main magnetic field B_0. The major source of this fluctuating field is from dipole-dipole interactions. Each spin-$\frac{1}{2}$ nucleus has an associated dipole field, and when two nuclei are in close proximity, Figure 1.9, they will experience a small disturbance to the main B_0 field. The magnetic field in the transverse plane B_{xy} that is generated by one nucleus to another molecule that is r away, is described by,

$$B_{xy} \propto \frac{1}{r^3} \sin\left(\theta\right) \cos\left(\theta\right),$$ (1.27)

where r is the inter-nucleus distance and θ is the angle between the B_0 field and the vector connecting the centres of the nuclei (Figure 1.9). As molecules of water randomly tumble in solution and undergo Brownian motion, the background magnetic field varies randomly.

The transverse relaxation rate of a sample is dependant upon the frequency distribution of the randomly fluctuating background field. The Bloembergen-Purcell-Pound (BPP) theory describes the frequency distribution that is observed. An autocorrelation function $G(t)$ is used to describe how well coupled the geometry of a molecule at a reference point is to its geometry at a time τ later. The autocorrelation function $G(t)$ decays exponentially with time as,

$$G(t) = \exp\left(\frac{-\tau}{\tau_c}\right),$$ (1.28)
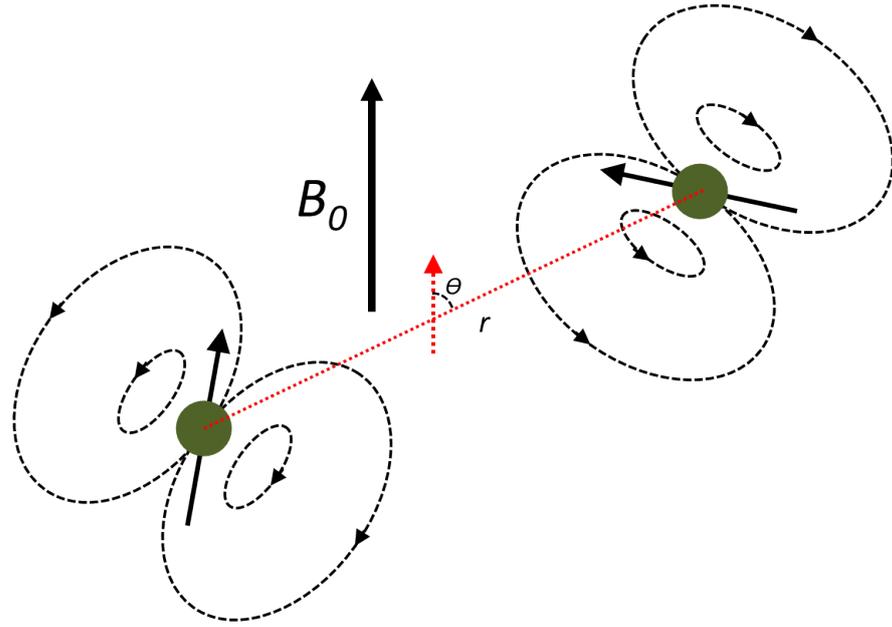
Figure 1.9: Two randomly tumbling magnetic dipole moments that are separated by the distance r. They are in close proximity such that they both influence the magnetic field each experiences, and the fluctuations in the magnetic field they experience due to the tumbling, induces relaxation processes.

where τ_c describes the decay memory of the tumbling motion, termed correlation time. The correlation time τ_c can be thought of as the average time taken for a molecule to rotate through a single radian. The spectral density $J(\omega)$, is the frequency analogy of $G(t)$, and describes the fluctuation of the frequency of the spins,

$$J(\omega) = \frac{\tau_c}{1 + \omega^2 \tau_c^2}. \tag{1.29}$$

If the transverse field of the molecule fluctuates rapidly, the molecule is highly mobile and is changing its motional state with high frequency so that the correlation time τ_c is short and the spectral density function is broad. Conversely, a slowly fluctuating field produces a narrow spectral density, with a long correlation time.

A short τ_c means a small number of water molecules tumbling at the Larmor frequency, and hence comparable T_1 and T_2 relaxation rates as seen in CSF. For water molecules, bound to macromolecules forming a hydration layer, the T_2
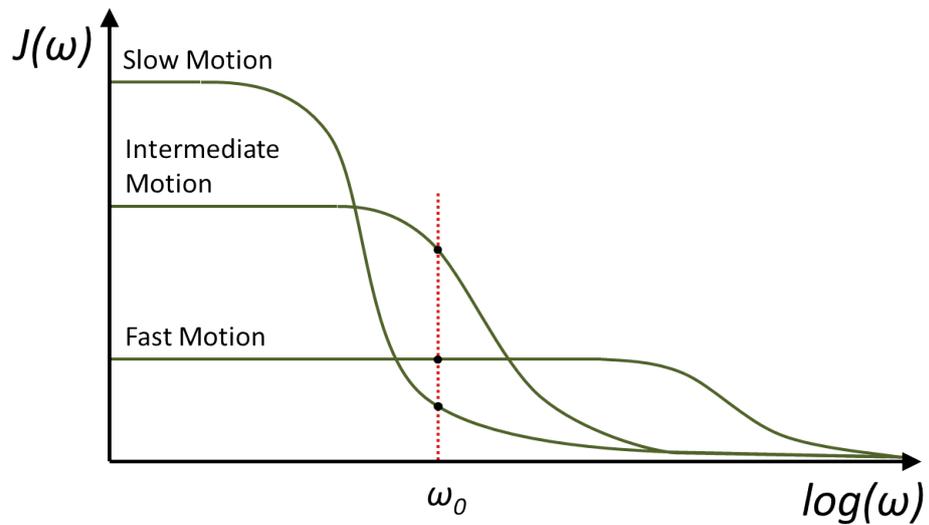
Figure 1.10: Spectral density function $J(\omega)$ for three molecules with difference correlation times τ_c.

relaxation is very efficient due to rapid dephasing with respect to other protons. The T_1 and T_2 relaxation rates diverge as the time varying background field that provides the non-secular contributions from T_1 relaxation contributing to T_2 relaxation reduces, whilst the secular contribution begins to dominate, as described by $J(0)$. These influences causes the T_2 to decrease linearly with increasing τ_c (tumbling slows and the background field becomes more static). While the correlation time τ_c is a good indication of the environment and the dynamic of the spins, it is not generally a practical measure. However diffusion and exchange of the magnetisation can be measured separately.

1.3.4 Susceptibility

The magnetic susceptibility χ, a dimensionless constant, describes how easily a sample becomes magnetised in response to the applied B_0 field. The effective local magnetic field generated by susceptibility effects is defined as,

$$B_{eff} = (1 + \chi) B_0. \tag{1.30}$$

The nuclear susceptibility of a proton, $\chi > 0$, is paramagnetic, where as the bulk susceptibility of tissue, $\chi < 0$, is diamagnetic. These susceptibility effects induce changes in the main magnetic field as seen in Equ. 1.30 and can result in artefacts in the acquired images.

1.3.5 Chemical Shift

As described so far, T_2 and T_2^* relaxation mechanisms result in variation in the Larmor frequency of the spins. Also affecting the Larmor frequency is the surrounding chemical environment in which the spins are situated. They will experience different static magnetic fields due to varying degrees of electronic shielding, known as chemical shift. The effective magnetic field, B_{eff}, that the spins experience due to the combination of the static B_0 field and the induced field generated by the free electrons of the molecules in the sample can be described by the following equation,

$$B_{eff} = (1 - \sigma) \, B_0. \tag{1.31}$$

The parameter σ is the chemical shielding constant and the chemical shift parameter δ, expressed in parts per million (ppm) is defined as,

$$\delta = \frac{\omega - \omega_{ref}}{\omega_{ref}} \times 10^6. \tag{1.32}$$

The reference resonance frequency ω_{ref}, in Magnetic Resonance Spectroscopy (MRS) is the Larmor frequency of ^{1}H nuclei in tetramethylsilane (TMS). This additional off-resonance effect can provide information on the chemical environment. In MRS, a single FID can be Fourier transformed, and analysis of the resulting spectrum can yield information about the chemical environment, and the chemical shift can be utilised to provide chemical exchange and magnetisation transfer contrast. In MRI the chemical shift between water and fat can

cause artefacts.

1.4 Principles of Imaging

So far only the origin of the NMR signal has been considered, and for MRI, we need to be able to localise the signal detected in the sample spatially. In 1973 Paul Lauterbur proposed using gradient fields to localise the source of the NMR signal [4]. Lauterbur used linear gradient magnetic fields, applied across a sample at a range of different angles, so that with back-projection reconstruction, a 2D image of the sample was formed. At a similar time, Mansfield and Grannell [5] presented a technique on NMR diffraction by gradients that introduced the concept of imaging in reciprocal k-space and, a year later, a method of selective excitation [6], which is still widely used in MRI today. Ernst then developed a Fourier imaging technique [7] combining non-selective excitation and orthogonal linear gradient fields to generate 2D Fourier encoded images. These techniques now form the basis of most MRI and will be outlined below in more detail.

1.4.1 Source Localisation using Gradient Fields

Gradient fields in the x, y and z planes can be superimposed onto the static B_0 field and result in small linear variations in the magnetic B_0 field along these planes. This leads to the resonant frequency ω_0 varying as a function of position. The applied total gradient field, $\mathbf{G}$ can be expressed in a tensor format with components along the magnetic fields axes B_x, B_y and B_z,

$$
\mathbf{G} = \begin{vmatrix} \hat{i}\hat{i}\dfrac{\partial B_x}{\partial x} & \hat{i}\hat{j}\dfrac{\partial B_x}{\partial y} & \hat{i}\hat{k}\dfrac{\partial B_x}{\partial z} \\[2ex] \hat{j}\hat{i}\dfrac{\partial B_y}{\partial x} & \hat{j}\hat{j}\dfrac{\partial B_y}{\partial y} & \hat{j}\hat{k}\dfrac{\partial B_y}{\partial z} \\[2ex] \hat{k}\hat{i}\dfrac{\partial B_z}{\partial x} & \hat{k}\hat{j}\dfrac{\partial B_z}{\partial y} & \hat{k}\hat{k}\dfrac{\partial B_z}{\partial z} \end{vmatrix}. \tag{1.33}
$$

1.4. Principles of Imaging

However, the main magnetic field B_0 is only applied along the z-axis and therefore the gradient tensor can be reduced to,

$$\mathbf{G} = \frac{\partial B_z}{\partial x}\hat{i} + \frac{\partial B_z}{\partial y}\hat{j} + \frac{\partial B_z}{\partial z}\hat{k}, \qquad (1.34)$$

as the gradient fields in B_x and B_y have very little effect on the resonant frequency of spins, although they can cause artefacts, particularly in non-transverse planes [8]. The superimposed gradient fields on the B_0 field result in the total magnetic field becoming a function of position $\mathbf{r}$,

$$B_z(r) = (B_0 + \mathbf{G} \cdot \mathbf{r})\,\hat{k}. \qquad (1.35)$$

Therefore the Larmor frequency ω_0 of the spins can be described as a function of position and time in the sample:

$$\omega(r, t) = \gamma\left(B_0 + xG_x\left(t\right) + yG_y\left(t\right) + zG_z\left(t\right)\right). \qquad (1.36)$$

The application of gradient fields is very important in the reconstruction of images in MRI in both 2D and 3D. In the following three sections, slice selection, frequency and phase encoding will be outlined. These all use gradient fields to localise the source of the NMR signal.

Slice Selection

Slice selection, also known as selective excitation, is a technique used to excite a slab of spins in a sample by applying a gradient field throughout the duration of the RF excitation pulse. RF excitation pulses used to excite the spins without an applied gradient field, known as non-selective excitation, excite all the spins in the sample within the pulse bandwidth, independent of position. Typically the slice selection gradient field is applied in the z-axis, causing a linear variation of

the Larmor frequency across the sample. By simplifying Equ. 1.36, the Larmor frequency as a function of position in the z-direction becomes,

$$\omega(z) = \gamma \left(B_0 + zG_z \right).$$

<div align="right">(1.37)</div>

The thickness Δz of the slice excited is determined by the bandwidth of the RF pulse and the amplitude of the gradient field,

$$\Delta z = \frac{\Delta \omega}{\gamma G_z}.$$

<div align="right">(1.38)</div>

The bandwidth of the RF excitation pulses dictates the range of resonance frequencies, $\Delta \omega$, that the pulse will excite. Thus, to decrease the slice thickness, the bandwidth of the pulse can be reduced. It is also possible to reduce the slice thickness by increasing the amplitude of the gradient field G_z. These effects are shown in Figure 1.11(a).
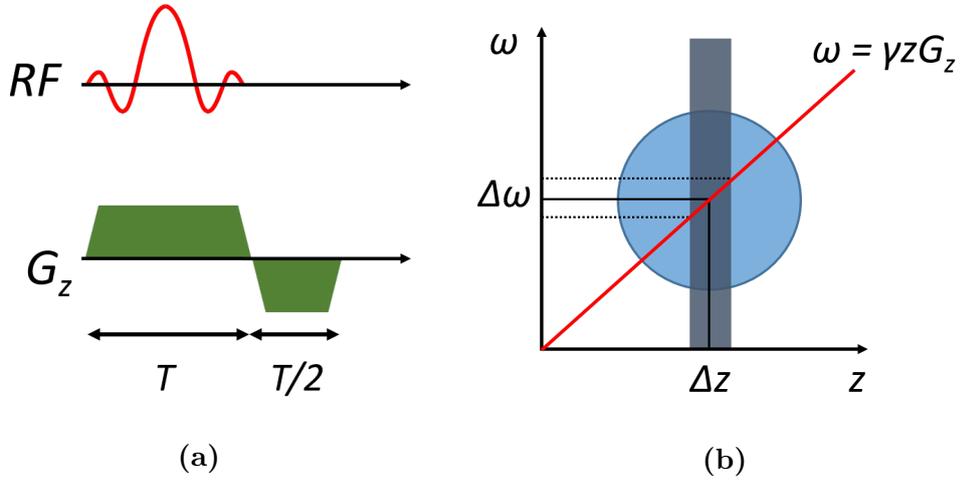
Figure 1.11: (a) An RF excitation pulse of $\Delta \omega$ bandwidth applied over a slice selection gradient, followed by a negative rewind to refocus the signal. (b) A slice of thickness Δz is excited.

Note that in Figure 1.11(a) after the slice selection gradient is applied, it is followed by a negative gradient of duration $T/2$. This gradient is used to rephase the signal that becomes dephased during the application of the slice selection

gradient to ensure maximum measured signal.

The excitation profile achieved by the slice selective RF pulse can be approximated by a Fourier Transform using the small tip angle approximation. To acquire a perfect rectangular profile, an RF sinc pulse of infinite length would be required, which is not feasible. In practice, sinc pulses have 3 or 5 lobes and Gaussian filtering to improve the excitation profile and limit the side bands outside the slice profile.

Frequency Encoding

Slice selection means that the measured signal is originating from a defined volume, but more spatial specificity is required to produce a 2D or 3D image. In frequency encoding the gradient fields are applied during the signal acquisition readout rather than the excitation. This gradient is applied along the x-axis and therefore a simplified form of Equ. 1.36 arises,

$$\omega(x) = \gamma \left(B_0 + xG_x \right). \tag{1.39}$$

Considering only a small part of the detected signal at a location $\mathbf{r}$ within a sample at a time t, without the presence of relaxation, the measured signal $S(r, t)$ is proportional to the spin density, ρ,

$$S(r, t) \propto \rho(r) \exp \left(i \int_0^t \omega(r, \tau) \, d\tau \right). \tag{1.40}$$

Extending this to an entire volume of space, the signal can be expressed as,

$$S(t) \propto \int_x \int_y \int_z \rho(r) \exp \left(i \int_0^t \omega(r, \tau) \, d\tau \right) dx dy dz. \tag{1.41}$$

where the precessional frequency of the spins, $\omega(r, \tau)$, is determined by the strength of the main magnetic field B_0 and the time evolution of the gradient

fields. The signal can be demodulated to remove the Larmor frequency ω_0 related to the B_0 field. After demodulation, the signal can only be considered by the time evolution of the gradient fields from time $t = 0$ to $t = \tau$, in the form,

$$S(r) \propto \int_x \int_y \int_z \rho(r) \exp\left(ik(t) \cdot r\right) dx dy dz, \tag{1.42}$$

where $k(t)$ describes the phase evolution and is defined as the reciprocal gradient space vector,

$$\mathbf{k}(t) = \gamma \int_0^t \mathbf{G}(\tau)\, d\tau. \tag{1.43}$$

Equ. 1.42 is in the form of a 3D Fourier Transform and so by taking an inverse Fourier Transform, the spin density of the sample can be obtained and this concept forms the basis of modern imaging techniques in MRI.

Phase Encoding

To fully acquire a 2D image from the detected signal, another linear gradient field is applied orthogonal to the frequency encoding gradient field. The phase encoding gradient G_y imposes a linear phase variation along the y direction between the RF excitation pulse and readout, such that

$$\omega(y) = \gamma\left(B_0 + yG_y\right). \tag{1.44}$$

The phase accumulated during this encoding gradient applied from $t = 0$ to $t = T$ is,

$$\phi(y) = \gamma y \int_0^T G_y(t)\, dt. \tag{1.45}$$

Several phase encoding gradients of varying field strengths are required, with

an FID signal measured after each, into order to produce a 2D MR image. The phase encoding gradient gives an initial phase to the magnetisation at the start of the FID and so by varying the area under the phase encoding gradient, different amounts of linear phase variations are introduced. The resulting signals are reconstructed *via* a Fourier transform to recover the spatial information.

1.4.2 k-Space

In order to visualise the motion of the spins under influence of frequency and phase encoding gradients, the principle of k-space in MR imaging, also referred to a Fourier space, was formulated in 1983 [9]. In general, k-space is defined by the spatial frequencies k_x, k_y and k_z corresponding to the spatial Cartesian coordinates x, y and z. Commonly, most MRI imaging techniques acquire one slice at a time. In this case, known as 2D planar imaging, k_z is fixed and only k_x and k_y are varied.

(a) Real Space
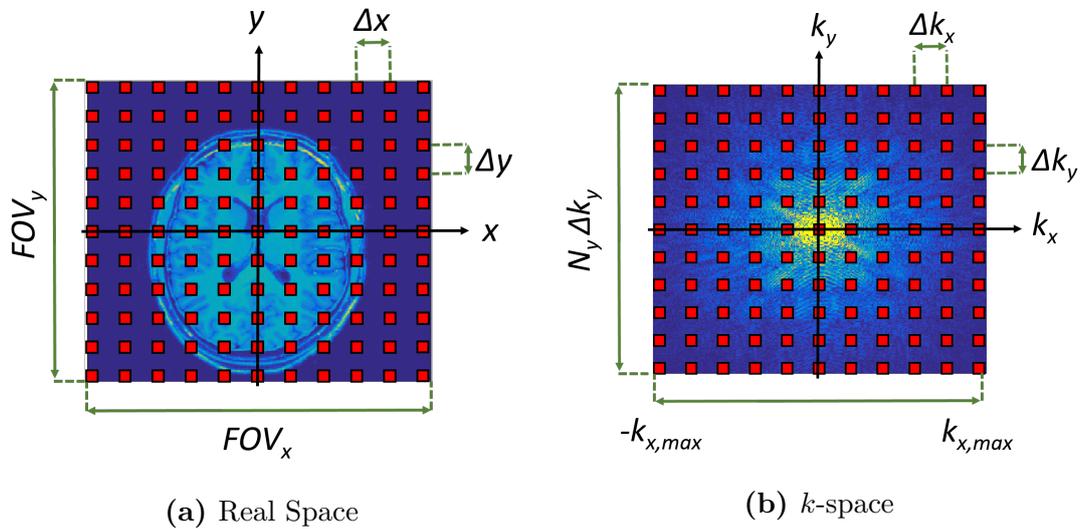
(b) k-space

Figure 1.12: The relationship between the FOV, spatial resolution and sampling between real space and k-space.

Immediately after an RF slice selection excitation pulse and rewind gradient, in 2D planar imaging, the sampling position is at the centre of k-space. The centre of k-space ($k_x = k_y = 0$), where the low spatial frequencies originate, provides

information of the bulk image intensity. Higher spatial frequencies, the outer edges of k-space, provide the finer detail about the acquired MR image.

In order to fully sample k-space, the sampling position is moved according to a k-space trajectory defined by the frequency encoding and phase encoding gradients. The signal acquired during the frequency encoding are recorded at regular intervals along the k_x direction.

k-space represents a continuous range of spatial frequencies, however the signal measured from an FID or echo is sampled at discrete intervals. The spacing and location of the k-space sampling determines the field of view (FOV) and the spatial resolution of the MR image,

$$FOV_{x,y} = \frac{1}{\Delta k_{x,y}}, \tag{1.46}$$

and so sampling further away from the centre of k-space produces greater resolution in the reconstructed MR image.

1.4.3 Imaging Pulse Sequences

Spin Warp

MR imaging sequences generally are based on either a Gradient Echo (GE) or Spin Echo (SE) (already described in Section 1.3.2 in reference to measuring T_2). Echoes are used to give a symmetric signal and therefore a real Fourier transform. In a GE sequence, Figure 1.13, after the excitation pulse a negative linear gradient field is applied along G_x. The spins dephase during this time T whilst the gradient is applied. After time $t = T$, the negative gradient's polarity is reversed and applied for twice the length of time. The phase accumulation is reversed by this process, and spins that had rapidly dephased come back into phase with the slower dephasing spins, resulting in an echo forming.

Spin warp imaging uses this technique to sample k-space by moving across the k_x axis collecting gradient echoes, whilst using a phase encoding gradient G_y to step over k_y to acquire k-space in 2D.
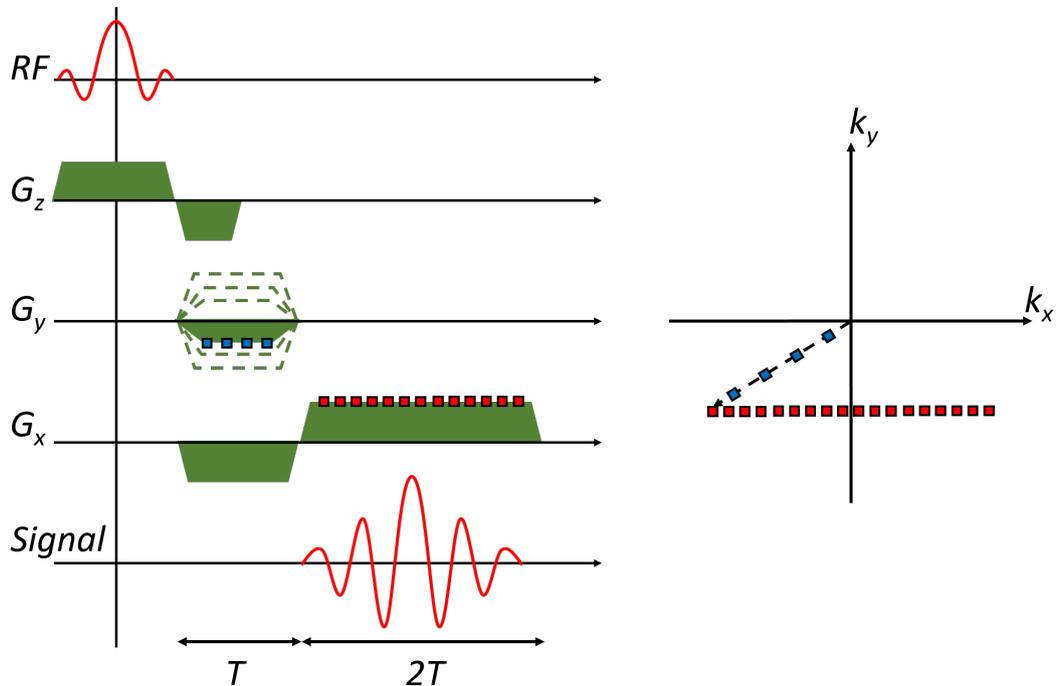
Figure 1.13: Schematic of gradient echo sequence and k-space trajectory.

Turbo Field Echo (TFE)

Spin warp imaging is a very robust technique and has the advantage of lower specific absorption rate (SAR) over SE sequences that require multiple 180° refocusing pulses. Acquisition times can be long, particularly if a 90° excitation pulse is used to achieve maximum signal, as long time intervals between gradient echoes are needed in order for recovery of the magnetisation.

To speed up acquisition times RF excitation pulses with smaller flip angles are used. Tipping the magnetisation by only a small amount ($\sim 10°$) leaves a large component of the longitudinal magnetisation. As a result the TR between RF excitation pulses can be shortened. The smaller flip angle tips enough of the longitudinal magnetisation into the transverse plane for signal to be recorded,

1.4. Principles of Imaging

after which a gradient spoiler is used to destroy the transverse magnetisation before the next excitation pulse. This ensures that the recorded images are only of T_1 weighting. The longitudinal magnetisation M_z after a train of RF excitation pulses, of flip angle α and evenly spaced in time by TR, will reach a steady state after a sufficient number of pulses. The steady state depends on the TR and the flip angle α of the excitation pulses, as well as the T_1 of the sample. Under the assumption that the transverse magnetisation is completely spoilt between TRs, the gradient echo signal can be quantified as,

$$S_{TFE} = M_0 \frac{\sin{(\alpha)} \left[1 - \exp\left(-\frac{TR}{T_1}\right)\right]}{1 - \cos{(\alpha)} \exp\left(-\frac{TR}{T_1}\right)} . \exp\left(-\frac{TE}{T_2^*}\right). \tag{1.47}$$

The maximum achievable signal for a given TR is defined by the Ernst angle [10] and is found by differentiating Equ. 1.47 with respect to α and found to be,

$$\alpha = \cos^{-1}\left[\exp\left(-\frac{TR}{T_1}\right)\right]. \tag{1.48}$$

For example, the grey and white matter of a healthy brain at 7T have T_1s of 2s and 1.2s respectively [11]. The flip angles needed to acquire the maximum signal, for a Turbo Field Echo (TFE) sequence with a TR of 50 ms, are 13° and 16° for grey and white matter.

Magnetisation Prepared Rapid Gradient Echo (MPRAGE) images provide excellent structural detail of both the grey and white matter. However, at 7T they are severely affected by B_1 inhomogeneity and was first developed in 1990 [12] and built upon the existing Turbo Field Echo sequence. MPRAGEs are T_1 weighted by preparing the longitudinal magnetisation with a tailored adiabatic inversion pulse [13] and excitation pulses of flip angle α used to measure the T_1 recovery.
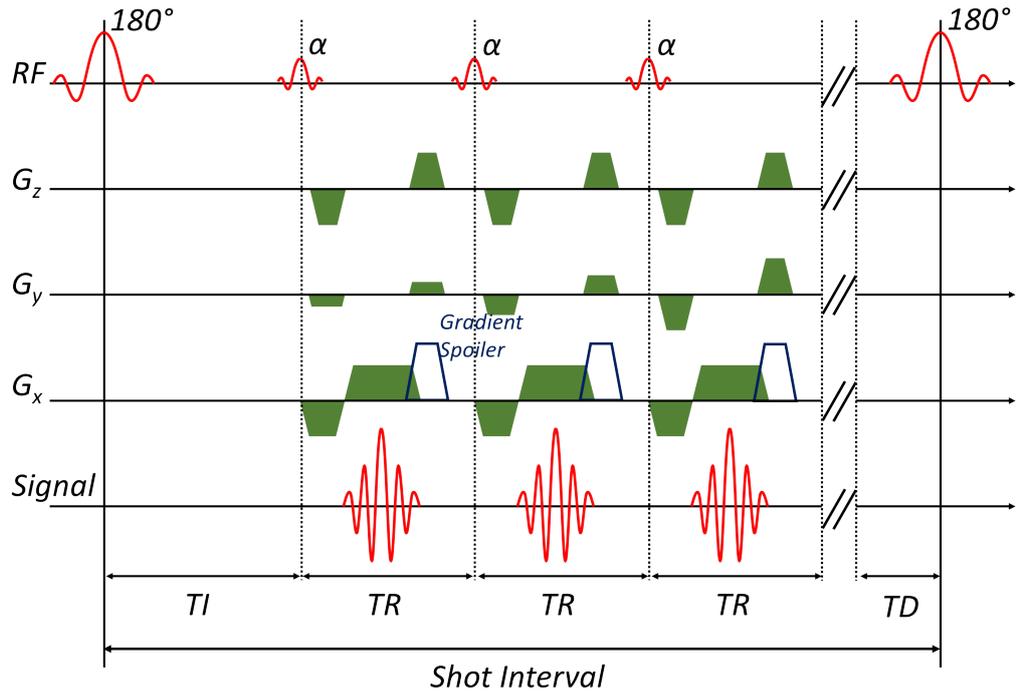
Figure 1.14: Magnetisation Prepared Rapid Gradient Echo (MPRAGE) sequence schematic.

The schematic of the T_1 weighted MPRAGE is shown in Figure 1.14. The inversion pulse at time $t = 0$ inverts the longitudinal magnetisation ($M_z = -M_0$) and after an inversion time TI (the time between the inversion and excitation readout) the TFE acquisition readout is played out.

TR is the repetition time between the excitation RF pulses of flip angle α whilst TE is the echo time of the individual GE readout. The number of pulses inside the train is called the TFE factor. Between the excitation pulses, a gradient spoiler crushes the transverse magnetisation and the delay between the end of the train and the next inversion pulse is called the time delay (TD). Pulses can be phase cycled to crush transverse magnetisation, instead of using gradients, to shorten the TR. The total time between inversion pulses is known as the shot interval, and between shots different lines of k-space are sampled to achieve a 3D image.

Echo Planar Imaging (EPI)

Echo Planar Imaging (EPI) was proposed by Mansfield in 1977 [14]. The technique is a significantly faster imaging modality compared to a spin warp acquisition, which has an RF excitation for each line of phase encoding. In EPI all lines in 2D planes of k-space are sampled within a single excitation shot, often within tens of milliseconds. EPI is used in to achieve high temporal resolution to allow the study of dynamic processes. Functional MRI (fMRI) requires a high temporal resolution to examine the haemodynamic response over a few seconds.
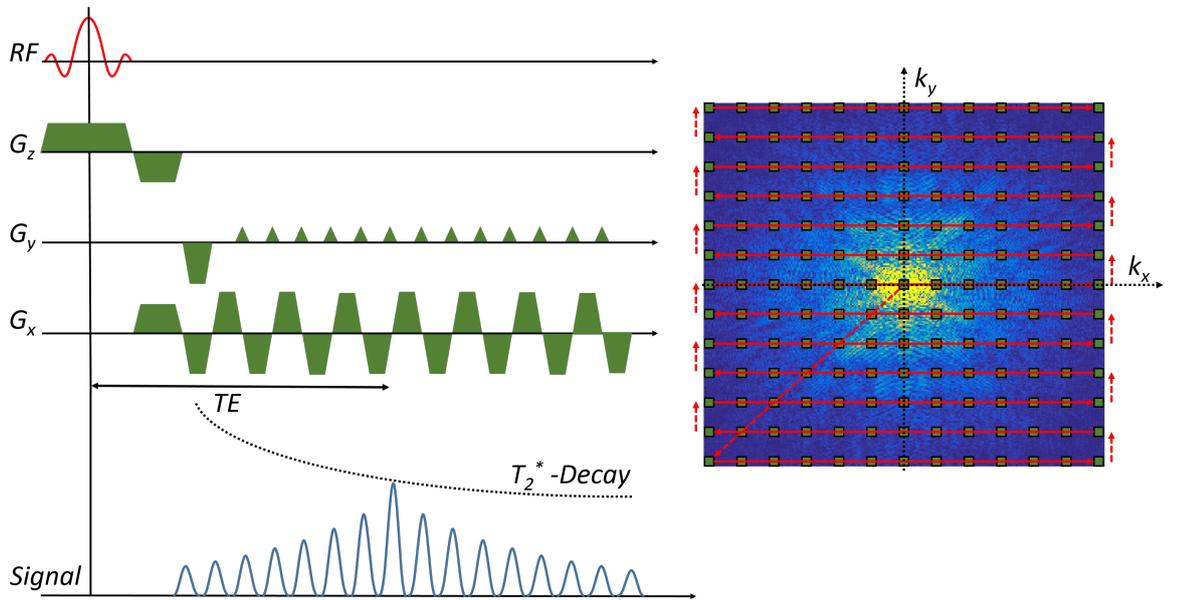
Figure 1.15: Schematic of Gradient Echo-EPI sequence (left) and the k-space trajectory (right).

A GE-EPI imaging sequence and k-space trajectory are shown in Figure 1.15. After the excitation pulse, negative lobes of the frequency and phase encoding gradients move the spin system to the outer edge of k-space. Once at $-k_{x,max}$ and $-k_{y,max}$ the frequency encoding gradient (G_x), used as the readout, is rapidly switched from positive to negative of equal amplitude and duration. As a result the transverse magnetisation is repeatedly refocused causing a train of gradient echoes as k_x plane is swept. Between the switching of the frequency encoding

gradients, small gradient blips in the phase encoding gradient G_y are applied to shift the trajectory in the k_y axis. As the lines of k-space are sampled in both directions, in order to produce an image, every other line of sampled k-space has to be time reversed before the Fourier Transform. This can cause so-called Nyquist ghost artefacts in images.

Field Mapping

Fast and robust *in vivo* B_0 and B_1 mapping is an essential prerequisite for quantitative MRI and multi-transmit applications.

B_0 Mapping

Measuring B_0 field inhomogeneities is possible using the dual gradient echo sequence, shown in Figure 1.16. The local B_0 field offset ΔB_z modifies the phase of the spins depending on the size of the frequency offset between the acquisition of two gradient echoes at different TEs. The phase difference between the two acquired images, $\Delta\phi(r)$ is proportional to the B_0 field inhomogeneity and the difference in echo time ΔTE,

$$\Delta\phi(r) = \gamma\Delta B_z\left(r\right)\Delta TE. \tag{1.49}$$

Therefore the spatial local B_0 magnetic field frequency offsets are found by measuring the phase difference between the two gradient echoes,

$$\Delta B_z\left(r\right) = \frac{\Delta\phi\left(r\right)}{\gamma\Delta TE}. \tag{1.50}$$

B_1 Mapping

The most accurate and reliable form of mapping the B_1 field requires the flip angle α over several images to be varied and fitted to a function $M_0\sin\left(c\alpha\right)$ to
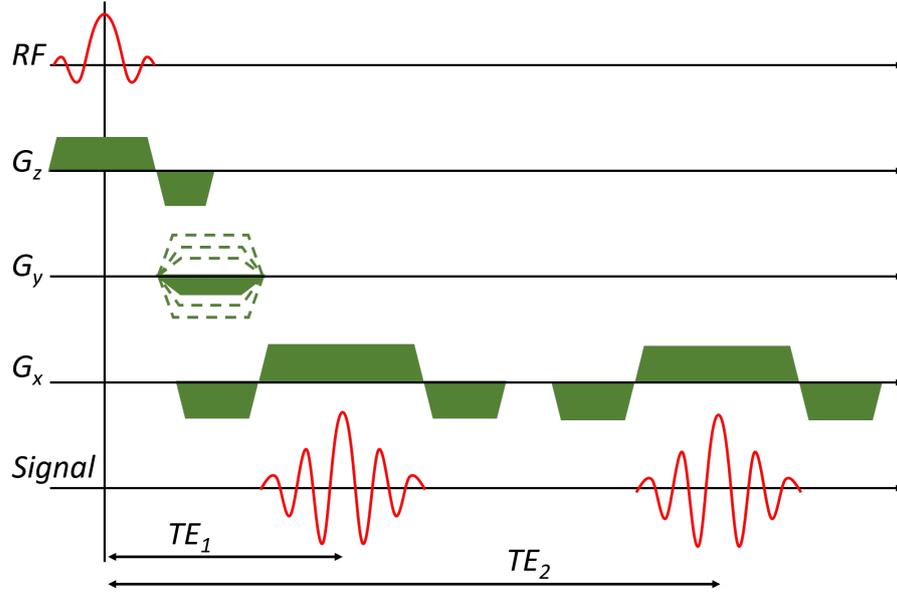
Figure 1.16: Dual Gradient Echo used to measure the B_0 field.

each of the image voxels, where c is the scale factor. However, this requires long TRs between the RF pulses to allow for the recovery of longitudinal magnetisation and therefore acquisition time would be too long to be feasible. Actual Flip-angle Imaging (AFI) [15] is a B_1 mapping technique that uses two identical RF excitation pulses, of flip angle α, with two delays of TR_1 and TR_2 which generate two signals S_1 and S_2, shown in Figure 1.17. The transverse magnetisation is spoiled between each acquisition as the longitudinal magnetisation has not completely recovered but results in shortened acquisition time. If the condition $TR_1 < TR_2 < T_1$ is met, the steady state signals recorded according to the Bloch equation are,

$$S_{1,2} = M_0 M_{t1,2} \exp\left(-\frac{TE}{T_2^*}\right), \tag{1.51}$$

where $M_{t1,2}$ are the normalised transversal steady state equilibrium magnetisation for the AFI dual TR sequence, and are is given as,

$$M_{t1,2} = \frac{1 - E_{2,1} + (1 - E_{1,2}) E_{2,1} \cos(\alpha)}{(1 - \cos^2(\alpha) E_1 E_2)} \tag{1.52}$$

and $E_{1,2} = \exp\left(-TR_{1,2}/T_1\right)$.

Taking the ratio, $r_{2,1}$, between the signals acquired by the two RF excitation pulses at two different TRs gives,

$$r_{2,1} = \frac{S_2}{S_1} = \frac{1 - E_1 + (1 - E_2)\, E_1 \cos\left(\alpha\right)}{1 - E_2 + (1 - E_1)\, E_2 \cos\left(\alpha\right)}. \tag{1.53}$$

Given the assumption that $TR_{1,2}/T_1 \ll 1$, a first order Taylor expansion of the exponential term in Equ. 1.53 can be taken such that,

$$r_{2,1} = \frac{1 + R \cos\left(\alpha\right)}{R + \cos\left(\alpha\right)}, \tag{1.54}$$

where $R = TR_2/TR_1$. Therefore an expression for the flip angle α is given by,

$$\alpha = \cos^{-1}\left(\frac{R r_{2,1} - 1}{R - r_{2,1}}\right). \tag{1.55}$$

Using this method a B_1 map of relative flip angle (fraction of measured flip angle vs target flip angle) across an image slice can be produced.
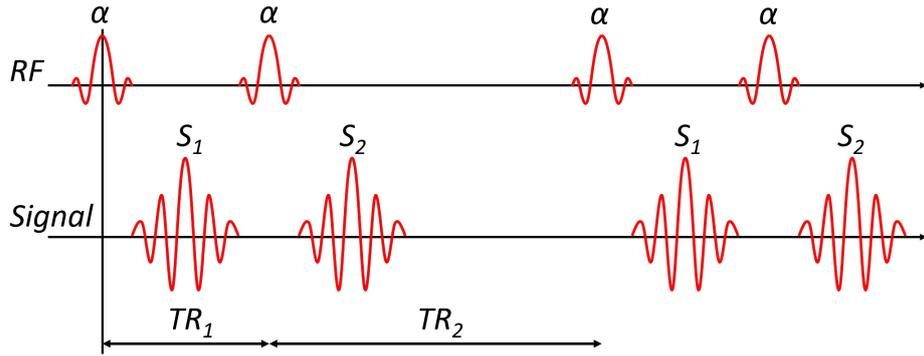
Figure 1.17: Timing diagram for the B_1 mapping sequence (API) showing RF pulses and detected signals for the two TRs.

1.4.4 Accelerating Image Acquisition

Segmented k-Space

Sequences that require a long echo time become more affected by T_2 and T_2^*, thus reducing the measured image quality. Segmenting the whole acquisition of k-space into multiple partial acquisitions results in reduced readout time. However, the overall time acquiring an MR image increases as additional RF excitations are required for each acquisition.

Partial Fourier Sampling

Another technique to speed up the acquisition times involves sampling half of k-space. A fully sampled k-space is composed of its complex conjugate, with the real component of the signal being symmetric about the centre, whilst the imaginary component is anti-symmetric. By sampling half or two-thirds of k-space, no contrast information is lost, as seen in Figure 1.18(e) and 1.18(f). The images in Figure 1.18 are reconstructed using the same Fourier Transform technique used in a fully sampled k-space. However, phase information is lost in partially sampled k-space and results in problems in correcting susceptibility artefacts. The SNR loss for the half sampled k-space is approximately 30% and therefore it is not always beneficial with reduction of acquisition times.

Sensitivity Encoding

Multi-coil arrays, first developed to improve SNR, can be used to speed up acquisition times. The Sensitivity Encoding (SENSE) reconstruction algorithm was proposed by Pruessmann [16] in 1999. To utilise the SENSE technique, the receiver coils must have multiple elements. Weighting the acquired images for each of the receive elements according to their spatial sensitivity profiles, results

(a) Full k-space sampled   **(b)** $1/2$ k-space sampled   **(c)** $2/3$ k-space sampled

(d) Reconstruction of (a)   **(e)** Reconstruction of (b)   **(f)** Reconstruction of (c)
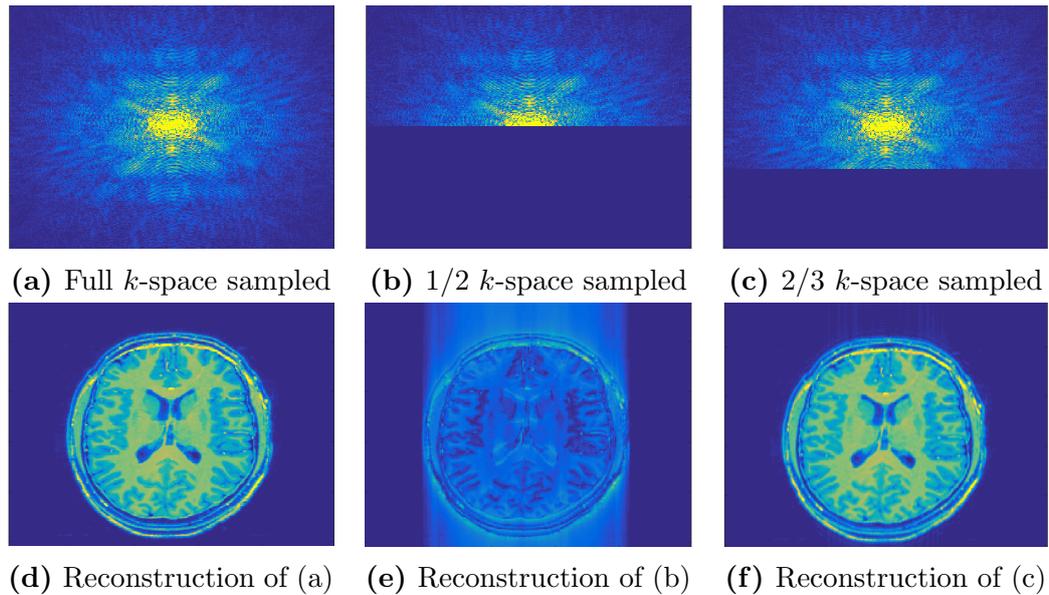
Figure 1.18: The representation of how k-space sampling affects the reconstruction of MR images.

in a complete image produced in a fraction of the time compared to a single element acquisition.

The overall time acquiring lines of k-space can be reduced by increasing the step size Δk_x and Δk_y, seen in Figure 1.12, whilst maintaining $k_{x,max}$ and $k_{y,max}$ ensuring spatial resolution, and the size of the FOV is not lost. The amount by which the sampled k-space is reduced is known as the SENSE factor. Reducing the sampling frequency, in the case where SENSE is not used, would result in a reduced FOV and aliasing. Aliasing like this causes signal outside the FOV to be folded back into the image. Using the sensitivity profiles of each of the receive elements, the image signals measured at each element can be reconstructed to produce a full FOV image.

1.5   Summary

This chapter has introduced the basics principles of NMR and MRI needed to understand the work presented in this thesis. Including the fundamentals of spin

relaxation and field mapping that are needed in understanding and analysing chemical exchange saturation transfer (CEST) contrast presented in Chapters 3 & 4.

Bibliography

[1] Bloch, F. Nuclear induction. *Physical review* **70**, 460 (1946).

[2] Purcell, E. M., Torrey, H. & Pound, R. V. Resonance absorption by nuclear magnetic moments in a solid. *Physical review* **69**, 37 (1946).

[3] Carr, H. Y. & Purcell, E. M. Effects of Diffusion on Free Precession in Nuclear Magnetic Resonance Experiments. *Phys. Rev.* **94**, 630–638 (1954).

[4] Lauterbur, P. C. Image formation by induced local interactions: examples employing nuclear magnetic resonance (1973).

[5] Mansfield, P. & Grannell, P. K. NMR diffraction in solids. *Journal of Physics C: solid state physics* **6**, L422 (1973).

[6] Garroway, A. N., Grannell, P. K. & Mansfield, P. Image formation in NMR by a selective irradiative process. *Journal of Physics C: Solid State Physics* **7**, L457 (1974).

[7] Kumar, A., Welti, D. & Ernst, R. R. NMR Fourier zeugmatography. *Journal of Magnetic Resonance* **18**, 69–83 (1975).

[8] Coxon, R. & Mansfield, P. EPI spatial distortion in non-transverse planes. In *Proc., SMRM, 8th Annual Meeting, Amsterdam*, 361 (1989).

[9] Ljunggren, S. A simple graphical representation of Fourier-based imaging methods. *Journal of Magnetic Resonance (1969)* **54**, 338–343 (1983).

[10] Ernst, R. & Anderson, W. Application of Fourier transform spectroscopy to magnetic resonance. *Review of Scientific Instruments* **37**, 93–102 (1966).

[11] Wright, P. *et al.* Water proton T1 measurements in brain tissue at 7, 3, and 1.5 T using IR-EPI, IR-TSE, and MPRAGE: results and optimization. *Magnetic Resonance Materials in Physics, Biology and Medicine* **21**, 121–130 (2008).

Bibliography

[12] Mugler, J. P. & Brookeman, J. R. Three-dimensional magnetization-prepared rapid gradient-echo imaging (3D MP RAGE). *Magnetic Resonance in Medicine* **15**, 152–157 (1990).

[13] Hurley, A. C. *et al.* Tailored RF pulse for magnetization inversion at ultra-high field. *Magnetic Resonance in Medicine* **63**, 51–58 (2010).

[14] Mansfield, P. Multi-planar image formation using NMR spin echoes. *Journal of Physics C: Solid State Physics* **10**, L55 (1977).

[15] Yarnykh, V. L. Actual flip-angle imaging in the pulsed steady state: a method for rapid three-dimensional mapping of the transmitted radiofrequency field. *Magnetic resonance in medicine official journal of the Society of Magnetic Resonance in Medicine Society of Magnetic Resonance in Medicine* **57**, 192–200 (2007).

[16] Pruessmann, K. P., Weiger, M., Scheidegger, M. B., Boesiger, P. *et al.* SENSE: sensitivity encoding for fast MRI. *Magnetic resonance in medicine* **42**, 952–962 (1999).

Chapter 2

Improving the B_1 Transmit Field at 7T

2.1 Introduction

MRI over the years has developed into one of the most flexible tools in medical research and diagnostic imaging. There are over 20,000 clinical MR systems currently in the world [1], of which the majority are at low field (3T or below). Only ~ 50 scanners are at 7T or above and are currently for research purposes only. The vast majority of research using ultra high field MRI (defined as 7 Tesla or greater) is conducted on the human brain, although recently there has been a move towards abdominal imaging at 7T [2]. The structure and function of the human brain is complex making it a very active area of research. In a clinical setting, MRI scanners are typically 1.5 or 3 Tesla, as it is possible to achieve high quality images of the brain anatomy for a fraction of the price as compared to 7T. However, the lower SNR at these field strengths limits the evaluation of subtle abnormalities that become enhanced at 7T, providing access to new contrast mechanisms. In the following chapter the hardware behind a 7T system will be outlined along with a discussion of the advantages and technical challenges of imaging at ultra high field. Finally the use of dielectric pads and multi-transmit RF pulse design are presented as potential solutions to overcome B_1 field inhomogeneities that are a major challenge at 7T.

2.2 Hardware

All the work conducted in this thesis was performed on a Philips Achieva 7T system (Best, Netherlands). Figure 2.1 shows the schematic of an MRI scanner, like the one used in the research conducted.
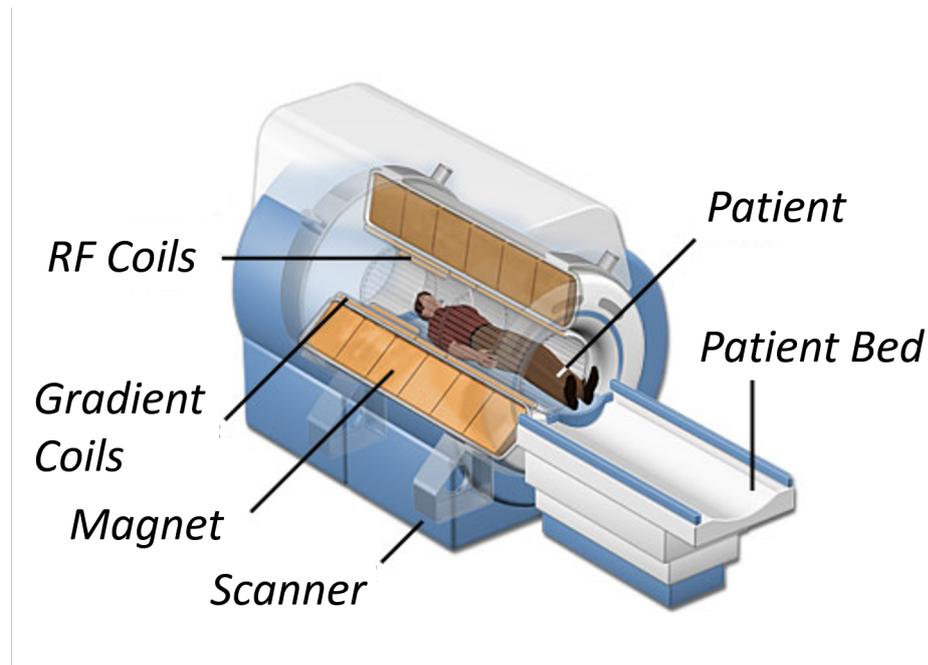
Figure 2.1: Schematic of a whole-body MRI scanner indicating the location of the main magnet, gradient and RF coils.

2.2.1 Main Magnet

The largest component of the scanner is the superconducting electromagnet that produces the static 7 Tesla B_0 field with a bore size of ~ 90 cm. It is important that the main magnetic field is spatially uniform and has good temporal stability. To achieve a homogeneous magnetic field over such a region, a cylindrical coil of superconducting current-carrying wires is kept below 10 K using liquid helium and a cryocooler which acts as a refrigeration unit. The Philips 7T system has a field homogeneity of ~ 0.10 ppm in a 25 cm diameter spherical volume at the isocentre of the magnet. The main magnet has a fringe field that needs to

be considered, in terms of safety. Areas where the magnetic field is above 0.5 mT (5 Gauss) have restricted access, to prevent anyone with contraindications to large magnetic fields being exposed. To limit the size of the fringe field in Nottingham and to bring the 5 Guass line to just inside the control room, the magnet is housed in a room surrounded by 200 Tonnes of passive iron shielding as the 7T scanner is not actively shielded like common clinical scanners.

2.2.2 Shimming System

From an engineer's point of view, it is difficult to construct a magnet which produces a homogeneous B_0 field predicted by theoretical design. Furthermore, when a subject is placed in the bore of the magnet, the field becomes distorted by the small susceptibility differences between different materials in the subject. Other sources of inhomogeneities induced in the B_0 field arise from problems associated with the construction process such as wire distribution, wires shifting due to the passive magnet force, and magnet stresses during transportation.

There are two methods of B_0 field shimming: passive and active. Passive shimming consists of placing pieces of iron inside the magnet, near to the imaging region along the bore circumference to counteract the field shifts. Active shimming corrects inhomogeneities in the B_0 field by varying the electric current through coils; known as shim coils, placed inside the bore of the magnet, generating spherical harmonic fields. The currents are varied constantly in an iterative process to correct the field until the target field is achieved. On the Philips 7T system there is an auto-shimming sequence before every scan in which an FID signal is measured in the absence of any switched gradient fields to measure the field homogeneity. Through adjustment of the shim currents, the largest amplitude FID is found [3, 4]. There are other methods of shimming, based on field mapping techniques, where a spatial map of B_0 is used.

2.2.3 Gradient Coils

Gradient coils are located just inside the shim coils and are used to produce spatially varying magnetic fields in x, y and z directions. The gradients are used to manipulate the spins so they can be localised spatially, as described in Section 1.4.1. The currents passed through the gradient coils can switch rapidly during imaging sequences. EPI based methods are an example of this and induce electric fields in human tissue causing stimulation of peripheral nerves and this effect is called Peripheral Nerve Stimulation (PNS). To limit PNS the maximum gradient field strength on the system is 40 mT/m with a slew rate of 200 mT/m/ms.

2.2.4 Radio Frequency Coils

Radio frequency (RF) coils have two primary functions in MRI: to transmit an oscillating transverse B_1 field to excite the magnetisation, by tipping it away from the longitudinal axis into the transverse plane and the other function is to receive the NMR signal whilst the magnetisation is away from equilibrium M_0. The excited spins precess at the Larmor frequency ω_0. As the spins precess they create a changing magnetic flux and according to Faraday's law, this induces an alternating voltage that is picked up by the RF receiver coils (which may be the same as the transmit coil). It is this voltage signal that is used for image reconstruction and the total signal detected by the receive coils is the sum of all the excited magnetisation within the imaging volume, and does not contain any useful spatial information. Spatial encoding gradient coils are used to obtain the spatial information to produce an MR image.

2.3 Safety Considerations

It is important to consider the safety concerns that may be present when conducting an experiment using MRI. The large static magnetic field has a number of potentially adverse effects on subjects or operators.

Ferromagnetic attraction associated with magnetic fields is the largest risk. Any ferromagnetic object taken within the vicinity of a scanner will experience a force. Loose objects can become projectiles and may cause injury or even have lethal consequences for anyone within the flight path. The static magnetic field can also interfere with implants. For example, pacemakers may malfunction and aneurysm clips can be pulled causing internal haemorrhaging. A careful screening process for volunteers and patients before they enter areas within the 5 Gauss line is conducted to ensure all metal objects have been removed and all safety procedures are understood, reducing the risk that any hazardous materials enter the magnet hall.

There have been no reports of any long-term adverse biological effects caused by large static magnetic fields [5]. However, it is widely reported that volunteers can experience a metallic taste and/or vertigo when exposed to high magnetic fields and moved through large field gradients [6]. These effects do not physically harm the subjects but may make them very uncomfortable and can be minimised by limiting the speed that a volunteer moves through the field to the isocentre. Peripheral nerve stimulation (PNS) [7] typically causes volunteers to experience tingling or slight tremors in their shoulders and/or back but has no apparent long-term effects.

A large part of the RF power transmitted to the tissue to excite the spins is transformed into heat as a result of resistive losses and is characterised by the Specific Absorption Rate (SAR), a mass normalised rate at which RF power is coupled to biologic tissue and is expressed in units of watts per kilogram (W/kg).

2.4 Advantages and Technical Challenges of Ultra High Field MRI

In the history of MRI, the increase in the B_0 field strength has always been associated with technical challenges initially. However, once overcome, the advantages of higher field strength have been instrumental in forming new medical diagnostics.

2.4.1 Advantages

Signal to Noise Ratio

The Signal to Noise Ratio (SNR) is associated with increased spin polarisation governed by Equ. 1.12 and increases linearly with main magnetic field strength B_0 up to 4T [8]. Beyond magnetic field strengths of 4T, the SNR varies spatially as a function of the B_1 field inhomogeneity, making it more complex to quantify. In a comparison between human brain imaging at 4T and 7T, an average SNR increase of 1.76 was recorded [9]. However, the increase in SNR was spatially dependent, with an increase of 2.1 in the centre of the head (where B_1 is the highest) and 1.4 at the periphery. The increased available SNR can be traded off for increased spatial resolution or reduced image acquisition time [10, 11].

Chemical Shift and Spectral Resolution

Spectral resolution increases as B_0 increases, and combined with increased SNR this means that metabolites of smaller concentration can be detected where previously it was not possible. For instance, at lower field, the natural linewidth of Glutamine and Gluamate overlap [12], but they are seperable at 7T. For Chemical Exchange Saturation Transfer (CEST), the chemical shift between two exchanging chemical sites increases with B_0 so that the exchange rates can

move from the fast exchanging limit to the slow regime resulting in better detection in z-spectroscopy (outlined in greater detail in Chapter 3). The increased sensitivity to metabolites can also result in shorter acquisition times or reducing the volume of the region of interest. This has resulted in Chemical Shift Imaging (CSI) becoming more useful at 7T [13].

Susceptibility Contrast

Greater contrast to susceptibility effects occur at ultra high field as T_2^* shortens with increased B_0 and has resulted in a contrast known as Susceptibility Weighed Imaging (SWI) [14]. SWI has excellent vascular imaging contrast when compared to lower field strengths. Susceptibility differences between tissues of paramagnetic ($\chi > 0$) and diamagnetic ($\chi < 0$) content are differentiated with Quantitative Susceptibility Mapping (QSM) [15]. QSM is used to map iron (ferritin) content [16] and levels of oxygen saturation [17].

Susceptibility effects are used to monitor dynamic changes in the brain, such as perfusion and Blood Oxygen Level Dependent (BOLD) contrast. For BOLD imaging the move from 3T to 7T is reported to result in a twofold increase in the measured ΔR_2^* between resting state and motor cortex activation [18]. Again, this is typically traded off to increase the spatial resolution which can actually increase local SNR by reducing intravoxel dephasing [19].

Relaxation Times

The proton T_1 relaxation time of brain tissue significantly increases from 1.5T to 7T. Longer T_1 is advantageous for the sensitivity of Arterial Spin Labelling (ASL) and Chemical Exchange Saturation Transfer (CEST). However, acquisition times are generally longer with increased T_1.

2.4.2 Technical Challenges

Moving to higher B_0 magnetic field strength in MRI has always been associated with technical challenges and can be separated into two types: manufacturing or user-based challenges. The manufacturing, technical challenges are associated with the construction of the superconducting magnets and attempts to actively shield the magnets. It costs $\sim$ £1 million per Tesla to build and install a new scanner [20]. The user-based challenges are the restrictions and negative impacts upon image quality and are outlined below.

Specific Absorption Rate (SAR)

Tissue heating due to the power deposition from RF pulses is measured by the parameter SAR (Specific Absorption Rate). Power deposited by RF pulses increases quadratically with field strengths up to 4.7T [21]. Power deposition is limited and restrictions are set out by the SAR guidelines. SAR measures the amount of RF energy deposited in a subject during a scan and is measured in watts per kilogram. SAR particularly limits the number of saturation or refocusing pulses delivered per unit time, as these require high power to saturate or invert the magnetisation respectively. Additionally complications arise from the spatial varying B_1 transmit field that can result in local SAR hotspots [22].

Effects on Relaxation

There are some advantages to be gained from longer T_1 recovery. However, in principle the T_1 times converge for the different tissue types in the brain at higher B_0, and as a consequence there is less contrast between them, although in practice this is not a problem at 7T. Longer TRs are required in experiments where the longitudinal magnetisation must be fully recovered and this extends the acquisition times.

2.4. Advantages and Technical Challenges of Ultra High Field MRI

More problematic is the effect on T_2 and T_2^* and image acquisition. In theory T_2 should not be affected by the larger B_0 field. However, T_2 becomes shorter in spin-echo sequences which causes problems in diffusion weighted imaging that require long TEs. Shorter T_2^* affects the signal contrast observed in GE sequences and so shorter TEs are used to overcome this problem.

Susceptibility

Spatial encoding (outlined in Section 1.4.1) requires a homogeneous B_0 field within the imaging volume otherwise artefacts manifest themselves in the re-constructed images, particularly affecting GE sequences. Regions where the differences in local susceptibility in tissue, such as the sinuses or near metal implants, $|\Delta\chi|$ increases and larger spatial variations in magnetic fields are observed. The overall effect of the B_0 field inhomogeneities on the reconstructed images depends upon the magnitude of the field perturbation and also on the imaging pixels' dimensions and bandwidth. When the field perturbation occurs within an imaging voxel, there is an increased rate of signal decay affecting the measurement of T_2^* and this causes image blurring. On the other hand, field perturbations that occur over larger distances (i.e. over several imaging voxels) give rise to geometric distortions due to signal mis-localisation.

B_1 Field Inhomogeneity

At 7T the spatial phase interactions of the electromagnetic fields in a medium become more complex and can notably affect image quality. The increase in the Larmor frequency ω_0 results directly in reduction of the wavelength of B_1. At 7T the wavelength of the electromagnetic waves in tissue becomes comparable to the dimensions of the head and leads to the creation of standing wave interference patterns across the head. This effect manifests in B_1 field inhomogeneities in both the transmit and receive fields, and B_1 field inhomogeneities result in spatial dependence on the achieved flip angle of RF pulses. In the worse cases

RF pulses can result in no excitation where there is severe destructive inter-
ference. Gaussian filtering methods are used to remove the central brightening
seen in images but these do not correct the signal losses in areas of low or no
excitation, and as such results in a loss of SNR. There have been attempts at
solutions to B_1 inhomogeneity problems, two of which are outlined in Section
2.5.

Motion Artefacts

As the isotropic resolution of the images becomes higher, motion artefacts can
begin to manifest themselves particularly in long acquisition based imaging.
Whilst patient comfort is of the upmost importance, so is ensuring that move-
ment is minimised. Motion can sometimes be corrected for in post-processing
but only if the subject has moved between scan or scans with multiple dynamics.
Movement within the acquisition, for example a 3D k-space acquisition, is very
difficult/impossible to correct for and causes a blurring or ghosting artefact.
Techniques using cameras to monitor movement of a subject have been devel-
oped, feeding a position measurement back in real time to allow the scanner to
adjust the k-space position [23].

2.5   Improving B_1 Homogeneity

To overcome B_1 field inhomogeneities a number of solutions have been proposed.
In the following section, a quantitative description is given of the benefits of util-
ising dielectric pads which alter the spatial distribution of the electromagnetic
field, improving B_1 in regions of interest where signal is normally lost. Also,
multi-transmit technology and RF pulse design to improve B_1 homogeneity will
be described along with the simulation of a slice selective RF spokes sequence
to improve the B_1 field.

2.5.1 Dielectric Pads

At 7T the central brightening in structural anatomical images occurs as the RF wavelength is comparable in length to the diameter of the head [24]. Figure 2.2 shows the central brightening and the signal drop-off at the outer regions of the brain in a T_1 weighted MPRAGE image at 7T. High permittivity materials can be used in MRI to alter the spatial distribution of the B_1 field, increasing the strength of the B_1^+ transmit and B_1^- receive magnetic fields in regions where there is intrinsically low sensitivity, such as the cerebellum and temporal lope. The spatially varying B_1 field within the transmit coil is dependent on the electrical properties, geometry and relative position of the sample within the coil [9, 25]. Dielectric pads are used either to locally enhance fields to increase sensitivity in a region of interest close to the pads or to shim the B_1 field to compensate for the central brightening artefact [26].
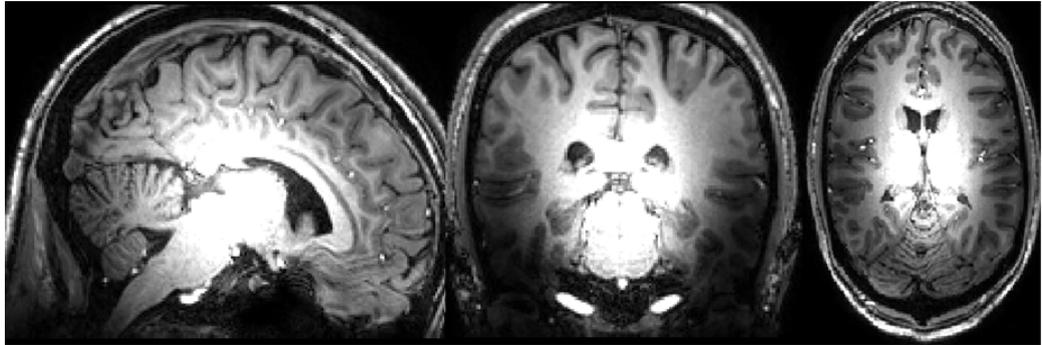
Figure 2.2: Magnetisation Prepared Rapid Gradient Echo (MPRAGE) image showing the central brightening caused by B_1 inhomogeneities in the sagittal, coronal and transverse planes.

Theory

The RF field within a conductive material, such as the human brain, is perturbed according to Ampere's law by conductive current $\mathbf{J}_c$ and displacement current $\mathbf{J}_d$,

2.5. Improving B_1 Homogeneity

$$\nabla \times \mathbf{B} = \mu \left(\mathbf{J}_c + \mathbf{J}_d \right) = \mu \sigma \mathbf{E} + i \mu \epsilon_r \epsilon_0 \omega_0 \mathbf{E}, \tag{2.1}$$

where $\mathbf{B}$ is the magnetic flux density, $\mathbf{E}$ is the electric field, ω_0 the Larmor frequency, ϵ_r and ϵ_0 is the relative and vacuum electric permittivity respectively, μ is the magnetic permeability and i is the complex unit that represents a 90° phase shift between the conductive and displacement currents. As an RF wave travels through a homogeneous medium, the conductive current $\mathbf{J}_c$ results in a decay of the RF field in the propagation direction whilst the displacement current, that has a phase shift of 90°, acts as a secondary field allowing the RF wave to propagate through the medium. Therefore the contribution of the two opposing current sources to the B_1 transmit field can be taken as a ratio of the conductive current $\mathbf{J}_c$ and displacement current $\mathbf{J}_d$,

$$\frac{\mathbf{J}_c}{\mathbf{J}_d} = \frac{\sigma}{\omega_0 \epsilon_0 \epsilon_r}. \tag{2.2}$$

Therefore a dielectric material with a high ϵ_r and a low σ can disturb the local B_1 field strength particularly when placed near the region of interest as the induced displacement current becomes greater than the conducting current. This results in more of the RF electromagnetic wave depositing its energy in regions nearer the dielectric pads and improving the B_1 field in these regions.

Methods

A quantitative assessment of the two sets of dielectric pads was conducted. The first set of dielectric pads (consisting of two pads connected together) were provided by Leiden University [26], had dimensions of $18 \times 18 \times 0.8$ cm^3 and contained a 2.8:1 ratio of calcium titanate ($\epsilon_r \sim 110$) and deuterated water. The second smaller dielectric pad of dimensions $15 \times 10 \times 1$ cm^3 was made to ratio of 20% Barium titanate ($\epsilon_r \sim 140$) and deuterated water. The placement of the dielectric pads differed during scanning. The large pads, as in [26], were placed

over the head covering the ears before moving the volunteer into the head coil (Figure 2.3(a)) and the smaller pad was placed at the base of the head and neck (Figure 2.3(b)), close to the cerebellum.

(a) Large Dielectric Pad   **(b)** Small Dielectric Pad
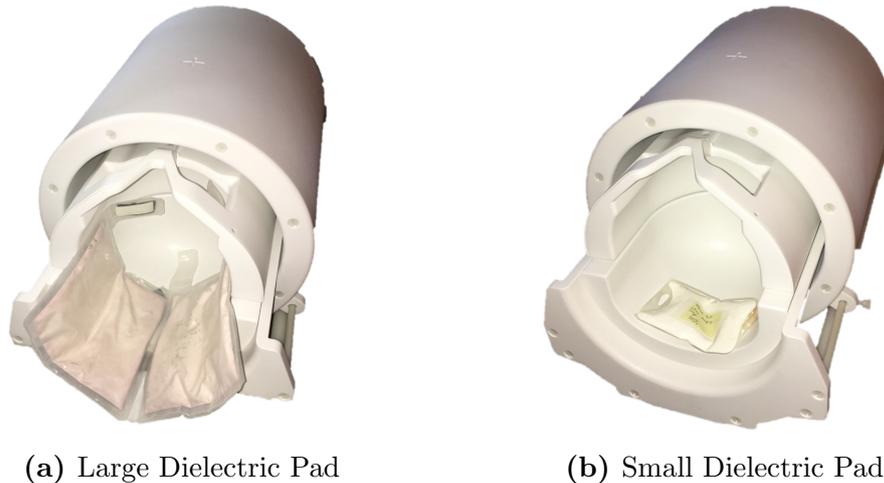
Figure 2.3: The positioning of the (a) large and (b) small dielectric pads in the Nova Medical volume transmit/receive coil.

For both the large and small dielectric pads, a T_1 weighted MPRAGE (described in Section 1.4.3) structural anatomical scan (which is severely affected by B_1 inhomogeneity) was collected. B_1 and B_0 field maps (also outlined in Section 1.4.3) were collected to assess the field changes that both sets of pads caused. In total three sets of scans were collected: no dielectric pads, large dielectric pads and small dielectric pads.

Prior to analysis the MPRAGE, B_0 and B_1 maps were co-registered using FSL[1] onto the same image space and the brain region extracted from the skull.

Results

Figure 2.4 shows the three collected MPRAGEs and the percentage Signal Increase (SI) between large or small dielectric pads and no pads. For the large dielectric pads, the central brighting in the MPRAGE images appears stretched out and the measured signal increased by over 200% in regions close to the pads

---

[1]FMRIB Software Library v6, fsl.fmrib.ox.ac.uk
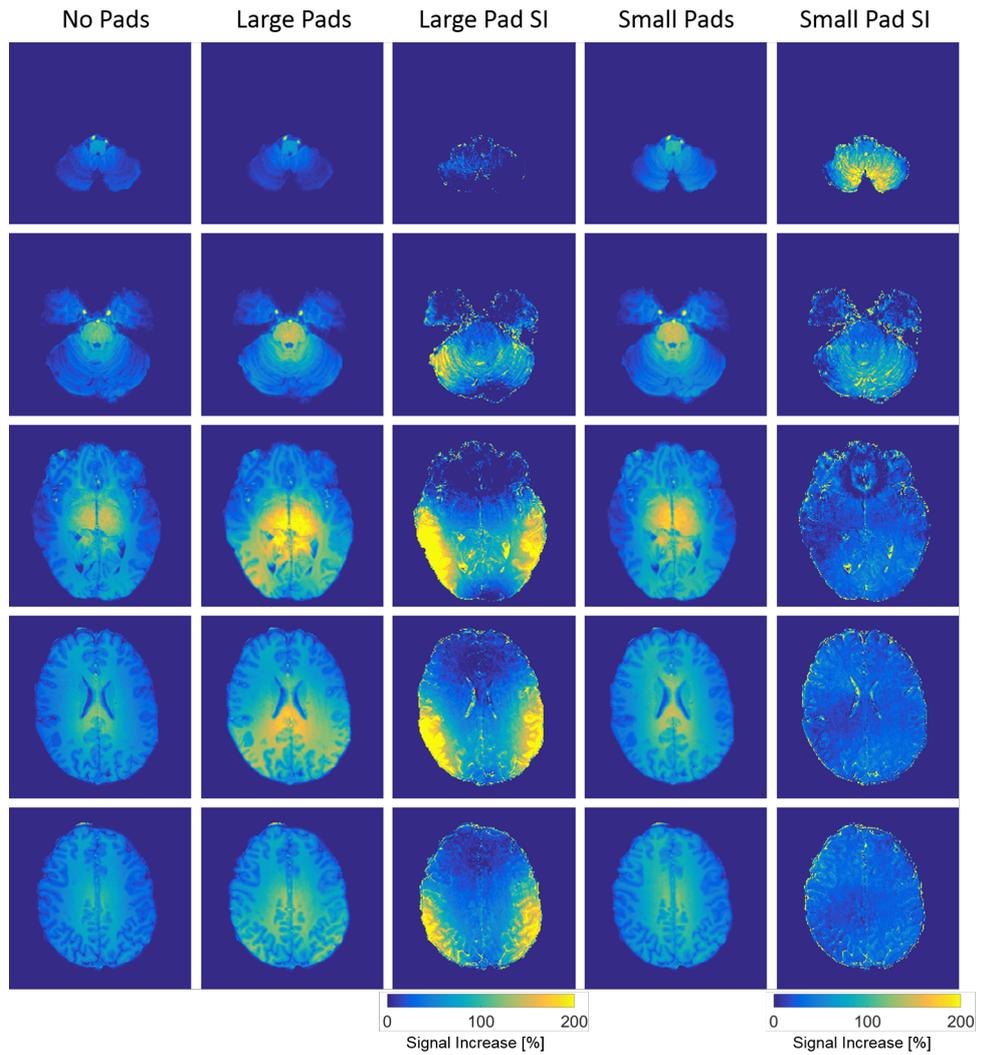
Figure 2.4: MPRAGE images with no dielectric pads, small and large dielectric pads (set to the same scale) and the percentage Signal Increase (SI) between small or large dielectric pads and no pads.

such as the temporal lobes. For the smaller dielectric pads, which are placed near the cerebellum, the signal increased by over 150%.

As previously reported, the dielectric pads have no detrimental effect on the B_0 field [26] and is confirmed in Figure 2.5. The B_1 field is, however, affected by the placement of the dielectric pads, which is expected. Inspection of the B_1 maps in Figure 2.5, confirms that the large pads draw out the B_1 field away from the centre of the brain. Histograms of the percentage of achieved flip angle for the whole head are shown in Figure 2.6 and indicate that neither the (b) large or (c)
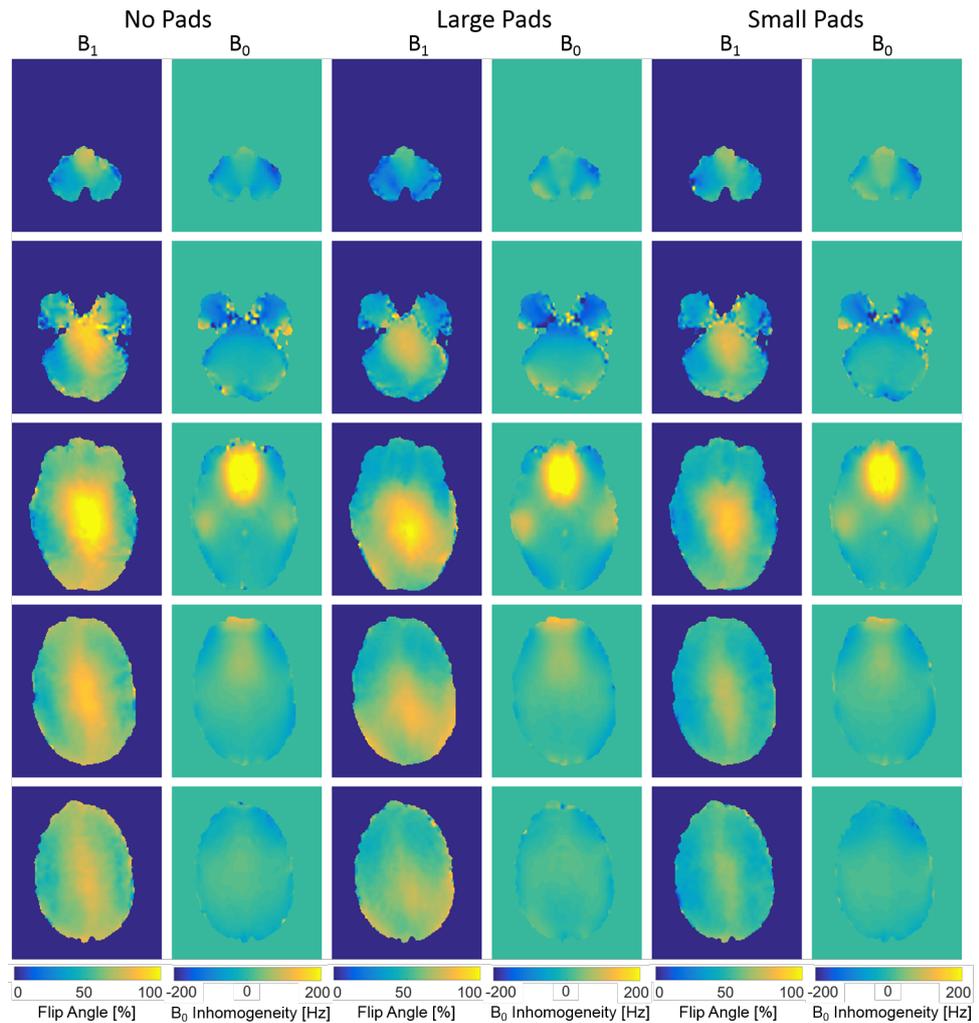
Figure 2.5: The B_0 (in Hz) and B_1 (in percentage of achieved flip angle) field maps for the large, small and no dielectric pads.

small dielectric pads improve the overall B_1 homogeneity across the whole head. Focusing on the achieved flip angle in the cerebellum, the histogram for the small dielectric pads, Figure 2.6(f) shows an increase in the expected flip angle and a bi-modal distribution, which accounts for the higher percentage of expected flip angle achieved and larger standard deviation in comparison to large dielectric pads or no dielectric pads at all. The large dielectric pads improved the B_1 field in the temporal lope, close to where the pads are placed, and in Figure 2.6(h) the histogram shows there is higher expected flip angle achieved compared to small or no dielectric pads.
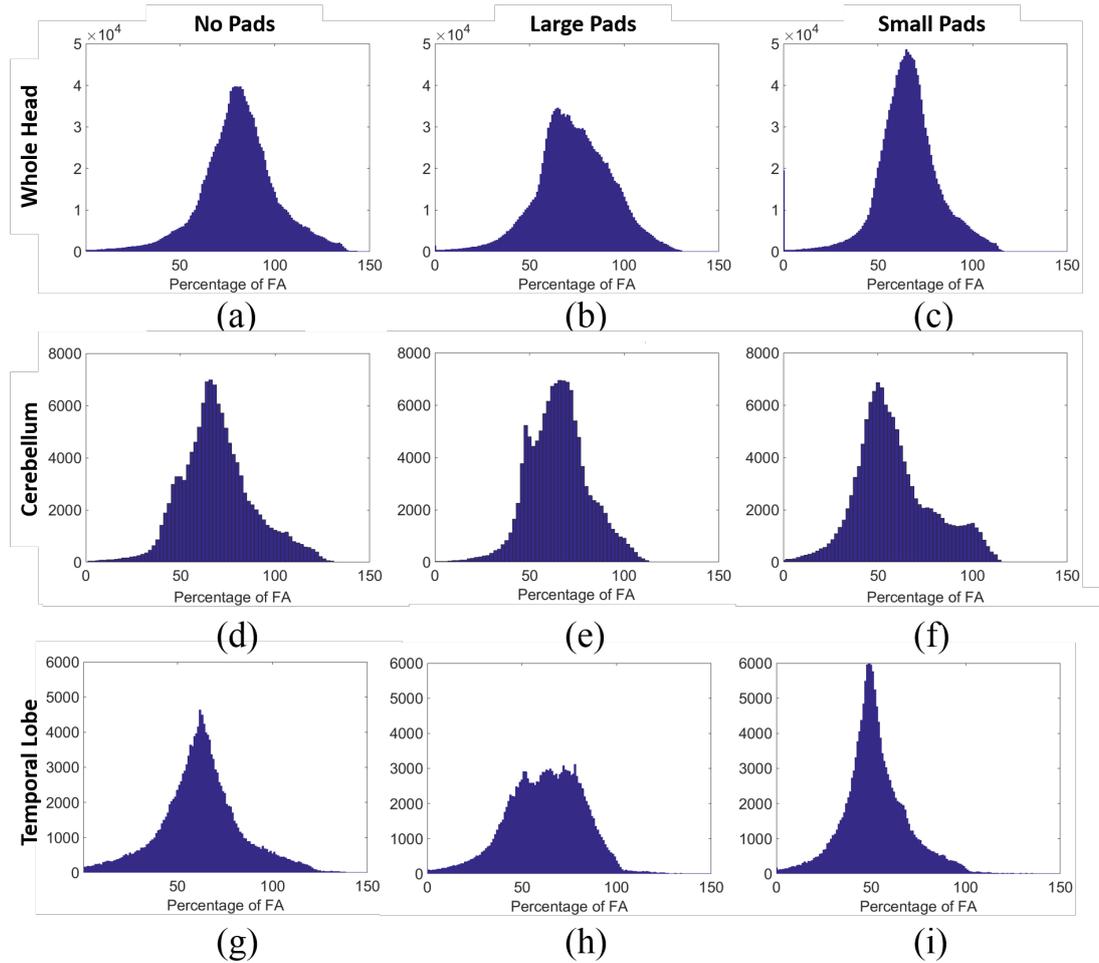
Figure 2.6: Histograms for the achieved flip angle: (a-c) whole head for no dielectric pads, large and small dielectric pads respectively. (d-f) the cerebellum for no dielectric pads, large and small dielectric pads respectively. (g-i) the temporal lobes for no dielectric pads, large and small dielectric pads respectively.

Discussion

The results presented indicate that dielectric pads provide a very efficient method of improving the B_1 field and signal intensity in MPRAGE sequences in ROIs close to the skull, like the cerebellum or the temporal lobes where dielectric pads can be placed nearby. The flexibility of the dielectric pads allows them to be positioned in the best location to improve the B_1 field depending on the ROI being examined. What dielectric pads fail to do is improve the B_1 field homogeneity across the whole head which in many cases is of greater importance. Whilst it

has been reported that the dielectric pads do not cause any significant increase in the SAR [26] and have been used to reduce SAR [27] at 3T, careful modelling of their impact on SAR distribution must be made before wider adoption. In the experiments carried out above, all of the scans had a low global SAR to ensure that even if there was an increase in local SAR near the dielectric pads it would not harm the volunteer. There are also practical issues still to be addressed, for example, the size of the dielectric pads and the position in which they are placed in the RF transmit coil. The size and geometry of the pads need careful design as, for example, the space within the 32 channel receive coil used in the experiments above meant that only volunteers with small heads (head circumference 56.6 cm) could fit inside the coil with the large pads positioned over their heads. Also, both the dielectric pads contain liquid and so sealing them to ensure they do not leak is also important.

2.5.2 Multi-Transmit

Multi-transmit RF technology is the most flexible approach to manipulating the B_1 transmit field to achieve flip angle uniformity. First proposed by Hoult and Ibrahim in 2000 [28, 29], the architecture of the RF system is changed. Standard, quadrature based, RF transmit coils are driven by a single RF amplifier and a fixed phase shift is applied between the transmit channels. Multi-transmit systems, however, have RF amplifiers for each separate transmit coil element, allowing for full control of the amplitude and phase of the RF waveforms from each element.

Initially multi-transmit was used for static B_1 adjustment of each channel much like image based B_0 shimming methods, termed as static B_1 shimming. However, Katscher [30] and Zhu [31] both independently proposed exploiting of full spatial and temporal control of the B_1 transmit field. All multi-transmit excitation methods require prior knowledge of the B_1 transmit field, using a B_1 field map (Section 1.4.3), from each of the coil elements, analogous to the sensitivity

2.5. Improving B_1 Homogeneity

profiles used in SENSE reconstruction [32]. The magnitude and phase B_1 transmit sensitivity profiles for a two-channel (Nova Medical) transmit coil used on a Philips 7T Achieva system are shown in Figure 2.7. Currently, multi-transmit B_1 excitation has two aims: uniform B_1 homogeneity or local excitation which can be achieved using either static or dynamic shimming techniques.
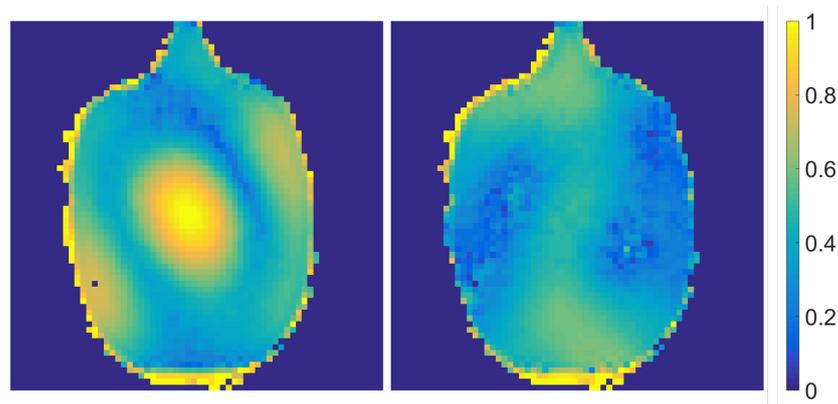
(a) Nominal B_1 magnitude profiles for both RF transmit channels
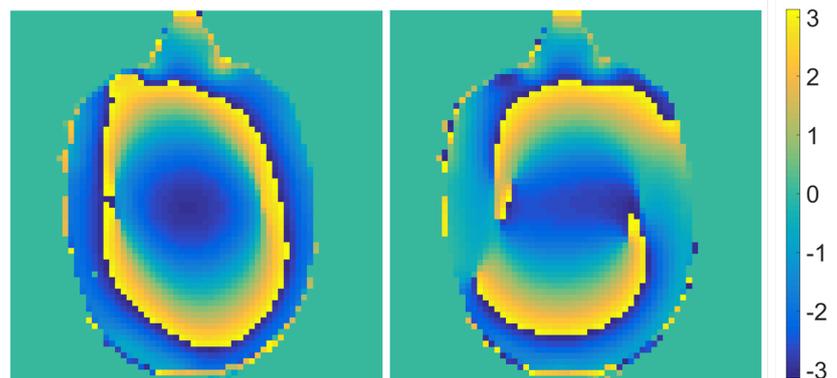
(b) Phase profiles for both RF transmit channels

Figure 2.7: The (a) magnitude and (b) phase B_1 transmit sensitivity profiles from a two channel head transmit coil.

Static B_1 shimming is the most basic form of B_1 field shimming using multi-transmit and has the ultimate goal of achieving an optimum B_1 field. The B_1 transmit sensitivity profiles $S_j(\mathbf{r})$ for the jth transmit coil contain the amplitude of the RF field and the relative phase between the transmit coils. The net B_1 transmit field, according to the principle of superposition, is the sum of the fields due to each of the transmit channels such that,

$$B_1 (\mathbf{r}, t) = \sum_{j=1}^{N_c} B_{1,j} (\mathbf{r}, t) = b_j (t) \sum_{j=1}^{N_c} w_j S_j (\mathbf{r}), \qquad (2.3)$$

where $b_j (t)$ is the time evolution of the RF waveform and w_j are the complex weights applied to each channel. The B_1 field within an ROI is manipulated by adjusting the complex weights in Equ. 2.3, and the optimal weights are typically determined using iterative cost function. The optimisation can also include weightings to limit SAR or the excitation selectivity. The principle of superposition of the sensitivity profiles to achieve uniform excitation using static B_1 shimming has a limited number of degrees of freedom, making it increasingly difficult to control the transmit B_1 field over large FOVs to obtain a homogeneous B_1 field.

Dynamic shimming modulates the B_1 field by carefully controlling the transverse plane excitation pattern. The RF pulse required to rotate the magnetisation to achieve a uniform B_1 distribution is calculated using the Small Tip Angle (STA) approximation [33]. The STA approximation assumes the RF pulse (with a small flip angle α) only tips a small amount of the magnetisation away from equilibrium, such that the longitudinal magnetisation is assumed to have remain at equilibrium, $M_z \approx M_0$, and the transverse magnetisation M_{xy} scales linearly with α ($M_{xy} \propto \alpha$). RF pulses with larger flip angles result in non-linear behaviour of the transverse magnetisation which makes it difficult to control the magnetisation in pulse design algorithms.

RF pulses used to shim the B_1 field exploit the linearity in the STA approximation such that the excitation patterns from multiple transmit coils can be spatially superimposed to form an aggregate pattern to describe the evolution of the transverse excitation plane magnetisation $\mathbf{m} (\mathbf{r}, \omega)$, profile as,

$$\mathbf{m} (\mathbf{r}, \omega) = i\gamma \sum_{j=1}^{N_c} S_j (\mathbf{r}) \int_0^T b_j (t) \, e^{i\gamma(\Delta B_0(\mathbf{r})+\omega)(t-T)} e^{i\mathbf{r}\cdot\mathbf{k}(t)} dt, \qquad (2.4)$$

where $\mathbf{r} = (x, y, z)$ represents spatial locations, ω is the angular frequency and b_j represents the RF waveform (in units of the micro-Tesla μT). S_j are the dimensionless B_1 transmit coil profiles and therefore the instantaneous RF field is the product of $S_j(\mathbf{r}) \cdot b_j(t)$. N_c is the number of transmit channels and $\Delta B_0(\mathbf{r})$ accounts for inhomogeneity in the B_0 field. The RF pulses can be designed in either the spatial domain [34] or the Fourier domain [31] and are achieved by discretising Equ. 2.4 in time and space in matrix form,

$$\mathbf{m}(\mathbf{r}, \omega) = \mathbf{Ab}. \tag{2.5}$$

The system matrix $\mathbf{A}$ incorporates the measured B_1 transmit sensitivity profiles, B_0 inhomogeneity and the k-space trajectory during the excitation, $\mathbf{k}(t)$. The ith and jth elements of the system matrix are given by,

$$a_{ij} = i\gamma m_0 \Delta t e^{i\gamma \Delta B_0(\mathbf{r}_i)(t-T)} e^{i\mathbf{r}_i \cdot \mathbf{k}(t)}. \tag{2.6}$$

The vector $\mathbf{b}$ in Equ. 2.5 holds the complex RF waveforms for each of the N_c transmit channels and the solution to the linear problem can be solved using a magnitude least-squares algorithm:

$$\mathbf{b} = \min \left[\| |\mathbf{Ab}| - \mathbf{m} \|_{\mathbf{w}}^2 + \lambda \|\mathbf{b}\|^2 \right]. \tag{2.7}$$

The mathematical formulation to dynamically shim the B_1 field requires prior knowledge of the k-space trajectory during excitation and the target excitation pattern. The choice of the k-space trajectory depends upon the choice of B_1 shimming and is split into two forms: selective or non-selective excitations. Spiral [35] and SPINS [36] are examples of non-selective excitations and are used effectively in small FOV excitations. Slice selective excitations, primarily used in large FOV excitations, are based on spokes excitations and an application of them will now be described.

Excitation for a B_1 Homogeneous Field Simulation Results

Aim

To improve the B_1 transmit field for target regions: the whole head, in the cerebellum and a small ROI where the B_1 field is low, using a slice selective spoke excitation.

Methods

B_1 transmit field inhomogeneity can be overcome by breaking the slice selective RF pulse into a set of sub RF pulses and k-space modulations known as spokes (also termed fast k_z) trajectories. A single spoke is equivalent to a standard slice selective pulse, and additional spokes applied at offsets away from $k_x = k_y = 0$ provide in-plane spatial modulation to the transmit field. The number of spokes and the locations of the in-plane k-space modulations are a key consideration when optimising the excitation pulse sequence. For just one spoke pulse (at
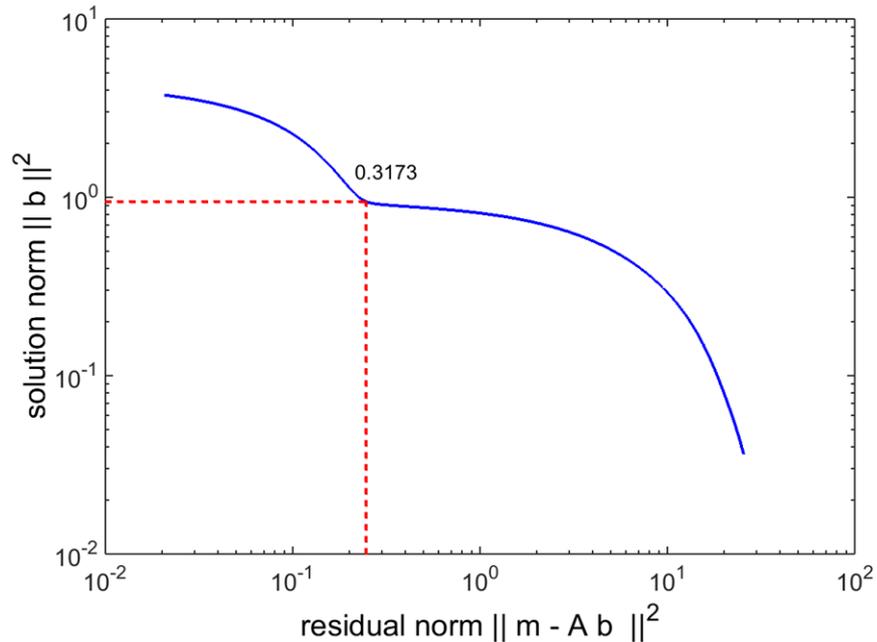
Figure 2.8: l_2 optimisation curve, locating the optimum value of λ used in the magnitude least squared solution (Equ.2.7) for the 5$^{\text{th}}$ spoke in the whole head target excitation spoke pulse design.

$k_x = k_y = 0$) the simulated transverse magnetisation profile $\mathbf{m}\left(\mathbf{r}, \omega_0\right)$ is shown in Figure 2.9. The additional spokes in-plane k-space modulations are chosen by searching for the largest RF norm to excite the residual error between the target excitation and the previous excitation profile using a greedy search approach.
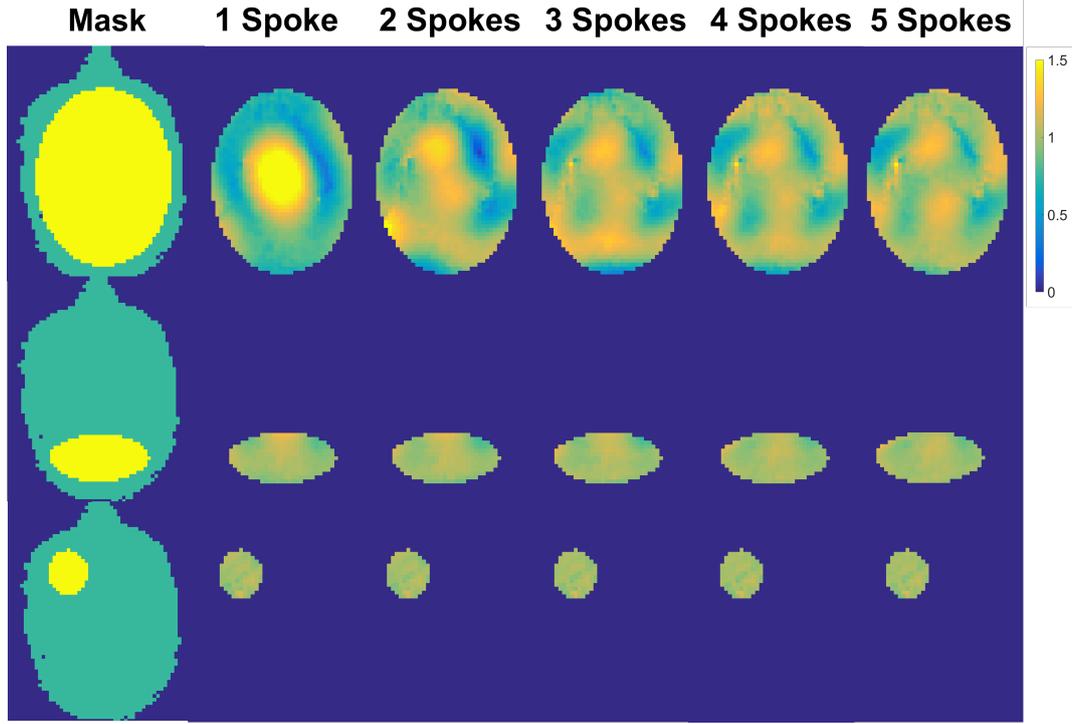
Figure 2.9: Simulated (normalised) B_1 transmit profiles for the N spokes for three target excitations: Whole head, cerebellum and a small ROI.

The spokes excitation sequences are re-optimised for each addition of a k-space modulation to control the amount of RF power deposited. The solution to Equ. 2.7 can include additional constraints to control the SAR and RF power. In this example the Tikhonov regularisation parameter λ is used to control the total RF power ($\|\mathbf{b}\|^2$) given by,

$$\|\mathbf{b}\|^2 = \frac{1}{N_c} \sum_{j=1}^{N_c} \int \|b_j\left(t\right)\|^2 dt. \tag{2.8}$$

It is also important to ensure the best solution to $|\mathbf{Ab}| - \mathbf{m}$, as increased λ detrimentally affects the solution. The optimal value of λ is found by examining

2.5. Improving B_1 Homogeneity

(a) Locations of Spokes

(b) In-plane slice profile
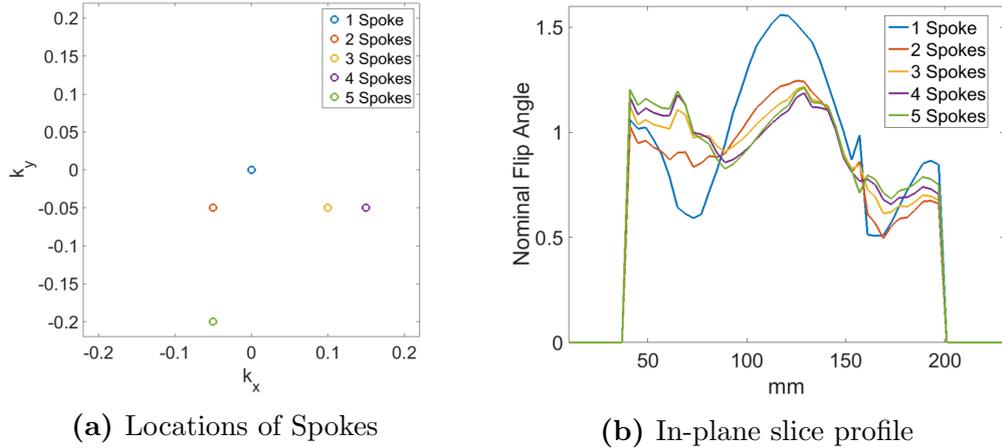
Figure 2.10: (a) The location of the spokes in k-space and (b) the through plane B_1 transmit profile for the N spokes for the whole head excitation pulse design.

the residual norm of Equ. 2.7 for a range of λ regularisations to produce the l_2 curve shown in Figure 2.8 for the 5$^{\text{th}}$ spoke in the whole head excitation. On the l_2 curve the turning point found at $\lambda = 0.3173$ is considered the optimal solution since increasing λ beyond this point has very little effect on reducing the RF power, whilst at the same time detrimentally affecting the solution to the B_1 transmit profile. This method of minimising the RF deposited power, however does not account for local SAR hotspots that can appear when the phase and amplitude of the RF pulses from the two independent channels are adjusted. More complex algorithms can be used to model the SAR, where the knowledge of electric fields is required but is not measurable by MRI.

Results

Excitation achieved with one to five optimised spokes are shown in Figure 2.9 for the three target extraditions. Figure 2.10(a) shows the k-space modulations for the whole head excitation and Figure 2.10(b) shows the B_1 through slice profiles for each of the spokes. The RF and gradient waveform for a five spokes, slice selective excitation are shown in Figure 2.11 for the whole head target excitation. As RF spokes are added to the slice selection, the B_1 field profile

smooths out for the three target excitations.

Table 2.1: The varation of the achieved flip angle (%) for the number of spoke modulations in k-space for the target excitations.

Flip Angle Variance	1 Spoke	2 Spokes	3 Spokes	4 Spokes	5 Spokes
Whole Head	30%	21%	17%	15%	14%
Cerebellum	7%	6%	6%	5%	4%
Small ROI	5%	4%	4%	4%	4%

The variation of expected flip angle for each additional simulated spokes is presented in Table 2.1 for the three target excitations, and shows that flip angle variance halves from a conventional (one spoke) excitation and five spokes for the whole head excitation but for the cerebellum and small ROI the variance between one spoke and five spokes falls by 2-3%. The total RF power for each additional spoke for all three target excitations are shown in Figure 2.12 with the small ROI requiring significantly more power than the whole head and cerebellum target excitations.

Discussion

Simulations of the spokes excitation show that for a large target excitation like the whole head, the variation in the flip angle is improved. For the cerebellum and small ROI target excitation there is not a significant improvement to the B_1 transmit field with increased spokes to suggest that they should be used to improve the B_1 field. The RF power for the small ROI target excitation is much greater than the other excitation as the B_1 transmit field is lower in this region prior to RF spokes design.

Although spokes have been proven to be successful at shimming to achieve a more homogeneous B_1 field they do result in increased duration of the slice selection. Shortening the spoke slice selection time would result in an increased SAR that cannot be achievable and a change in the excitation bandwidth.

The designed spokes sequence above is only based on the small-tip angle ap-

2.5. Improving B_1 Homogeneity
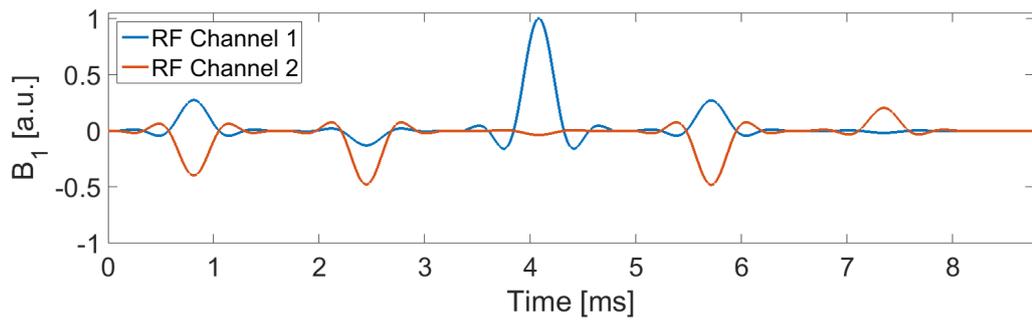
(a) RF waveforms
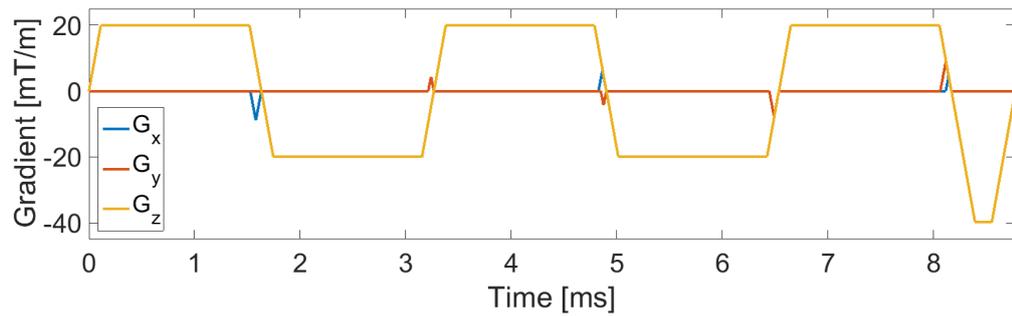
(b) Gradient waveforms

Figure 2.11: The (a) RF and (b) gradient waveforms for the two channel transmit coil for a five spoke excitation.
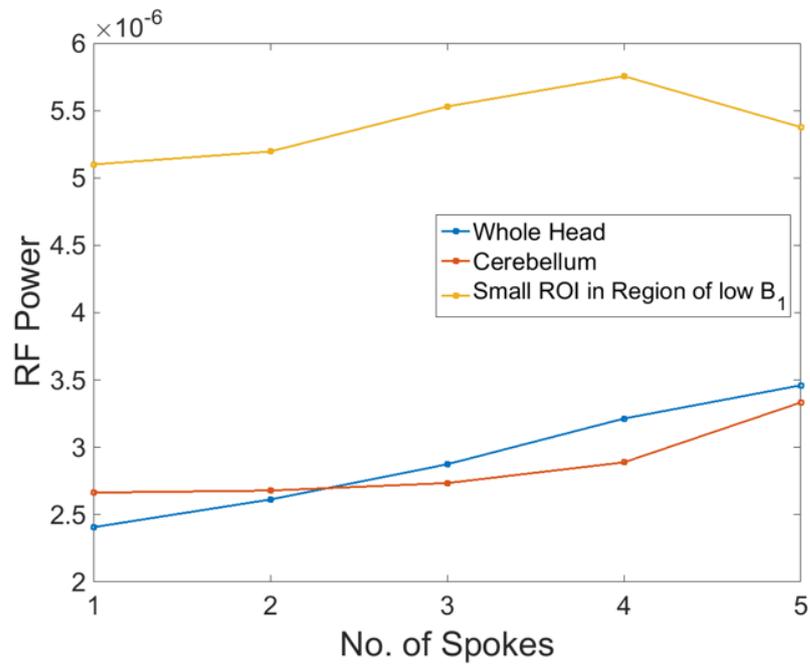
Figure 2.12: The RF power (Equ.2.8) for each spoke for the three target excitations.

proximation and for flip angles beyond 30° the B_1 profiles breakdown. Large tip angle methods are used for overcoming this problem and the additive angle approach is an example. The additive angle method [37] uses the STA approximation of the RF spokes waveform as its initial solution and the full Bloch equations are used to simulate the transverse magnetisation for the larger target flip angle. The resultant B_1 transmit profile is compared to the STA solution and the weights for each of the sub RF pulses are updated.

The spokes excitation results presented show that the detrimental B_1 field inhomogeneity at 7T could be overcome by using RF spoke excitations for large FOVs. The next step in the development of B_1 shimming here at Nottingham requires the spoke excitation sequence to be coded onto the scanner and careful consideration of the SAR before human imaging can be done.

2.6 Summary

This chapter has outlined the set up of an ultra high field MRI and the advantages and technical challenges for the development of MRI at this field strength. Also highlighted are the large spatial variations in the B_1 transmit field that detrimentally affect image quality. Dielectric pads were shown to increase the achieved B_1 field in cerebellum and temporal lobes where previously the signal was intrinsically low. Dynamic B_1 field shimming was also shown to improve the B_1 transmit profiles across the whole imaging slice, which dielectric pads were unable to achieve in simulations of slice selective spokes sequence.

Bibliography

[1] Blamire, A. The technology of MRI—the next 10 years? *The British journal of radiology* (2014).

[2] Vaughan, J. T. *et al.* Whole-body imaging at 7T: Preliminary results. *Magnetic resonance in Medicine* **61**, 244–248 (2009).

[3] Tochtrop, M., Vollmann, W., Holz, D. & Leussler, C. Automatic shimming of selected volumes in patients. In *Proc Soc Magn Reson Med*, vol. 6, 816 (1987).

[4] Holz, D., Jensen, D., Proksa, R., Tochtrop, M. & Vollmann, W. Automatic shimming for localized spectroscopy. *Medical physics* **15**, 898–903 (1988).

[5] Hartwig, V. *et al.* Biological effects and safety in magnetic resonance imaging: a review. *International journal of environmental research and public health* **6**, 1778–1798 (2009).

[6] Glover, P. M., Cavin, I., Qian, W., Bowtell, R. & Gowland, P. A. Magnetic-field-induced vertigo: A theoretical and experimental investigation. *Bioelectromagnetics* **28**, 349–361 (2007).

[7] Ham, C., Engels, J., Van de Wiel, G. & Machielsen, A. Peripheral nerve stimulation during MRI: effects of high gradient amplitudes and switching rates. *Journal of Magnetic Resonance Imaging* **7**, 933–937 (1997).

[8] Edelstein, W. A., Glover, G. H., Hardy, C. J. & Redington, R. W. The intrinsic signal-to-noise ratio in NMR imaging. *Magnetic Resonance in Medicine* **3**, 604–618 (1986).

[9] Vaughan, J. *et al.* 7T vs. 4T: RF power, homogeneity, and signal-to-noise comparison in head images. *Magnetic Resonance in Medicine* **46**, 24–30 (2001).

Bibliography

[10] Ugurbil, K. *et al.* Ultrahigh field magnetic resonance imaging and spectroscopy. *Magnetic resonance imaging* **21**, 1263–1281 (2003).

[11] Norris, D. G. High field human imaging. *Journal of magnetic resonance imaging* **18**, 519–529 (2003).

[12] Scheenen, T. W., Heerschap, A. & Klomp, D. W. Towards 1H-MRSI of the human brain at 7T with slice-selective adiabatic refocusing pulses. *Magnetic Resonance Materials in Physics, Biology and Medicine* **21**, 95–101 (2008).

[13] Brown, T., Kincaid, B. & Ugurbil, K. NMR chemical shift imaging in three dimensions. *Proceedings of the National Academy of Sciences* **79**, 3523–3526 (1982).

[14] Yao, B. *et al.* Susceptibility contrast in high field MRI of human brain as a function of tissue iron content. *Neuroimage* **44**, 1259–1266 (2009).

[15] de Rochefort, L., Brown, R., Prince, M. R. & Wang, Y. Quantitative MR susceptibility mapping using piece-wise constant regularized inversion of the magnetic field. *Magnetic Resonance in Medicine* **60**, 1003–1009 (2008).

[16] Li, W., Wu, B. & Liu, C. Quantitative susceptibility mapping of human brain reflects spatial variation in tissue composition. *Neuroimage* **55**, 1645–1656 (2011).

[17] Haacke, E., Tang, J., Neelavalli, J. & Cheng, Y. Susceptibility mapping as a means to visualize veins and quantify oxygen saturation. *Journal of Magnetic Resonance Imaging* **32**, 663–676 (2010).

[18] Beisteiner, R. *et al.* Clinical fMRI: evidence for a 7T benefit over 3T. *Neuroimage* **57**, 1015–1021 (2011).

[19] van der Zwaag, W. *et al.* fMRI at 1.5, 3 and 7 T: characterising BOLD signal changes. *Neuroimage* **47**, 1425–1434 (2009).

Bibliography

[20] Moser, E., Stahlberg, F., Ladd, M. E. & Trattnig, S. 7-T MR—from research to clinical applications? *NMR in biomedicine* **25**, 695–716 (2012).

[21] Bottomley, P. A. & Andrew, E. R. RF magnetic field penetration, phase shift and power dissipation in biological tissue: implications for NMR imaging. *Physics in Medicine and Biology* **23**, 630 (1978).

[22] Zelinski, A. C. *et al.* Specific absorption rate studies of the parallel transmission of inner-volume excitations at 7T. *Journal of magnetic resonance imaging* **28**, 1005–1018 (2008).

[23] Zaitsev, M., Dold, C., Sakas, G., Hennig, J. & Speck, O. Magnetic resonance imaging of freely moving objects: prospective real-time motion correction using an external optical motion tracking system. *Neuroimage* **31**, 1038–1050 (2006).

[24] Collins, C. M., Liu, W., Schreiber, W., Yang, Q. X. & Smith, M. B. Central brightening due to constructive interference with, without, and despite dielectric resonance. *Journal of magnetic resonance imaging : JMRI* **21**, 192–6 (2005).

[25] Yang, Q. X. *et al.* Analysis of wave behavior in lossy dielectric samples at high field. *Magnetic Resonance in Medicine* **47**, 982–989 (2002).

[26] Teeuwisse, W. M., Brink, W. M. & Webb, A. G. Quantitative assessment of the effects of high-permittivity pads in 7 Tesla MRI of the brain. *Magnetic resonance in medicine : official journal of the Society of Magnetic Resonance in Medicine / Society of Magnetic Resonance in Medicine* **67**, 1285–93 (2012).

[27] Yang, Q. X. *et al.* Reducing SAR and enhancing cerebral signal-to-noise ratio with high permittivity padding at 3 T. *Magnetic resonance in medicine* **65**, 358–362 (2011).

[28] Hoult, D. I. Sensitivity and power deposition in a high-field imaging experiment. *Journal of Magnetic Resonance Imaging* **12**, 46–67 (2000).

[29] Ibrahim, T. S., Lee, R., Baertlein, B. A., Kangarlu, A. & Robitaille, P.-M. L. Application of finite difference time domain method for the design of birdcage RF head coils using multi-port excitations. *Magnetic resonance imaging* **18**, 733–742 (2000).

[30] Katscher, U., Börnert, P., Leussler, C. & Van Den Brink, J. S. Transmit SENSE. *Magnetic resonance in medicine official journal of the Society of Magnetic Resonance in Medicine Society of Magnetic Resonance in Medicine* **49**, 144–50 (2003).

[31] Zhu, Y. Parallel excitation with an array of transmit coils. *Magnetic resonance in medicine : official journal of the Society of Magnetic Resonance in Medicine / Society of Magnetic Resonance in Medicine* **51**, 775–84 (2004).

[32] Pruessmann, K. P., Weiger, M., Scheidegger, M. B., Boesiger, P. *et al.* SENSE: sensitivity encoding for fast MRI. *Magnetic resonance in medicine* **42**, 952–962 (1999).

[33] Pauly, J., Nishimura, D. & Macovski, A. A k-space analysis of small-tip-angle excitation. *Journal of Magnetic Resonance 1969* **81**, 43–56 (1989).

[34] Grissom, W. *et al.* Spatial domain method for the design of RF pulses in multicoil parallel excitation. *Magnetic resonance in medicine : official journal of the Society of Magnetic Resonance in Medicine / Society of Magnetic Resonance in Medicine* **56**, 620–9 (2006).

[35] Katscher, U., Börnert, P., Leussler, C. & Van Den Brink, J. S. Transmit sense. *Magnetic Resonance in Medicine* **49**, 144–150 (2003).

[36] Malik, S. J., Keihaninejad, S., Hammers, A. & Hajnal, J. V. Tailored excitation in 3D with spiral nonselective (SPINS) RF pulses. *Magnetic resonance in medicine* **67**, 1303–1315 (2012).

[37] Grissom, W. A., Yip, C.-Y., Wright, S. M., Fessler, J. A. & Noll, D. C. Additive angle method for fast large-tip-angle RF pulse design in parallel excitation. *Magnetic resonance in medicine* **59**, 779–787 (2008).

Chapter 3

Magnetisation Transfer Suppression Using Dual-Frequency Saturation RF Pulses

3.1 Introduction

The following chapter outlines the principles of magnetisation transfer and chemical exchange saturation transfer. The physical mechanisms, and the model that describes the magnetisation transfer between different chemical environments, are presented along with methods to quantify the exchange processes. Finally a new method of suppressing the magnetisation transfer from the macromolecular bound pool is described, to improve visualisation of smaller exchange effects using dual-frequency modulated RF saturation pulses. This includes the RF pulse design along with simulations and phantom validation experiments to assess the MT suppression effectiveness and the *in vivo* application of the technique.

3.2 Sources of Magnetisation Transfer

3.2.1 Magnetisation Transfer from the Macromolecules

In hydration layers of large macromolecules, the water molecules are bound and therefore have a restricted rotational and translational motion seen in Figure 3.1. In free water the protons are freely moving with a faster average rotational frequency than bound water protons. Water protons can be viewed as small magnetic dipoles, and the rotational and translational motion of these dipoles disturbs the surrounding magnetic field. Over long time courses (of the order of nanoseconds) the field disturbances average to zero for the free water protons. In contrast the protons bound to macromolecules have a fixed orientation and therefore cannot exhibit the same rotational and translational motion. In close proximity to these protons the magnetic field disturbances do not average to zero, and consequently cause local variations in the magnetic field giving rise to additional T_2^* dephasing of the order of μs, and the (several kHz) wide frequency distribution which is modelled by a super-Lorentzian or Gaussian lineshape [1]. The net NMR signal from the bound proton disappears rapidly due to the very short T_2 and therefore it is not possible to detect it with standard NMR imaging. However, these protons can be indirectly imaged through the monitoring of magnetisation transfer from the macromolecular bound pool to the free water. The net transfer of magnetisation from macromolecules can occur over two pathways: direct transfer of magnetisation via spin transfer and dipole-dipole interactions or the transfer of protons in spin exchange.

3.2.2 Chemical Exchange Saturation Transfer

The principle of magnetisation exchange behind the contrast in Chemical Exchange Saturation Transfer (CEST) was first utilised in magnetisation transfer contrast (MTC) imaging [2]. There are a large variety of molecules exchanging
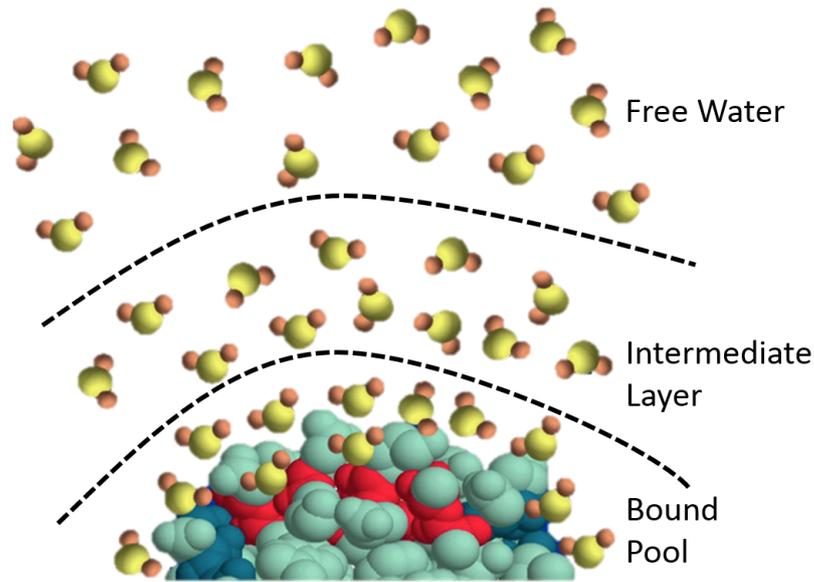
Figure 3.1: Diagram of hydration layers around a macromolecule.

magnetisation, beyond the macromolecular bound pool. Chemical exchange between solutes and the bulk free water spins can be detected over the broad MT spectrum. CEST contrast provides an increase of several orders of magnitude in sensitivity for metabolites over direct detection via MRS [3], through the indirect detection of exchange through the water signal. The exchange processes can be separated into three different forms: proton exchange, molecular exchange and compartmental exchange, which are shown in Figure 3.2. The chemical groups $-NH$, $-NH_2$ and $-OH$ are associated with proton exchange [4–7], and are commonly termed amide, amine and hydroxyl groups respectively. These chemicals can be exogenous as well as endogenous. Endogenous CEST contrast originates from within an organism, tissue or cell, and takes advantage of proton exchange in fast tumbling molecules of proteins and small peptides found in relatively high concentration *in vivo*. The T_2s of the exchanging protons are longer than those of protons attached to the macromolecules, allowing them to be distinguished by a narrow Lorentzian lineshape overlapping the broad MT spectrum. The chemical shift of the protons is between 0 to 5 ppm downfield from water and depends upon the molecules whose exchange rate can vary in the

range of a few Hz to 10,000 Hz. This range encompasses most $-NH$ exchanging groups which are the most developed CEST contrast technique to date, termed amide proton transfer (APT) [6]. The maximum APT contrast is detected at 3.5 ppm downfield from water and the exchange rate of the molecules involved in APT contrast is a function of temperature, pH and the buffer properties of the solution [8].

(a) Proton Exchange   **(b)** Molecular Exchange   **(c)** Compartment Exchange
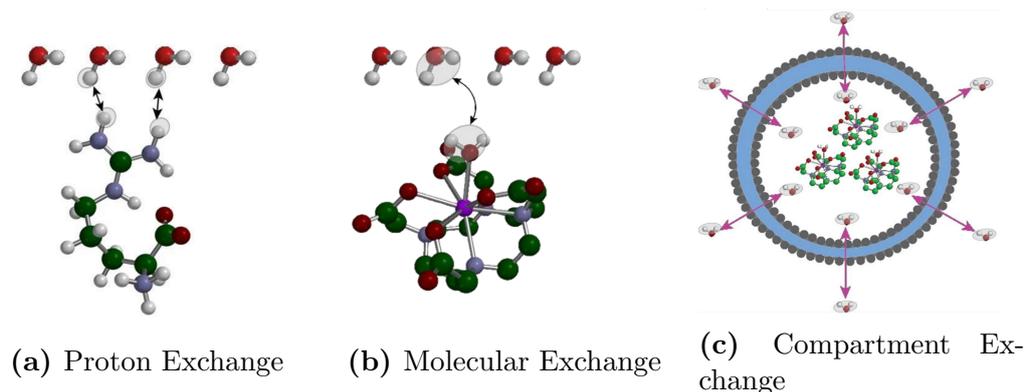
Figure 3.2: The three exchange pathways that can result in chemical exchange saturation transfer (CEST) contrast: (a) proton exchange, (b) molecular exchange and (c) compartment exchange. Adapted from [9].

3.2.3 Nuclear Overhauser Enhancement

Nuclear Overhasuer Enhancement (NOE) is another type of magnetisation transfer that occurs due to the direct interaction of magnetisation between protons in close proximity in different molecules. Beyond the physical transfer of protons through space, other molecules containing $-CH$ and $-CH_2$ groups 0 to -10 ppm upfield from water can directly exchange magnetisation. Homo-nuclear $H^1 - H^1$ NOE meditated magnetisation transfer between aliphatic protons (resonating between -2 and -5 ppm) and the bulk water can be detected *in vivo*. The transfer of magnetisation may occur via two pathways: intermolecular cross relaxation and exchange relayed transfer. Exchange relayed magnetisation transfer relies on labile amide hydroxyl hydrogens exchanging with hydrogen which are in close proxmity with the bulk free water, followed by intramolecular exchange between

neighbouring immobile protons in macromolecules [10]. Intermolecular cross relaxation occurs between trapped water molecules within protein structures and the bulk free water [11].

3.3 Principles of Chemical Exchange

CEST contrast originates from the effects observed in saturation transfer experiments in NMR spectroscopy [12] where RF saturation pulses of sufficient power are used to promote spins from the lower energy state (aligned with the B_0 field) to the higher energy state (aligned against the B_0 field) and results in a reduction of the bulk magnetisation. If enough RF saturation is applied, eventually the number of spins in the higher energy state will match the lower energy state and the net magnetisation is zero, and therefore the NMR signal is completely eliminated.
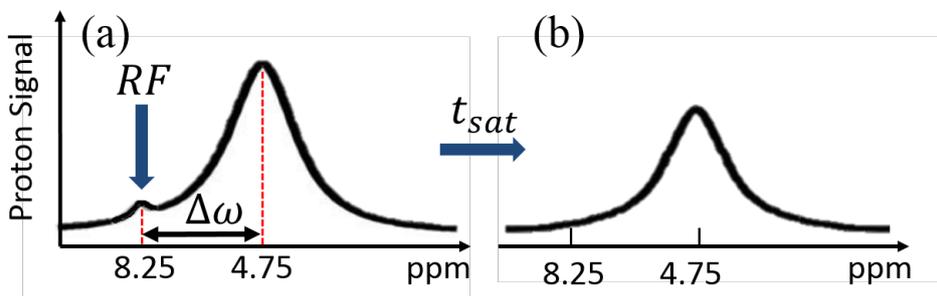
Figure 3.3: Solute protons are saturated at their specific resonance frequency in the proton spectrum (here 8.25 ppm for amide protons). This saturation is transferred to water (4.75 ppm) at exchange rate k. After a period t_{sat}, this effect becomes visible on the water signal (b).

To obtain a detectable CEST contrast, consider two magnetically distinct environments in exchange. The exchanging pools, pool A and pool B, are resonating at angular frequencies ω_a and ω_b respectively and separated by $\Delta\omega = |\omega_a - \omega_b|$, and in Figure 3.3(a) pool A representing the free water is seen in the proton signal at 4.75 ppm, and pool B for the amides at 8.25 ppm. To observe the chemical exchange processes from the NMR signal the exchange must be in the

slow exchange regime. RF saturation pulses applied on-resonance for pool B (at 8.25 ppm in the proton signal in Figure 3.3) result in an increased number of spins aligning against the B_0 field, and thus decreasing the bulk magnetisation. Immediately after the RF saturation, pool A (which was not saturated) remains at Boltzmann equilibrium, as the RF saturation pulses have not perturbed the magnetisation of pool A. However, over time the magnetisation of pool A will be perturbed as a result of chemical exchange between the pools, resulting in an increased number of spins in the higher energy state in pool A and a decrease of spins in the lower energy state. Overall the spin exchange results in the distribution of spins in pool A to move closer to the saturation level and therefore decrease in observed net magnetisation. Obtaining an NMR signal through the application of an excitation pulse immediately after the RF saturation reveals lower signal from pool B (due to its saturation) but also a loss of signal intensity from pool A, seen in Figure 3.3(b).

The chemical exchange processes that are observed in the NMR signal are in strong competition with longitudinal relaxation. If $R_1 = 1/T_1$ of pool B is faster than the exchange rate between pool B to pool A, the spin system will return to equilibrium before any spin exchange perturbs the magnetisation of pool A. CEST contrast can only be observed if the R_1s of both pools A and B are greater than the exchange rate, therefore a larger B_0 field is advantageous as it will result in a larger CEST contrast as T_1 relaxation time increases B_0.

The Z-Spectrum

Acquiring the NMR signal after saturation (S_{sat}) and the NMR signal with no RF saturation (S_0), a plot of the normalised M_z magnetisation of water signal intensity S_{sat}/S_0 as a function of off-resonance frequency is generated and is known as a z-spectrum, with 0 ppm the central water frequency. *In vivo* z-spectra from an ROI in healthy white matter acquired at 7T is shown in Figure 3.4 and show how S_{sat}/S_0 varies with off-resonances frequency for three nominal $B_{1,sat}$ saturation powers.
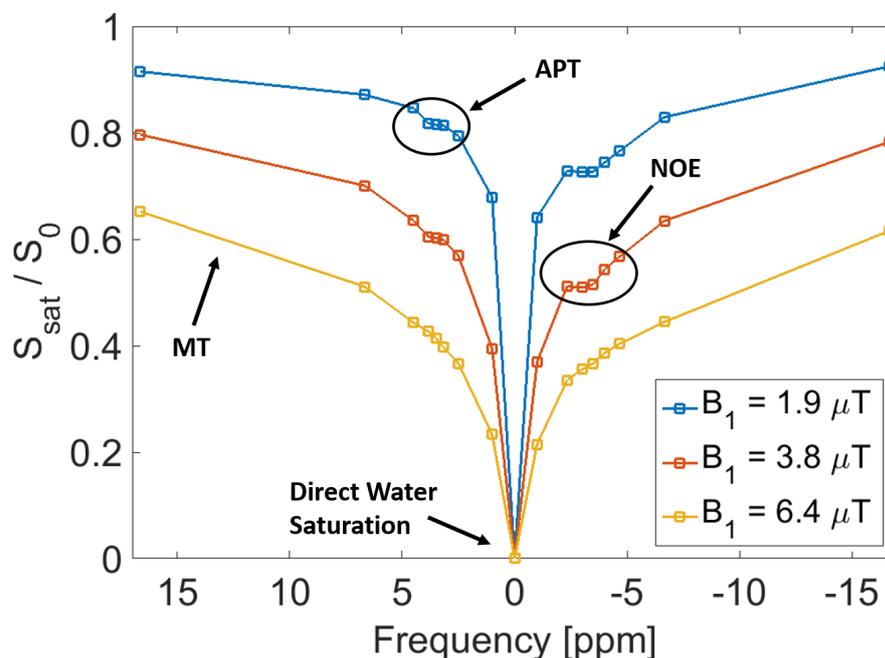
Figure 3.4: *In vivo* white matter z-spectra acquired at 7T for three nominal $B_{1,sat}$ powers of 1.9, 3.8 and 6.4 μT.

APT and NOE phenomena are illustrated in Figure 3.4 and occur at chemical shifts of 3.5 ppm and -3.5 ppm respectively away from the direct water saturation at 0 ppm. A major difference between MT and CEST contrast is the frequency specificity required to generate the CEST contrast whilst MT can be detected over several ppm.

The shape of the z-spectrum is dependent on the inherent characteristics of the exchange processes of the magnetisation between protons of macromolecules, proteins and lipids and free water. Notice in Figure 3.4 that with increasing B_1 saturation power, the APT and NOE peaks at ± 3.5 ppm respectively become less observable as MT from the macromolecules dominates over these effects. Analysis of the z-spectrum through quantification methods, described later in more detail (Section 3.7), can be used to extract CEST, NOE, and MT proton pool sizes.

3.4 Chemical Exchange Rates

If two molecules are exchanging magnetisation their NMR spectra will be modified. The slow, coalescence and fast exchange rates regimes are identified in Figure 3.5 along with the case of no exchange [13].
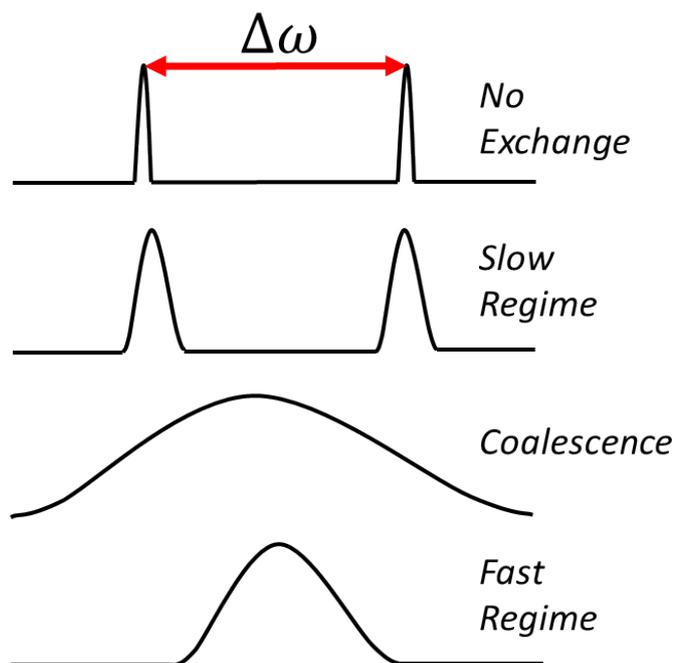
Figure 3.5: Schematic of the NMR spectrum for symmetrical two-site exchange and the dependence of the frequency of exchange in the slow regime, two distinctive peaks, occurs when $k_{ex} < |\frac{\Delta\omega}{2}|$. Coalescence, the merging of the two NMR peaks, $k_{ex} = |\frac{\Delta\omega}{2}|$ and the fast regime, one NMR peak detectable, $k_{ex} > |\frac{\Delta\omega}{2}|$.

Slow Exchange Regime

The separation between the two resonance frequencies $\Delta\omega$ is much greater than the exchange rate k_{ex}. The term 'slow exchange' refers to low probability of exchange between the molecular sites, and when exchange does occur the resolved NMR spectra has two distinct resonance lines. The saturation transfer method first described by Forsen [12] was used to examine the exchange rate k_{ex} in this regime.

Fast Exchanging Regime

k_{ex} is much larger than the separation resonance frequency $\Delta\omega$ and the observed lineshape merges into one sharp resonance line, primarily due to the motional narrowing effect [14].

Coalescence Regime

The exchange rate k_{ex} is half of the separation between the resonance lines $\Delta\omega$ and the observed resonant line broadens extensively, making the detection of the two peaks extremely difficult. Saturation transfer is not effective in measuring the exchange rate, and generally a spin-locking method is required. Spin locking [15] is used to measure the relaxation time $T_{1\rho}$ as a function of the locking field strength, and as a result the exchange rate can be determined.

3.5 Exchange Model
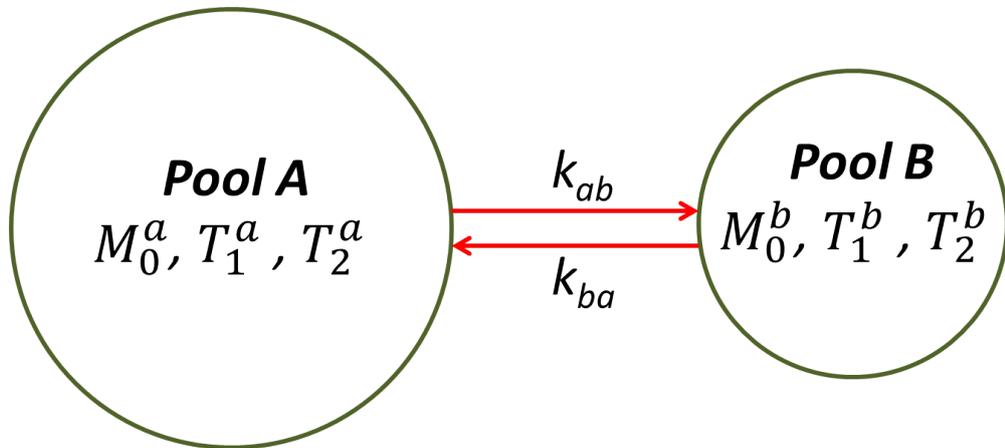
Figure 3.6: The two-pool model with exchange. $M_0^{a,b}$ are the relative concentration of protons in exchange pools, $T_2^{a,b}$ are the transverse relaxation times for both pools, $T_1^{a,b}$ the longitudinal relaxation rate, $k_{a,b}$ and $k_{b,a}$ the exchange rate constants governing exchange between the pools.

A two-pool model describes CEST or MT contrast in its simplest form. The model consists of a large pool A which represents the bulk free water and pool B a small solute, illustrated in Figure 3.6. Pools A and B are in different chemical

3.5. Exchange Model

environments and have differing thermal equilibrium magnetisation $M_0^{a,b}$ and longitudinal and transverse relaxation rates $T_1^{a,b}$ and $T_2^{a,b}$ respectively. The two-pool model assumes no scalar coupling between the pools which can each be described by the Bloch equations (Equ. 1.15) after having been modified to describe the chemical exchange. Termed the Bloch-McConnell equations, these coupled equations describe the dynamics of the magnetisation undergoing exchange in the presence of an RF saturation,

$$\frac{dM(t, \omega_{rf})}{dt} = \mathbf{A}(t, \omega_{rf}) \cdot \mathbf{M}(t, \omega_{rf}) + \mathbf{B} \cdot \mathbf{M_0}. \tag{3.1}$$

$\mathbf{M}(t, \omega_{rf})$ describes the magnetisation after the RF saturation pulse ω_{rf}, at time t and $\mathbf{M_0}$ is the initial longitudinal magnetisation such that,

$$\mathbf{M}(t, \omega_{rf}) = \begin{bmatrix} M_x^a(t, \omega_{rf}) \\ M_y^a(t, \omega_{rf}) \\ M_z^a(t, \omega_{rf}) \\ M_x^b(t, \omega_{rf}) \\ M_y^b(t, \omega_{rf}) \\ M_z^b(t, \omega_{rf}) \end{bmatrix}, \mathbf{M_0} = \begin{bmatrix} 0 \\ 0 \\ M_0^a \\ 0 \\ 0 \\ M_0^b \end{bmatrix}. \tag{3.2}$$

$\mathbf{A}(t, \omega_{rf})$, termed the mixing matrix, describes the evolution of the magnetisation of pools A and B undergoing exchange and RF saturation,

$$\mathbf{A}(t, \omega_{rf}) = \begin{bmatrix} -\frac{1}{T_2^a} - k_{ab} & -\Delta_a & 0 & k_{ba} & 0 & 0 \\ \Delta_a & -\frac{1}{T_2^a} - k_{ab} & -\omega_{rf} & 0 & k_{ba} & 0 \\ 0 & -\omega_{rf} & -\frac{1}{T_1^a} - k_{ab} & 0 & 0 & k_{ba} \\ k_{ab} & 0 & 0 & -\frac{1}{T_2^b} - k_{ba} & -\Delta_b & 0 \\ 0 & k_{ab} & 0 & \Delta_b & -\frac{1}{T_2^b} - k_{ba} & -\omega_{rf} \\ 0 & 0 & k_{ab} & 0 & -\omega_{rf} & -\frac{1}{T_1^b} - k_{ba} \\ & & & & & -R_b(\omega_{rf}) \end{bmatrix}, \tag{3.3}$$

3.5. Exchange Model

where k_{ab} and k_{ba} are the exchange rates between pool A and pool B and *vice versa*, and are related by,

$$M_0^a k_{ab} = M_0^b k_{ba}. \tag{3.4}$$

The net chemical exchange rate is characterised as $k_{ex} = k_{ab} + k_{ba}$ and $\Delta_{a,b} = \omega_{a,b} - \omega_{rf}$ represents the frequency shift between the RF saturation pulse and resonance frequency of pools A or B. The correlation time $\tau_{ab} = 1/k_{ab}$ defines the mean length of time a proton spends in pool A before transitioning to pool B.

$\mathbf{B}$ incorporates the longitudinal relaxation of the pools in the absence of any exchange processes,

$$\mathbf{B} = \begin{bmatrix} 0 & 0 & 0 & 0 & 0 & 0 \\ 0 & 0 & 0 & 0 & 0 & 0 \\ 0 & 0 & \dfrac{1}{T_1^a} & 0 & 0 & 0 \\ 0 & 0 & 0 & 0 & 0 & 0 \\ 0 & 0 & 0 & 0 & 0 & 0 \\ 0 & 0 & 0 & 0 & 0 & \dfrac{1}{T_1^b} \end{bmatrix}. \tag{3.5}$$

If pool B describes the macromolecular bound pool, an additional term in the mixing matrix $\mathbf{A}(t, \omega_{rf})$ is required, since the Bloch equations only apply to spins that are in rapid motion and are modelled by a Lorentzian lineshape. $R_b(\omega_{rf})$ is required to describe the super-Lorentzian lineshape of the macromolecular pool for the solution of the two-pool model to be physically accurate [1].

There are two distinct types of saturation transfer experiments: steady state and transient state. The steady state occurs when the spin system becomes time independent $(dM/dt = 0)$, and when pool B is also completely saturated,

such that $M_x^b = M_y^b = M_z^b = 0$, then Equ. 3.1 simplifies to a solution of the magnetisation of pool A,

$$\frac{M_z^a}{M_0^a} = \frac{\tau_{ab}}{T_1^a + \tau_{ab}}, \tag{3.6}$$

and can be re-arranged (using Equ. 3.4) in terms of the exchanging proton pool concentration and the lifetime of pool B,

$$\frac{M_z^a}{M_0^a} = \frac{\tau_{ba}}{T_1^a \frac{M_0^b}{M_0^a} + \tau_{ba}}. \tag{3.7}$$

In the transient state $(dM/dt \neq 0)$, the solution to Equ. 3.1 is more complicated. Assuming that pool B is still saturated and that there is no direct saturation of pool A, the transient state solution for M_z^a after the RF saturation of ω_{rf} is solved by integrating dM_z^a/dt,

$$\frac{M_z^a(t)}{M_0^a} = \frac{\tau_{ba}}{T_1^a + \tau_{ba}} + \frac{\tau_{ba}}{T_1^a + \tau_{ba}} \exp\left(-\frac{-T_1^a + \tau_{ba}}{T_1^a \tau_{ba}} t\right). \tag{3.8}$$

The model presented so far incorporates two exchanging proton pools, and in fact most simulations to analyse or optimise CEST contrast are based upon a three or four pool model incorporating free water and magnetisation transfer from macromolecules and CEST pools. To incorporate this, the mixing matrix $\mathbf{A}$ in Equ. 3.3 is expanded to include the extra pools such that it takes the form,

$$\mathbf{A}(t, \omega_{rf}) = \begin{bmatrix} \mathbf{D}_a & \mathbf{k}_{ab} & \mathbf{k}_{ac} & \cdots \\ \mathbf{k}_{ba} & \mathbf{D}_b & \mathbf{k}_{bc} & \cdots \\ \mathbf{k}_{ca} & \mathbf{k}_{cb} & \mathbf{D}_c & \cdots \\ \vdots & \vdots & \vdots & \ddots \end{bmatrix}, \tag{3.9}$$

where

$$\mathbf{D}_i = \begin{bmatrix} -\frac{1}{T_2^i} - k_i & -\Delta_i & 0 \\ \Delta_i & -\frac{1}{T_2^i} - k_i & -\omega_{rf} \\ 0 & -\omega_r f & -\frac{1}{T_1^i} - k_i \end{bmatrix} \tag{3.10}$$

and

$$\mathbf{k}_{ij} = k_{ij}\mathbf{I}_3. \tag{3.11}$$

The analytical solution to this form of the Bloch-McConnell equation can be found if the system is in the steady state [16, 17].

3.6 CEST at Ultra High Field

As discussed in Section 2.4, the move to ultra high field brings great advantages, but also technical challenges. Higher field strengths provide an increase in SNR and increased $\Delta\omega$ between exchanging sites. However, the lengthening of T_1 associated with higher B_0 results in a decrease in the amount of SNR per unit time in CEST experiments, and also the MT effect is greater at 7T due to the increased T_1 recovery. So the flip angles used in the imaging readout pulses tend to be small as larger flip angles in the readout result in complex interactions between the T_1 recovery and MT [18].

Focusing on the challenges in CEST contrast imaging, increased inhomogeneity in the static B_0 field results in larger variations from the desired off-resonance frequency saturation. The frequency variations are minimised by shimming the B_0 field within the imaging volume using the techniques outlined in Section 2.2.2 and in addition a B_0 field map can be used to correct the shifts in the water resonance frequency. Z-spectra are B_0 corrected on a voxel-by-voxel basis by interpolating the spectrum and shifting it by the difference between the B_0 map and the direct-water saturation at 0 ppm. Finally z-spectra are re-sampled

back to the original off-resonance frequencies. Water Saturation Shift Resonance (WASSR) is another method that can be employed to correct z-spectra. WASSR images the direct water saturation profile through the measurement of the absolute water frequency at low power, allowing centring of z-spectra on a voxel-by-voxel basis [19].

The effective saturation power depends on the inhomogeneity in the B_1 transmit field profile. The magnetisation transfer is dependent on the amount of saturation delivered, and therefore it is important to carefully map the B_1 field and take it into account in the quantification of CEST contrast. In Chapter 4 a B_1 correction method will be outlined.

3.7 Quantification of CEST and MT

The separation of the CEST effects from direct water saturation and MT from macromolecules has been a significant challenge in the development of CEST contrast imaging. The ultimate goal is to separate the different sources of CEST contrast observed in z-spectra and quantify the concentration of the exchanging pools and their respective exchange rates. There have been several methods developed to quantify CEST and MT.

3.7.1 Asymmetry Analysis

The simplest and crudest form of CEST contrast quantification is achieved via asymmetry analysis of z-spectra to obtain the proton transfer rate (PTR) [20, 21]. This technique is built on magnetisation transfer contrast quantification via magnetisation transfer ratio (MTR) parameter [22]. The analytical solution of the PTR is given as,

$$PTR = \frac{S_0 - S_{sat}\left(t_{sat}, \alpha\right)}{S_0},$$ (3.12)

where S_{sat} is a function of α that defines the RF saturation efficiently and in the steady saturation condition $\alpha = 1$. However, in reality it is not possible to measure the PTR directly *in vivo* as RF saturation pulses also affect the magnetisation in macromolecules and free water, reducing the acquired S_{sat}. The total ratio of S_{sat}/S_0 water signal after saturation at off-resonance frequency $\Delta\omega$ is a summation of the PTR, MTC and direct water saturation (DS),

$$\frac{S_{sat}\left(\Delta\omega\right)}{S_0} = PTR\left(\Delta\omega\right) + MTC\left(\Delta\omega\right) + DS\left(\Delta\omega\right). \qquad (3.13)$$

Assuming that direct water saturation and MT are approximately symmetrical about the central water resonance frequency at 0 ppm, the magnetisation transfer ratio asymmetry (MTR_{asym}) can be defined as,

$$MTR_{asym} = MTR\left(\Delta\omega\right) - MTR\left(-\Delta\omega\right) = \frac{S_{sat}\left(\Delta\omega\right)}{S_0} - \frac{S_{sat}\left(-\Delta\omega\right)}{S_0}, \quad (3.14)$$

and this has been used to separate the CEST effects from MT and direct saturation. However, this analysis very crudely assumes that MT is symmetrical about the central water frequency which is not valid, particularly *in vivo* at 7T, as seen in Figure 3.7. MT is symmetrical however, is shifted upfield to -2.4 ppm from water [23]. Also seen in Figure 3.7, with increasing RF saturation power the CEST contrast is masked by the dominating MT and becomes unquantifiable by MTR_{asym}.

Another source of error in MTR_{asym} arises from the fact that APT and NOE effects occur symmetrically around the water resonance at $\pm$ 3.5 ppm causing overlap in the MTR_{asym} and contaminating the quantification of both exchanging pools. Although asymmetrical analysis is a problematic technique for quantifying PTR, it can be a useful metric to assess the change in CEST contrast in a quick and simple way, and the initial adoption of the CEST contrast imaging

technique was driven by asymmetry analysis.
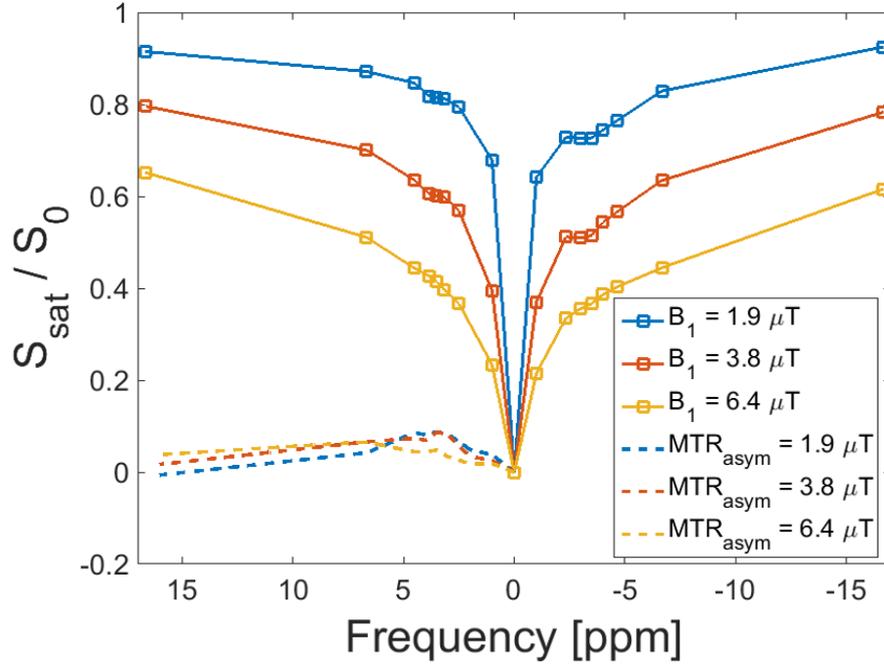
Figure 3.7: Asymmetry analysis of the *in vivo* white matter z-spectra acquired at 7T seen in Figure 3.4.

3.7.2 Lorentzian Lineshape Fitting Model

A more robust method of quantifying CEST contrast uses a model that sums Lorentzian lineshapes corresponding to each exchanging proton pool. The modified Bloch-McConnell equations [16] model the direct water saturation and other CEST pools as Lorentzian lineshapes, since they have long T_2s. The z-spectra in Figure 3.4 can be decomposed into separate Lorentzian lineshapes for each pool with independent amplitudes A_i, full width at half maximum W_i and central resonance frequencies $\omega_{ref,i}$ for the bulk water, NOE, CEST and MT. The multi Lorentzian model of the z-spectra can be described as,

$$\frac{S_{sat}(\Delta\omega)}{S_0} = 1 - \sum_{i=1}^{N} A_i \left[1 + \left(\frac{\Delta\omega - \omega_{ref,i}}{0.5W_i}\right)^2\right]^{-1}. \tag{3.15}$$

This model can also incoporate the MT lineshape that is modelled better by a super-Lorentzian [1] rather than a Lorentzian.

Figure 3.8 shows how the Lorentzian lineshape fitting model is implemented. A least-squares fitting algorithm is typically used to find the best linear summation of the lineshapes describing the exchanging proton pools. However, Figure 3.8(b) shows an example where MT dominates in the z-spectrum over all the other exchanging pools and makes it increasingly more difficult to fit.

To demonstrate the detrimental effect that MT from macromolecules has on the quantification of CEST contrast when the Lorentzian lineshape model fitting is used, a multi-Lorentzian fit for water, MT, APT and NOE was conducted on a simulated 4-pool Bloch-McConnell *in vivo* z-spectra database (used in *Geades et al* as a look-up-table [24]). The database contains z-spectra for MT, NOE and APT concentration between 1 to 15% for $B_{1,sat} = 6.4\mu$T.

The percentage error between the simulated *in vivo* z-spectrum and the Lorentzian model fitted z-spectrum for a range of MT concentrations and B_1 saturation powers are shown in Figure 3.9 and illustrate that for increased MT concentrations and $B_{1,sat}$ powers, the worse the fit becomes. The reality is that the Lorentzian model assumes that the system is linear and that there is no exchange of magnetisation during the build-up of saturation which at higher power is evidently untrue.

3.7.3 Bloch-McConnell Fitting

Numerical modelling of the evolution of the longitudinal magnetisation for the multi-exchanging proton pools is considered the 'gold standard' method of quantification. The observed exchange processes in the z-spectra can be modelled by the Bloch-McConnell equations (Equ. 3.1) which can include the concentration and exchange rates of the each pool. The disadvantage of the Bloch-McConnell fitting approach is the large number of parameters used within the model, such
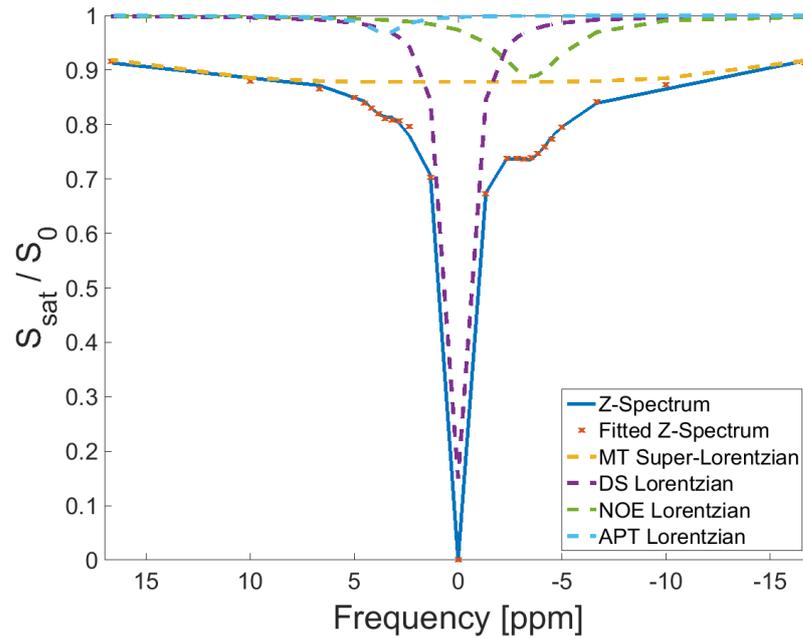
(a) $B_{1,sat} = 1.9 \ \mu T$
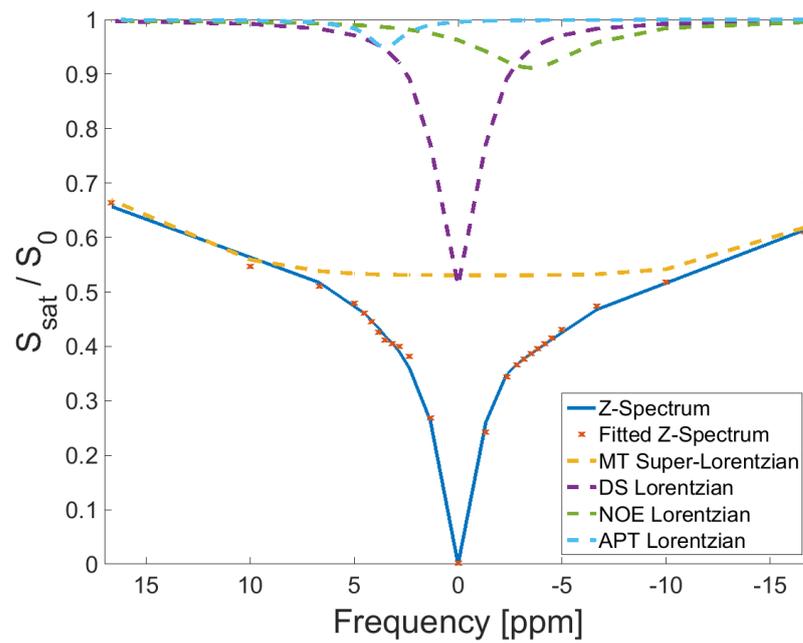
(b) $B_{1,sat} = 6.4 \ \mu T$

Figure 3.8: Lorentzian lineshape fitting applied to the *in vivo* z-spectra ($B_{1,sat}$ powers (a) 1.9 μT and (b) 6.4 μT from Figure 3.4. Lorentzian lineshapes for the DS, NOE and APT and super-Lorentzian for the MT. Red crosses show the sum of the Lorentzians fitted.
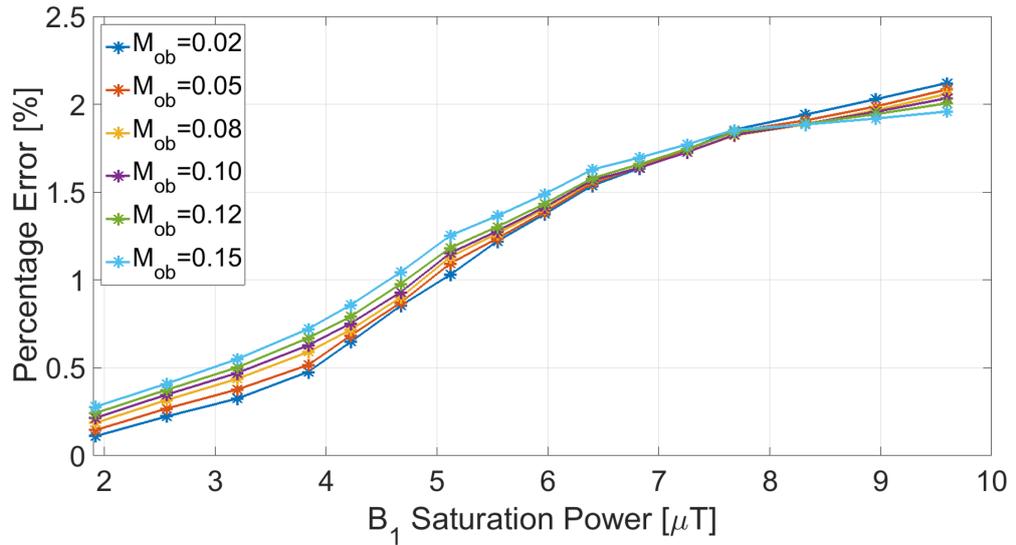
Figure 3.9: The percentage error between the simulated *in vivo* z-spectra and the Lorentzian model fitted spectra for a range of B_1 saturation powers and MT concentrations.

as the T_1 and T_2 of the exchanging pools, needed *a priori*. Although fairly well known, the inter-subject and intra-subject variability in these parameters potentially creates inaccuracies in the fitting. Despite this, the model does include the accurate super-Lorentzian lineshape model for the MT [25] that creates inaccuracy in the other described fitting methods. The Bloch-McConnell model can also directly incorporate the B_1 inhomogeneity in the saturation into the fitting and the observed T_1 that also determines the shape of the z-spectra. This method of fitting comes with heavy computational costs, particularly if the saturation does not reach a steady state, where there is no analytical solution to the Bloch-McConnell equations (Equ. 3.1) which have to be numerically solved.

The reduction of computational cost has been proposed recently by *Geades et al*, where a look-up-table (LUT) database of *in vivo* z-spectra was simulated for a range of proton pool concentrations, T_1 values of the bulk free water pool and B_1 saturations powers, assuming known values of T_1, T_2 and exchange rates of the exchanging proton pools [24]. The model also included B_1 inhomogeneity that detrimentally affects the acquired spectra at ultra high field. The proton pool

concentrations were estimated by comparing the experimentally measured *in vivo* z-spectra to every z-spectrum in the LUT by brute force least-squares fitting [24]. This method speeds up the quantification process as the acquired z-spectra are compared to known solutions, whereas direct Bloch-McConnell model fitting simulates a z-spectrum for each iteration of the fitted parameters.

3.7.4 Pulse Sequences for CEST Separation

Separation of CEST contrast from the broad MT spectrum has also been achieved through the careful design of pulse sequences.

The Z-spectroscopy with Alternating Phase Irradiation (ZAPI) [26] technique uses RF saturation pulses that are amplitude and/or phase modulated to exploit the different variations in the loss of coherence due to T_2 relaxation between MT, CEST and bulk free water. These pulses allow the selective saturation of the short T_2 components, and the signal attenuation due to direct water saturation and other longer T_2 components is shifted away from 0 ppm on the z-spectrum. Thus, the shorter T_2 components that are resonating close to 0 ppm can be highlighted.

As already discussed, conventional MTR_{asym} analysis is flawed due to the asymmetrical nature of magnetisation transfer. Another form of MTR_{asym} has been proposed that uses Saturation with Frequency Alternating RF Irradiation (SAFARI) [27]. SAFARI exploits the non-linearity of the saturation processes observed in the z-spectrum. Once the amide protons responsible for the detected APT peak at 3.5 ppm are fully saturated, any further increase in RF saturation will be independent of the observed APT contrast. The additional RF power will, however, still increase the MT and direct water saturation contribution to the z-spectrum. SAFARI acquisition and post-processing exploits this variation of saturation dependence with only three image acquisitions required. Figure 3.10 shows the schematic of the SAFARI imaging acquisition.

3.7. Quantification of CEST and MT

Two standard CEST images are acquired at the control (-3.5 ppm) and label (3.5 ppm) frequencies separately, with the same total RF power as the modulated pulse. The control attenuates the MT and direct water saturation, whilst the label also attenuates the CEST. The MT asymmetry means that the standard two-offset CEST difference $MTR_{asym} = [S_{sat}(\omega_-)\text{-}S_{sat}(\omega_+)]/S_0$ is not equal to the total CEST effect. RF saturation pulses that are modulated to saturate, with equal power, at both the control and label off-resonance frequencies simultaneously, will attenuate the MT and direct saturation at both off-resonance frequency and the CEST at 3.5 ppm. Using the three images, $MTR_{SAFARI} = [S_{sat}(\omega_-)+S_{sat}(\omega_+) - 2S_{sat}(SAFARI)]/S_0$, is calculated and isolates the CEST effect without contamination from the asymmetric MT.
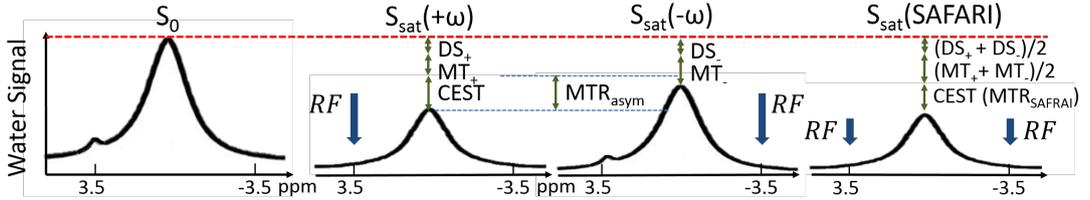
Figure 3.10: Schematic an SAFARI experiment, where the spectral line represents the free water signal. DS, MT, and CEST are the signal loss due to direct water saturation, magnetisation transfer and amide proton transfer, respectively. RF saturation is applied separately and simultaneously at the label and control frequencies ± 3.5 ppm. MTR_{SAFARI} is calculated as $[S_{sat}(\omega_-)+S_{sat}(\omega_+) - 2S_{sat}(SAFARI)]/S_0$, using the three water signal images.

Chemical Exchange Rotational Transfer (CERT) isolates the CEST effects from MT by exploiting the rotation exchange effect that slow exchanging species possess [28]. At 3.5 ppm off-resonance from water, after two saturation at different B_1 flip angles but the same average RF power, the MT in both signals is attenuated to the same level. However, the rotational contribution from the CEST effects is obtained after subtraction of two signals acquired with two different nutation flip angles.

Another method of isolating CEST from MT has been achieved by varying the 'mixing time' (the inter-pulse delay) in the pulsed saturation trains [29]. CEST effects from slow exchanging protons increase initially as a function of the mixing

time, because these spins require a longer time to exchange with water. After reaching a maximum, the CEST signal will then decay as a function of mixing time due to the T_1 relaxation of water. Acquiring the signal at two different mixing times, one where the CEST signal is at a maximum and the other when the CEST signal is nulled, but in both cases where the MT remains at a constant level, the subtraction of the two signals will isolate the CEST effects.

3.8   Imaging Methods

CEST contrast imaging sequences where the magnetisation is in a steady state require long RF saturations, $\sim$2-3 seconds long, to fully saturate the exchangeable proton pool being probed [30]. Careful considerations are required in designing CEST contrast acquisition sequences. Whilst total saturation of the exchanging pools is required, the amount of RF power delivered *in vivo* also needs to be kept as low as possible and within SAR limitations. The trade-off between the number of off-resonance frequencies acquired and the spatial resolution also needs consideration. The design of CEST acquisition sequences can be split into two parts: saturation and imaging readout.

Saturation

Originally long continuous wave (CW) rectangular pulses were widely used for saturation. CW pulses were advantageous as they provided narrow bandwidth and rapid saturation of the exchanging pool [31]. Also the analytical solution to the Bloch-McConnell equations is easily computed. This allows straightforward optimisation to achieve maximum CEST contrast. Since the bandwidth of saturation is proportional to $1/t_{sat}$, it was beneficial that the saturation was applied for a significant length of time.

However, CW saturation at ultra high field is problematic as more RF saturation power is required to reach the same level of saturation achieved at lower

(a) Continuous Wave (CW) CEST acquisition

(b) Pulsed-CEST acquisition

(c) Pulsed-CEST acquisition with segmented readout
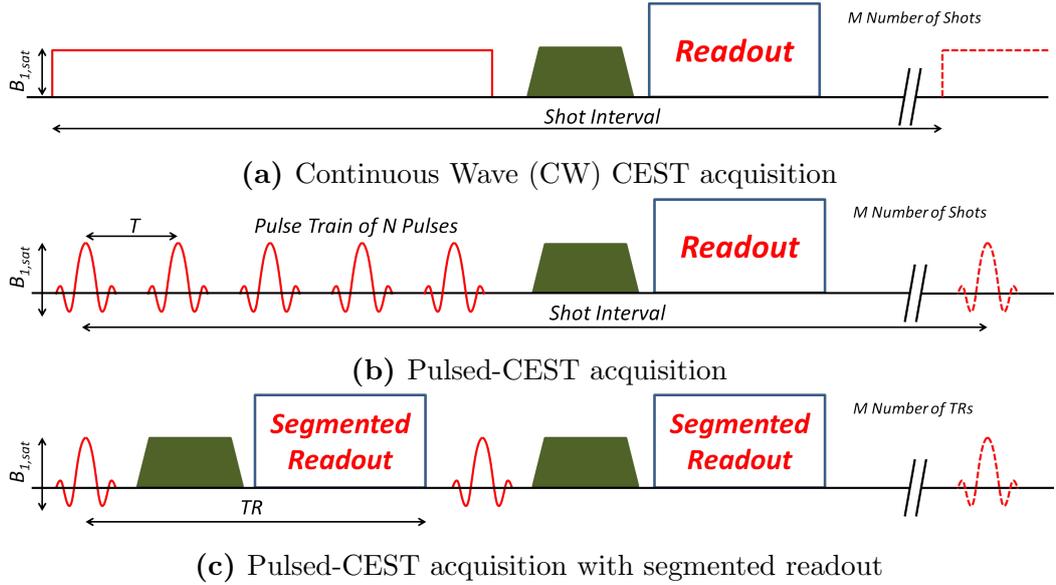
Figure 3.11: Types of saturation and imaging readouts used in CEST contrast acquisition.

field strengths. The RF amplifiers have limited duty cycles, restricting the use of CW pulses. The technical difficulties with CW saturation lead to saturation generally being achieved through the use of RF pulse trains, commonly termed pulsed-CEST [8]. Pulsed saturation consists of a train of N RF pulses before the readout (Figure 3.11(b)) or RF pulses interspersed with a segmented readout (Figure 3.11(c)). Pulsed saturation is characterised by a larger set of saturation parameters: number of pulses, pulse bandwidth, duty cycle, saturation power and the pulse shape. The choice of RF pulse shape used in the pulse train has been well tested. Gaussian or Gaussian modulated sinc pulses [32] are conventionally used in pulsed-CEST as they can generally achieve narrow bandwidth of $\sim$200 Hz with little to no sidebands. Pulsed saturation makes the analytical solution to the Bloch-McConnell equations more challenging. However, through optimisation of the saturation, there is more flexibility in probing exchange via adjusting the duty cycle and inter-pulse delay [29, 33].

Imaging Readout

During the early development of CEST contrast, the imaging readout was single-slice. However, single slice imaging has limited clinical value [6], and to overcome this challenge, multi-slice CEST acquisition schemes were developed [34, 35] but were hampered by inter-slice variation in off-resonance saturations.

Volumetric CEST acquisitions are not affected by unintended off-resonance saturation and 3D CEST acquisition schemes are now widely used. Volumetric CEST sequences can be separated into either steady-state segmented readouts or transient state (also termed pseudo-steady state) readouts as shown in Figure 3.11(c) and 3.11(b) respectively.

The transient state CEST sequence shown in Figure 3.11(b) is used throughout the work presented in this thesis. The sequence consists of a train of N RF saturation pulses at a given off-resonance frequency followed by a crusher gradient to remove the residual transverse magnetisation. A 3D Turbo Field Echo (TFE) readout, as described in Section 1.4.3, comprising of a chain of rapidly acquired single gradient echoes, was used to sample k-space from the centre outwards radially as the TFE signal fades off fast with T_1. M number of shots (normally 3-5) are required to achieve sensible SNR and spatial resolution.

For comparison a steady-state CEST sequence is shown in Figure 3.11(c) which comprises of a single off-resonance RF saturation pulse and gradient crusher followed by a 3D segmented EPI readout due to its fast acquisition of k-space. The steady state CEST signal is built up over M number of TRs and the k-space is sampled from the outer edges to centre, so that when the centre of k-space is sampled the magnetisation is in the steady state condition. A comparison of the two pulsed saturation sequences has revealed that the transient state saturation sequence is more sensitive to slow chemical exchange processes than the steady state sequence [30].

3.9 Dual-Frequency Magnetisation Transfer Suppression

3.9.1 Introduction

A major problem in CEST contrast imaging is the contamination by MT from the macromolecular bound pool, which hampers the detection of the narrow CEST peaks in z-spectra that resonate close to 0 ppm. Current methods to remove MT from z-spectra to better visualise and quantify NOE and CEST effects, include subtraction of a fitted super-Lorentzian used to model MT from the z-spectrum [36] and SAFARI pulse sequences. However, removing the MT spectrum in this way does not reveal CEST and NOE features that have been masked by MT saturation. This chapter investigates the use of dual-frequency band saturation pulses that are designed to saturate the MT to the same level throughout the acquisition and therefore suppress the MT contribution to the z-spectrum and reveal NOE and CEST effects more clearly, allowing better quantification.

Fundamentally quantification via a Lorentzian lineshape model fitting assumes that all the exchanging proton pools can be modelled using either Lorentzian, super-Lorentzian or Gaussian lineshapes. The lineshape model for MT has come under scrutiny recently. Super-Lorentizan lineshapes have been successfully used to model MT in many biological tissues [1, 37] under the assumption that the MT spectrum is isotropic. However, a correlation has been observed between the transverse relaxation rate of the macromolecular bound pool and the orientation of white matter fibres [38, 39]. This phenomenon has been reported to relate to the orientation dependence of the RF absorption lineshape, and *Pampel et al.* have shown that the MT lineshape can transition between a super-Lorentzian to a Gaussian as nerve fibres rotate through 90° in regions of high myelination [40]. Therefore an approach that reduces the sensitivity to the MT lineshape

would be more beneficial in CEST contrast imaging.

A new technique is now presented where the CEST and MT are simultaneously saturated, allowing the CEST contrast in z-spectra to be separated from the MT. This is achieved by using RF saturation pulses which simultaneously saturate at two off-resonance frequencies. The pulses are implemented to cycle one of the saturation bands over frequency offsets to interrogate the z-spectrum, as usual. The other saturation frequency band is fixed at a far off-resonance frequency (~ 6 kHz) which will suppress the macromolecular bound pool MT contribution across the whole z-spectrum, so that the MT is saturated to the same level during each acquisition. The design, simulations and *in vivo* implementation of the dual-frequency saturations pulses will now be described.

3.9.2 RF Pulse Design

The choice of RF saturation pulse shape is important in achieving the best possible separation of NOE and CEST effects. The pulse shapes govern the off-resonance frequency selectivity (associated with BW of the pulse) in multi off-resonance pulsed-CEST experiments. Saturation pulses need to have a narrow frequency response (~ 200Hz) to avoid direct water saturation effects around 0 ppm whilst the CEST and NOE effects are probed.

In pulsed-CEST experiments, the pulse shapes currently used are: Gaussian [32], Gaussian-windowed Sinc [6, 41] or Fermi [34] due to their narrow bandwidth of 200 Hz or less and minimal sidebands outside the frequency selective saturation band. Figure 3.12(a) shows a Gaussian windowed sinc pulse used in the saturation pulse train in the experiments to follow which is mathematically described as,

3.9. Dual-Frequency Magnetisation Transfer Suppression

$$B_{1,GS}(t) = \begin{cases} At_0 \dfrac{\sin\left(\dfrac{\pi t}{t_0}\right)}{\pi t} e^{-\frac{t^2}{2\sigma^2}}, & -N_L t_0 \leq t \leq N_R t_0 \\ 0, & \text{elsewhere.} \end{cases} \qquad (3.16)$$

The parameter A defines the peak amplitude of the pulse (in micro-Tesla) that occurs at $t = T/2$, for the symmetric sinc pulse, where T is the duration of the pulse, N_L and N_R are the number of zero crossing points left and right of the central peak at $t = T/2$, and t_0 is the half time-width of the central lobe. The Gaussian windowing of the sinc pulse is applied through the exponential term and the pulses used in the saturation train described in this and the following Chapter have $\sigma = 1$ and $N_L = N_R = 3$ illustrated in Figure 3.12(a) to achieve a bandwidth of 200 Hz and minimal sidebands outside the excitation.

The effect that the Gaussian windowed sinc has on the off-resonance longitudinal magnetisation is an important optimisation parameter in CEST contrast acqui-

(a) Gaussian windowed Sinc

(b) Longitudinal Magnetisation M_z
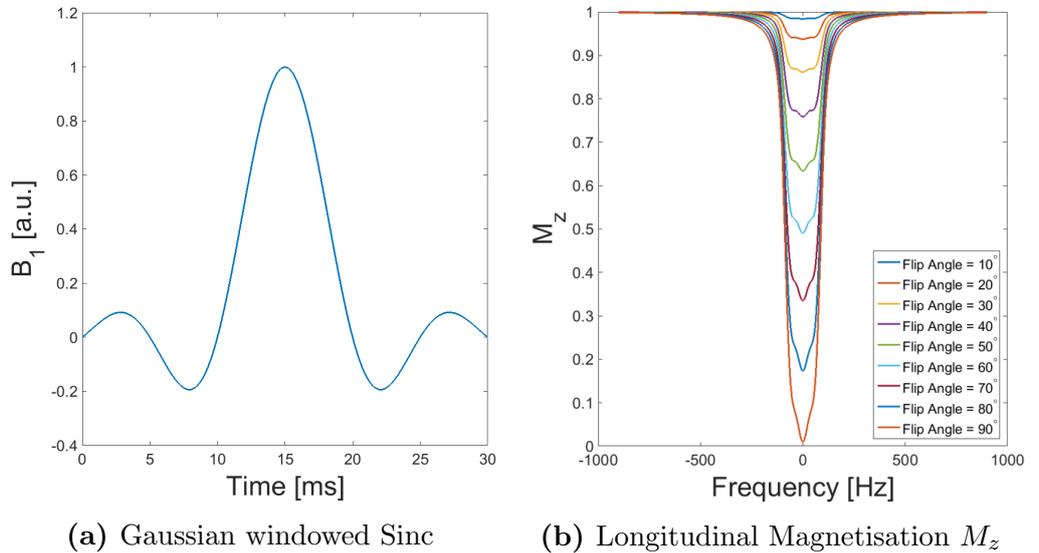
Figure 3.12: The (a) Gaussian windowed sinc (with normalised amplitude) and (b) the longitudinal magnetisation frequency profile for flip angles between 10° and 90° showing that the bandwidth of the magnetisation broadens for larger flip angles. As a result, Lorentzians with wider full width half maximums (FWHM) are fitted for the direct saturation in Lorentzian lineshape model fitting for higher B_1 powers.

3.9. Dual-Frequency Magnetisation Transfer Suppression

(a) $\alpha{:}\beta = 1{:}1$ **(b)** $\alpha{:}\beta = 1{:}2$ **(c)** $\alpha{:}\beta = 1{:}3$
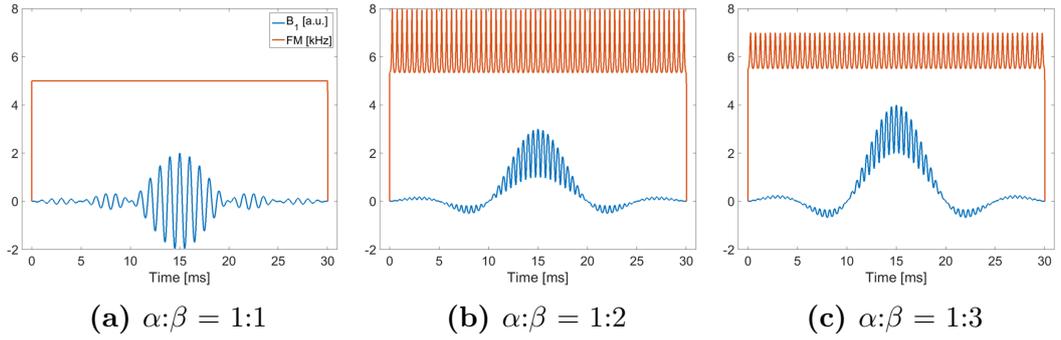
Figure 3.13: The amplitude (blue) and frequency (red) modulations of the designed dual-frequency band saturation RF pulses.

sition. The Gaussian windowed sinc with duration T = 30 ms has a bandwidth of 200 Hz in the absence of T_1 and T_2 relaxation processes and assuming the small tip angle approximation [42]. However, this is not a physical representation of the actual achieved frequency response of the longitudinal magnetisation. Figure 3.12(b) depicts the frequency selectivity (of the free water pool) predicted by the Bloch equations for the Gaussian windowed sinc with flip angles between 10° and 90° and shows how the bandwidth of the excitation broadens for larger flip angles. At higher B_1 saturations the bandwidth exceeds 200 Hz and requires a Lorentzian with a larger full-width half maximum to be fitted for the direct water saturation around 0 ppm, and this effect in the z-spectrum is shown in Figure 3.8(b).

The Gaussian windowed sinc pulses, $B_{1,GS}$, are frequency modulated to the desired off-resonance central carrier frequency by applying a modulation function,

$$B_{1,FM}\left(t\right) = B_{1,GS}\left(t\right) \cdot \exp\left(-2\pi i f_0 t\right). \tag{3.17}$$

RF saturation pulses that simultaneously saturate two off-resonance frequencies are designed by summing two Gaussian window sinc pulses which are frequency modulated at separate carrier frequencies f_0 and f_1,

$$B_{1,Dual\text{-}FM}\left(t\right) = B_{1,GS}\left(t\right) \cdot \left(\alpha \exp\left(-2\pi i f_1 t\right) + \beta \exp\left(-2\pi i f_0 t\right)\right), \tag{3.18}$$

assuming a linear response. Parameters α and β in Equ. 3.18 control the distribution of saturation power between the two desired off-resonance saturation frequencies and allow more of the B_1 power to be used to saturate the macromolecular bound pool. As β increases so does the total B_1 power, and the maximum value of β is limited by SAR constraints and maximum B_1 amplitude of the transmit coil. Figure 3.13 illustrates how the RF amplitude and frequency modulation waveforms vary for α and β ratios of (a) 1:1, (b) 1:2 and (c) 1:3. The response to the resultant pulses were Bloch simulated for a single water pool with the results shown in Figure 3.14 to validate that they excited the desired off-resonance frequencies and to ensure that there were no sidebands at other off-resonance frequencies.
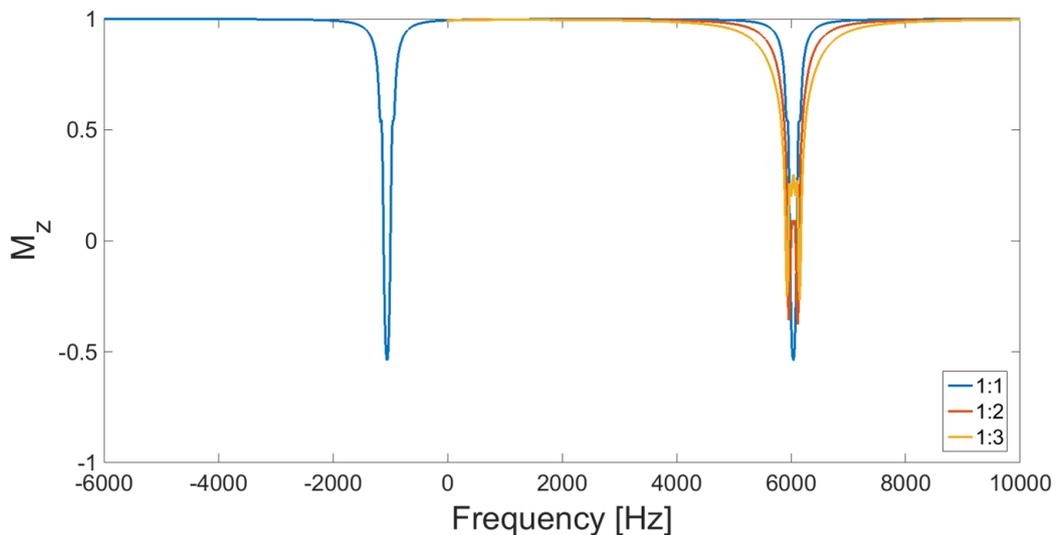
Figure 3.14: The longitudinal magnetisation M_z after the application dual-frequency pulses with $\alpha : \beta$ ratios of f_1 and f_0 was of 1:1, 1:2 and 1:3 with $B_{1,sat}$ in the f_1 pulse of 2.44 μT.

3.9.3   Simulations

To assess the effectiveness that the dual-frequency RF saturation pulses have on the z-spectrum, the designed pulses were applied in a 4-pool Bloch-McConnell model [43] incorporating the effects of chemical exchange between MT, NOE and CEST with the bulk free water on the longitudinal magnetisation (described in

Section 3.5). The RF saturation pulse train consisted of dual-frequency band pulses with α and β in ratios of 1:1, 1:2 and 1:3. The pulse trains consisted of 20 RF saturation pulses with duty cycle of 50% and nominal peak B_1 amplitudes of 2.53, 3.80 and 5.06 μT relating to $B_{1,rms} = 0.43$, 0.86 and 1.29 μT. The parameters governing the relaxation, exchange rate, concentrations (given as a fraction of equilibrium magnetisation of the pool M_0 by the equilibrium magnetisation of the free water M_0^f) and chemical shifts of the 4 pools used in the simulations are detailed in Table 3.1.

Table 3.1: The relaxation, exchange rate, concentrations and chemical shifts parameters used in the 4-pool model.

	Bulk Water	Bound Pool	APT Pool	NOE Pool
T_1	1.2 s	1 s	1 s	1 s
T_2	80 ms	9 μs	30 ms	0.5 ms
M_0 / M_0^f	-	12 %	1 %	5 %
k	-	50 Hz	20 Hz	10 Hz
Chemical Shift	-	-700 Hz	1050 Hz	-1050 Hz

Evolution of the MT and NOE Magnetisation

The evolution of the magnetisation from the MT pool, M_0^b at 6000 Hz (20 ppm), which is being saturated by f_0, and the NOE pool at -1050 Hz (-3.5 ppm) is shown in Figure 3.15. For increased β powers, more of the magnetisation from the macromolecular bound pool is saturated (Figure 3.15(a)) and therefore allows more of the saturation power in the sweeping f_1 to saturate the NOE rather than the MT at -3.5 ppm. The evolution of the NOE magnetisation M_0^n for $B_{1,rms} = 0.43$ μT is shown in Figure 3.15(b) and illustrates that after 20 saturation pulses the NOE magnetisation is almost completely saturated.
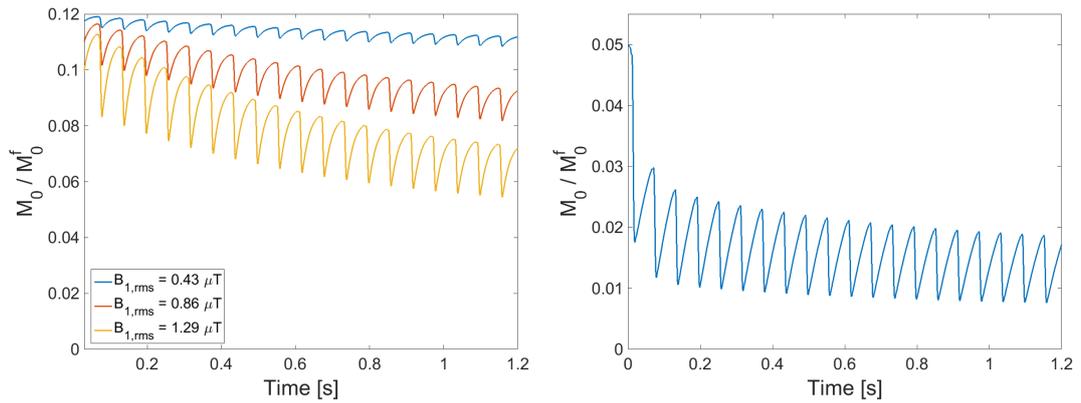
(a) Evolution of M_0^b/M_0^f at 6000 Hz   **(b)** Evolution of M_0^n/M_0^f at -1050 Hz

Figure 3.15: The evolution of the macromolecular bound pool M_0^b and the NOE pool M_0^n during the application of dual-frequency saturation pulses, $\alpha{:}\beta$ = 1:1, 1:2 and 1:3.

Effect on Z-spectra

The simulated z-spectra for the conventional single and dual band ($\alpha{:}\beta$=1:1) saturations are shown in Figure 3.16. The resultant dual-band z-spectrum indicates that the addition of a fixed frequency at 6000 Hz suppresses the MT contribution to the z-spectra but leaves the NOE and CEST unaffected and visually enhanced.
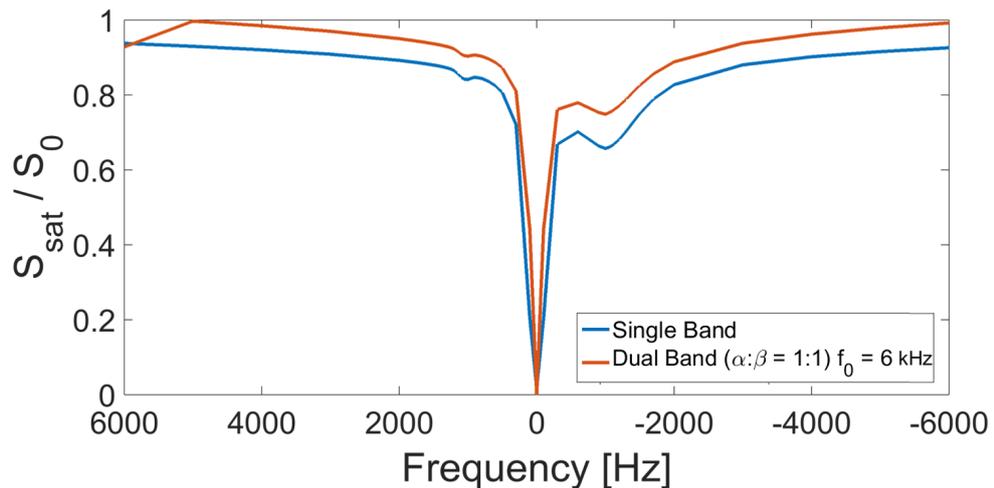
Figure 3.16: Simulated z-spectra for the single and dual-frequency band saturation for $B_{1,rms} = 0.43$ μT.

3.9.4   Phantom Validation and Sequence Optimisation

To validate the effect that the dual-frequency band saturation pulses have on suppressing the MT and to optimise the ratio of α and β, a phantom of bovine serum albumin (BSA) was made. The phantom was composed of 10% BSA (3.037 g for 24 ml of distilled water) and was prepared by mixing the BSA in the distilled water at room temperature and allowing it to dissolve over several hours. Once fully dissolved the BSA solution was placed in a small cylindrical test tube and 1 ml Glutaraldehyde was added to cross link the BSA. The solution was slowly mixed via inversions of the tube to ensure even consistency and was placed in the refrigerator to set. During scanning the BSA phantom was placed in a holder surrounded by water to minimise the effects of susceptibility artefacts and to ensure that the RF transmit coil had enough loading. The phantom was used to investigate the effect of varying the saturation parameters α and β, the number of pulses in the saturation train and the frequency of the fixed saturation.

Optimum Number of Pulses in Saturation Train

As already highlighted in Figure 3.12(b), the number of RF saturation pulses in the saturation train is key to achieving a steady state (or close to steady state) condition. The more pulses in the saturation train, the more the MT is attenuated in the z-spectra for the conventional single band saturation, as shown in Figure 3.17 by the dashed lines. Assessing the impact of the dual-frequency saturation pulses on the acquired z-spectra, Figure 3.17 (solid lines) shows the dual-frequency saturation, with α:β of 1:1 for a $B_{1,rms} = 0.43$ μT (duty cycle 50%) and fixed f_0 at 6 kHz (20 ppm) away from water indicating that the difference between 20 and 30 pulses is minimal. Therefore 20 pulses were used in the *in vivo* z-spectra acquisition to reduce the SAR and to allow more off-resonance frequencies to be sampled.
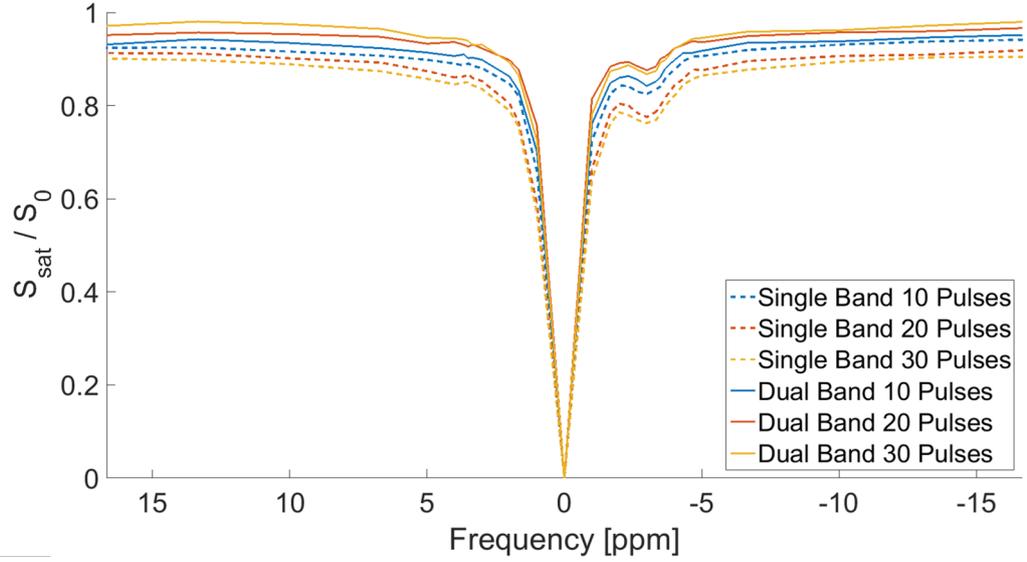
Figure 3.17: The z-spectra ($B_{1,rms}$ =0.43 μT) achieved for single frequency saturation and dual-frequency saturation ($\alpha = \beta = 1$) with the (a) 10, (b) 20 and (c) 30 RF saturation pulse in the saturation train.
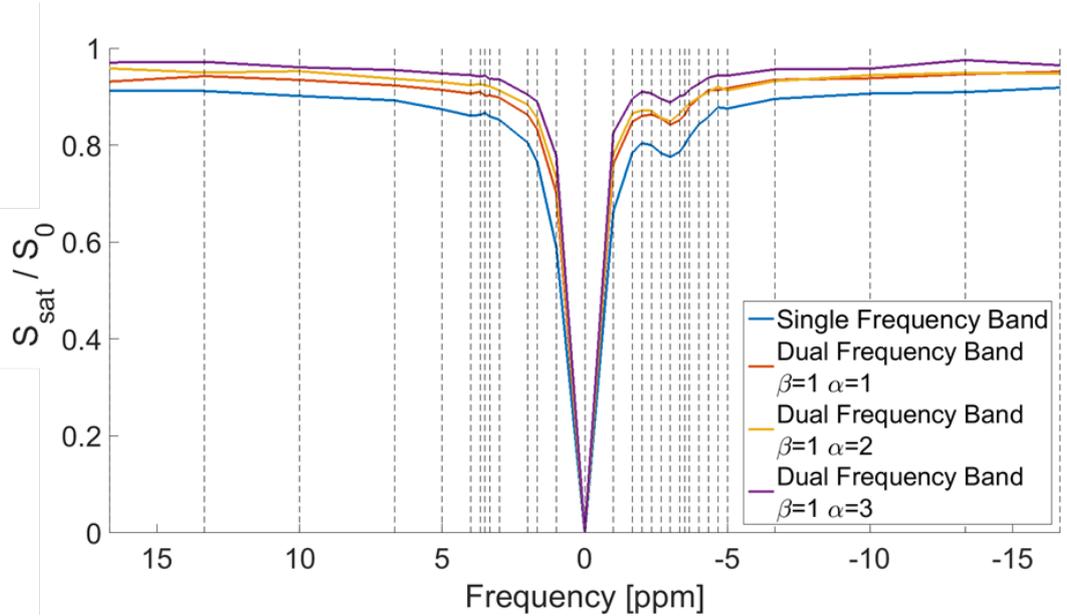
Figure 3.18: The z-spectra ($B_{1,rms} = 0.43$ μT) acquired for single frequency saturation and dual-frequency saturations for α:β ratios of 1:1, 1:2 and 1:3. The vertical dashed lines represent the location of sampled frequencies in the z-spectrum.

Optimum Ratio of Power Distribution Between Frequency Bands

The distribution of power in the frequency bands f_0 and f_1 delivered by the dual-frequency saturation Gaussian windowed sinc (Equ. 3.18) requires optimisation

to achieve the best suppression of MT whilst not limiting the saturation of the NOE and CEST. Once the NOE or CEST are fully saturated, any additional power at that frequency will only result in additional saturation of the MT. Figure 3.18 shows increased values of β lead to more suppression of the MT in the z-spectra. It was found that the optimum power distribution ratio (α:β) was between 1:3 and 1:4 to fully suppress the MT in the BSA phantom whilst enhancing the visualisation of both the NOE and CEST. Ultimately a limiting factor of the scanner is the restriction of the maximum amplitude of the B_1 through the transmit coil. The (NOVA Medical) volume T/R coil was limited to 15 μT and therefore using a power ratio of 1:4 was not feasible *in vivo*.
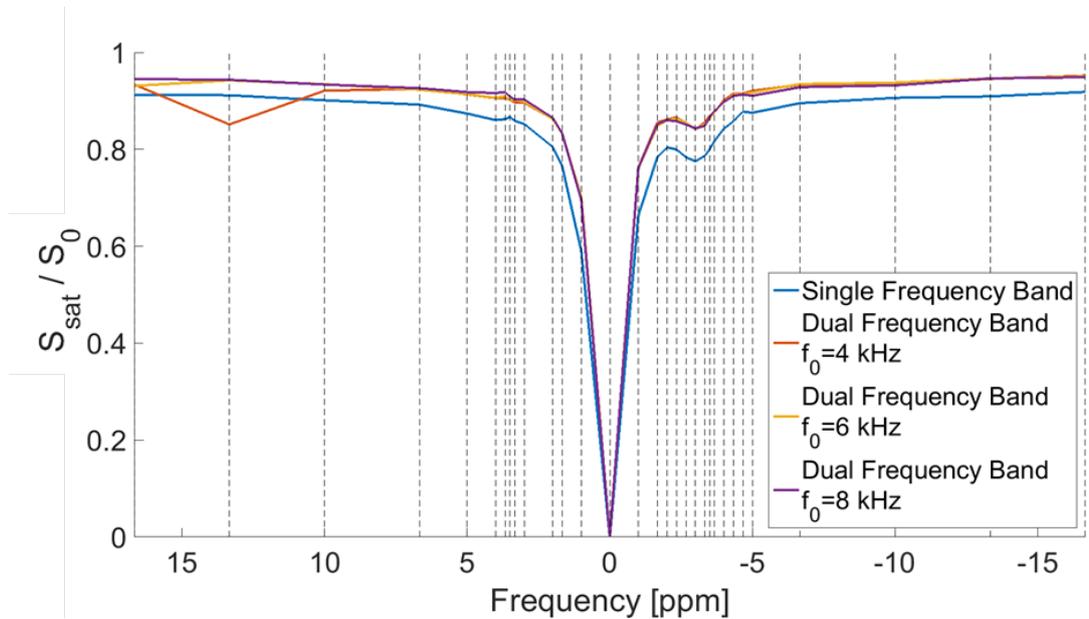
Figure 3.19: The z-spectra ($B_{1,rms} = 0.43$ μT) acquired for single frequency saturation and dual-frequency saturation (α:β=1:1) with the location of the fixed f_0 frequency located at 4, 6 and 8 kHz. Note that the peak at 13 ppm is the fixed saturation when $f_0 = 4$ kHz. The vertical dashed lines represent the location of sampled frequencies in the z-spectrum.

Location of Fixed Saturation

The location of the fixed frequency saturation f_0 band is also an important consideration as f_0 needs to suppress the MT whilst not directly affecting the

CEST and NOE pools. The MT spectrum is broad but the closer the f_0 band is to the central resonance of the MT spectrum (-2.4 ppm away from water) the more efficiently the MT will be saturated. Pulses with a higher β value excite wider bandwidths (seen in Figure 3.14 at 6 kHz) and could affect the APT signal at 3.5 ppm if the fixed pulse is moved too close to the water frequency at 0 ppm. To examine this, the fixed frequency band was applied at 4, 6 and 8 kHz (13.33, 20 and 26.66 ppm respectively) for dual-frequency saturation pulses with $\alpha=\beta=1$, and the resultant z-spectra are shown in Figure 3.19. It can be seen that the location of f_0 between 4-8 kHz has little effect on suppression of the MT.

3.9.5   Other Optimisation Considerations

For the optimisation of the sequence, the effect that the dual-frequency pulses have on the SAR must also be considered. The RF power deposited is doubled for 1:1 dual-frequency pulses compared to the conventional single band pulses of the same amplitude. As β is increased to improve the MT suppression, it is limited by regulations on the SAR allowed *in vivo* with each acquisition. The SAR level can be reduced by increasing the time between each off-resonance acquisition, and although this does not have a detrimental effect on the z-spectra, it does increase scanning times. It is important to keep the acquisition times short to minimise motion artefacts and to maximise the number of off-resonance frequencies sampled in the z-spectrum.

3.9.6   *In vivo* Acquisition

The dual-frequency band saturation simulations and phantom validation experiments show that the RF pulses suppress the MT from the macromolecular bound pool whilst not significantly affecting magnetisation exchange from other mobile protons pools in chemical exchange with water. Therefore the next stage was to

3.9. Dual-Frequency Magnetisation Transfer Suppression

acquire z-spectrum images *in vivo* using the designed dual-frequency saturation pulses.

All MRI experiments were conducted on a 7T Philips Achieva with a volume transmit RF coil and Nova 32 channel receive array. Following local ethical approval, three healthy volunteers were scanned (one male & two female). Each z-spectrum image was acquired using a saturation-prepared 3D-TFE sequence shown in Figure 3.20. The RF saturation consisted of a train of N = 20 Gaussian windowed sinc or dual-frequency modulated (with $f_0 = 6$ kHz and $\alpha{:}\beta = 1{:}3$) Gaussian windowed sinc RF pulses of bandwidth BW = 200 Hz, 30 ms long, repeated every T = 60 ms (50% duty cycle), with a phase increment between each pulse. A spoiler gradient applied at the end of the saturation train was used to remove any residual transverse magnetisation.
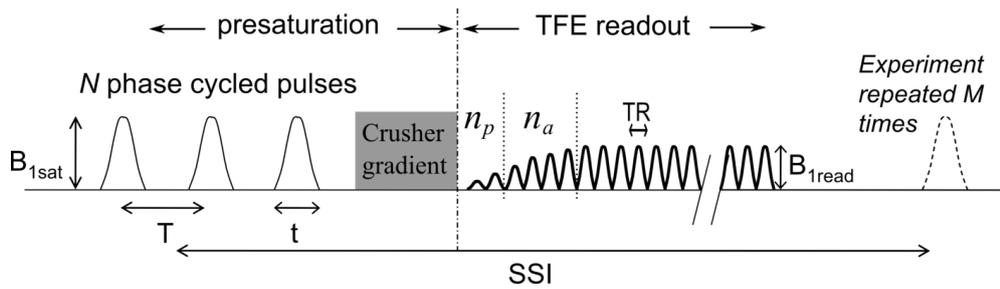
Figure 3.20: The magnetisation transfer-prepared turbo field echo (MT-TFE) sequence: presaturation period followed by the TFE readout. The presaturation period consists of $N = 20$ Gaussian windowed sinc pulses. The duty cycle of 50% was used such that $t = 30$ ms and $T = 60$ ms. The crusher gradient at the end of the saturation train removes any residual transverse magnetisation. $n_p = 2$ and $n_a = 4$ are the number of ramped RF pulses before and at the start of the acquisition, respectively. Adapted from [43].

Z-spectra were acquired by varying the off-resonance saturation frequency (f_1) with off-resonances unevenly sampled between ± 20 ppm. A 50 kHz off-resonance saturation was used for normalisation of the conventional single frequency band saturation. The normalisation of the dual-frequency z-spectra was achieved by turning off the power in the sweeping (f_1) frequency band (i.e. $\alpha{:}\beta = 0{:}3$). The 3D-TFE readout consisted of a train of 410 gradient echoes, TR/TE/FA = 8 ms/2.8 ms/8°, FOV = $192 \times 186 \times 60$ mm^3, 1.5 mm isotropic image

resolution and low-high k-space acquisition. The 3D volume acquisition required 3 repetitions of this cycle. The amplitude of readout pulses was modulated to avoid large variations in signal at the start of the TFE train there were 2 (n_p) ramped RF pulses before acquisition, followed by 4 (n_a) ramped RF pulses at the start of the acquisition, with the remaining pulses at constant flip angle $\alpha = 8°$ and a SENSE factor (RL) of 2. A typical single band z-spectrum acquisition with 40 off-resonance frequencies using a TFE readout takes ~ 10 minutes. Dual band z-spectra acquisition of 40 off-resonance frequency took us ~ 20 minutes, and for any longer volunteers struggled to keep still.

In addition to the acquisition of the z-spectra, a double echo B_0 map was acquired to correct the z-spectra for B_0 field inhomogeneities. A B_1 map (dual TR) was also collected to map the RF saturation profile and a Phase Sensitive Inversion Recovery (PSIR) was obtained to separate the grey and white matter of the brain and obtain a T_1 map. The PSIR sequence is an inversion recovery sequence which acquires two images, one where the grey matter and white matter have equal and opposite signals (i.e. equal signals in the unsigned magnitude image, or null point image) and another image at a later TI. At 7T this has been optimised with TIs of 780 ms and 2380 ms [44]. The calculated T_1 map gives accurate values for the WM and GM, for which it is optimised for.

3.9.7 Data Pre-Processing

Both the single and dual-frequency band z-spectra datasets were motion corrected using *mcflirt* (FSL[1]) and co-registered on the same image space using a high Contrast to Noise Ratio (CNR) image created by averaging across all of the off-resonance frequencies of the z-spectrum acquired for the single frequency band. SPM[2] was used to segment the white matter (WM) and grey matter (GM) from the PSIR to create masks that were retrospectively registered onto

---

[1]FMRIB Software Library v6, fsl.fmrib.ox.ac.uk
[2]Statistical Parametric Mapping v8, http://www.fil.ion.ucl.ac.uk/spm/

z-spectra space. The masks were thresholded at high probability values ($\sim$0.9) to avoid partial volume errors.

(a) Uncorrected z-spectra

(b) B_0 corrected z-spectra
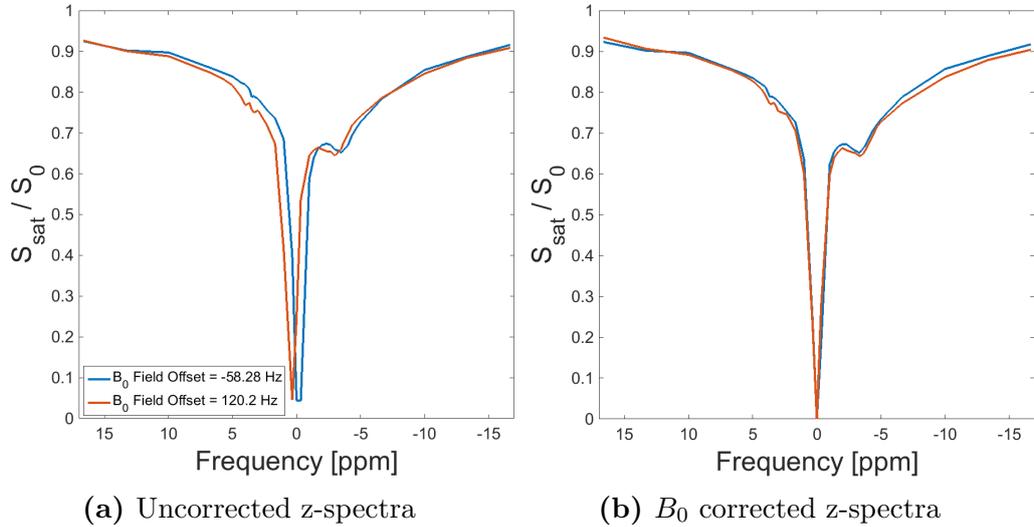
Figure 3.21: (a) Two z-spectra (without MT suppression) in the WM with large B_0 field frequency offsets showing the shift in the z-spectra around 0 ppm. (b) The respective B_0 corrected z-spectra.

Z-Spectra B_0 Correction

As outlined in Section 3.6, the acquired z-spectra have to be corrected for variation in the B_0 field. Figure 3.21(a) shows that if the z-spectra are not corrected, the resultant z-spectra are shifted away from 0 ppm by the inhomogeneity in the B_0 field. The z-spectra have (in this example) 40 off-resonance data points. Interpolating between the first and last point ($\pm$20 ppm) on the z-spectrum for steps of 0.01 ppm using a piece-wise interpolation method, the shape of the z-spectrum is retained but now has approximately 4000 data points. From here the whole spectrum is shifted by the difference between the direct water saturation position and the frequency shift measured by the acquired B_0 map. Finally the shifted interpolated spectra is re-sampled back to the original off-resonance frequencies. Figure 3.21(b) shows the B_0 corrected z-spectra for the two z-spectra shown in Figure 3.21(a). A problem for z-spectra imaging occurs when

the optimised off-resonances sampling of the CEST peaks in the z-spectrum are shifted by large B_0 inhomogeneities. This results in the peak being sampled in the wrong place and in the worst case scenario, the CEST peak might not even be sampled at all.

3.9.8   Assessing MT Suppression

The effectiveness of the MT suppression by the dual-frequency band pulses and quantification of the NOE and APT was assessed by using the multi-Lorentzian model fitting [36] (outlined previously in Section 3.7). For both the single and dual-frequency band z-spectra, a Lorentzian for the direct water saturation and a super-Lorentzian for the MT were fitted and subsequently subtracted away to reveal the remaining NOE and CEST contrast.

The NOE and CEST contrast revealed by the subtraction of the MT and DS were also separated using the multi-Lorentzians fit. Along with the fitted MT and DS, Lorentzians for the NOE at -3.5 and -2 ppm and the amides and amines at 3.5 and 2.2 ppm respectively were fitted to each z-spectra. Summing all the fitted Lorentzians (and the super-Lorentzian) forms a reference z-spectrum (Z_{ref}), and subtracting the Lorentzian for the proton pool of interest from Z_{ref} yields a label z-spectrum (Z_{label}). For example the Z_{label} for the APT is calculated as,

$$Z_{label} = Z_{ref} - L_{amide}, \tag{3.19}$$

where L_{amide} is an array representing the Lorentzian fitted to the amide peak at 3.5 ppm. The Z_{ref} and Z_{label} for each CEST and NOE pool are used to calculate the MTR uncorrected Lorentzian difference,

$$MTR_{LD} = Z_{ref} - Z_{lab} = L_{amide}, \tag{3.20}$$

and inverse MTR Lorentzian difference which has been show to remove the de-

pendence on the MT and direct water saturation, and have a linear relationship with T_1 [45],

$$MTR_{Rex} = \frac{1}{Z_{label}} - \frac{1}{Z_{ref}}.$$

(3.21)

The MTR_{Rex} values are converted to the apparent relaxation compensated contrast (AREX) by dividing MTR_{Rex} by T_1 [46].

3.9.9 Results

White Matter and Grey Matter MT Suppression

Comparing the dual-frequency saturation z-spectra to the conventional single band saturation for averaged whole head WM and GM, Figure 3.22 shows the dual-frequency pulses (with α:β of 1:3) significantly suppressed the background MT spectrum in both the WM and GM whilst leaving the detected NOE and CEST signal largely unchanged.

The subtraction of the fitted super Lorentzian for the MT and Lorentzian for the DS away from the WM and GM z-spectra in Figure 3.22(a) and 3.22(b) respectively shows that the NOE and CEST signals in the averaged whole head WM and GM are somewhat suppressed by the MT suppression by the dual-frequency saturation. Furthermore the suppressed MT z-spectrum for the WM has significantly less variation in the signal baseline, with the standard deviation shown by the grey shaded area behind each z-spectrum.

For the three subjects, the averaged area under the curve (AUC) for super-Lorentzians fitted for each individual z-spectra in the WM and GM are shown in Figure 3.23(a), with the MT being suppressed by 46 $\pm$ 8% and 31 $\pm$ 16% in the WM and GM respectively. Comparing this suppression to the AUC for the NOE and APT shown in Figure 3.23(b) and (c), the dual band frequency suppression only suppressed the NOE by 12 $\pm$ 9% and 24 $\pm$ 7% in the WM and
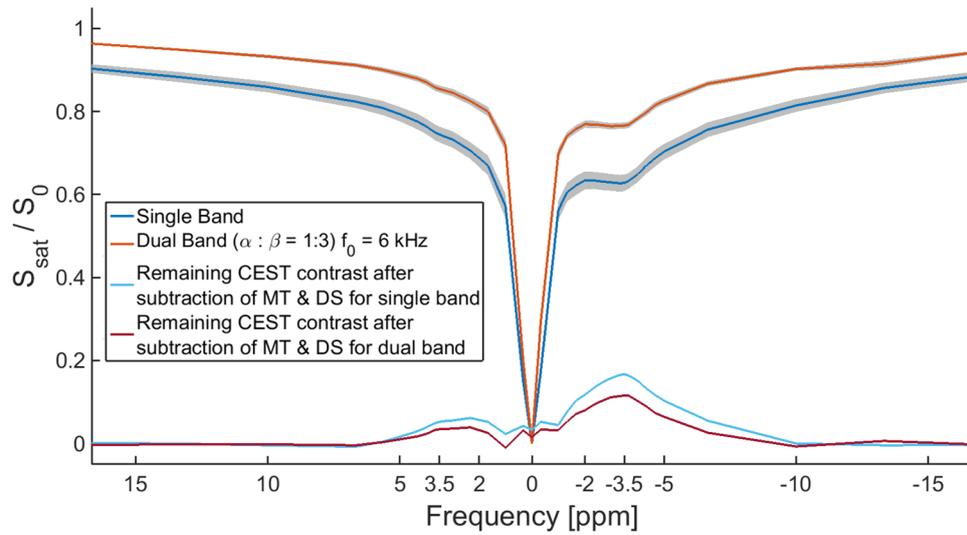
(a) White Matter
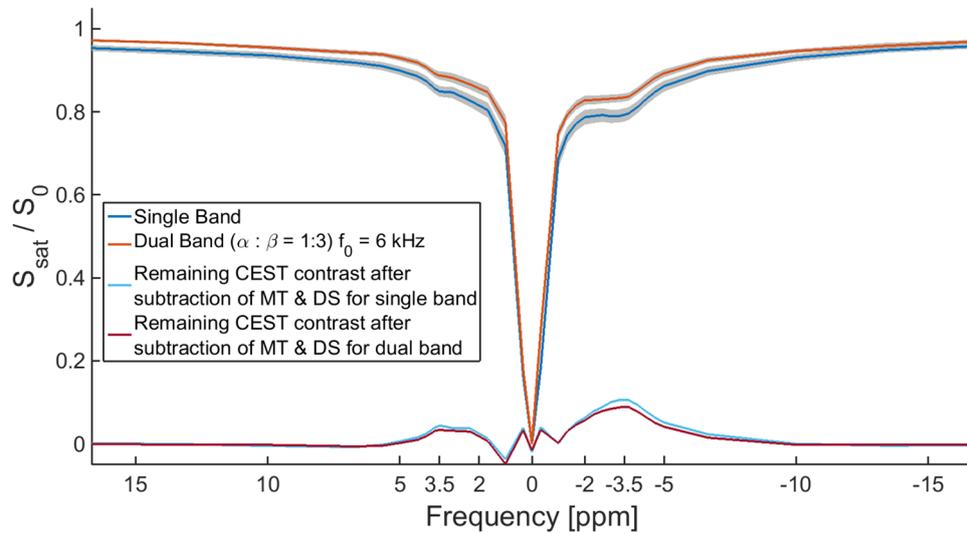
(b) Grey Matter

Figure 3.22: The averaged (a) WM and (b) GM z-spectra for both single and dual band saturation (α:β = 1:3) and $f_0 = 6$ kHz with the standard deviation for each off-resonance shown by the grey shaded area. Below the z-spectra is the revealed CEST and NOE signals after the fitted MT and DS lineshapes are subtracted.

GM respectively, and the APT was suppressed by $13 \pm 19\%$ and $10 \pm 21\%$ in the WM and GM respectively.

3.9. Dual-Frequency Magnetisation Transfer Suppression

(a) AUC of MT   **(b)** AUC of NOE   **(c)** AUC of APT
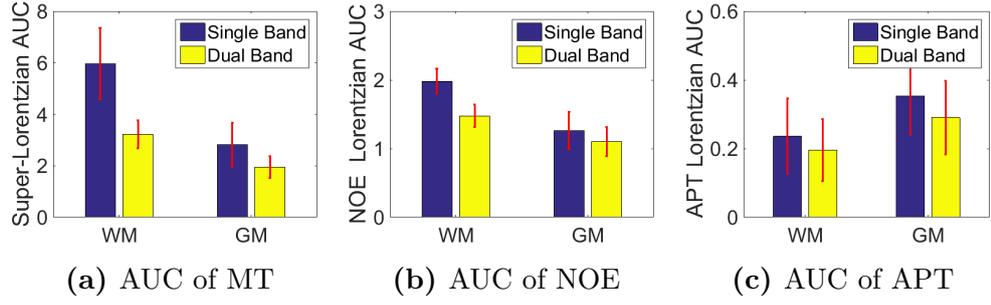
Figure 3.23: WM and GM averaged area under the curve (AUC) for the fitted super-Lorentzians for the MT lineshape and Lorentzians for the APT and NOE (at ± 3.5 ppm) across the three subjects, with the MT in the WM and GM being suppressed by $46 \pm 8\%$ and $31 \pm 16\%$ respectively.

(a) Single Band Lorentzian Fit   **(b)** Dual Band Lorentzian Fit
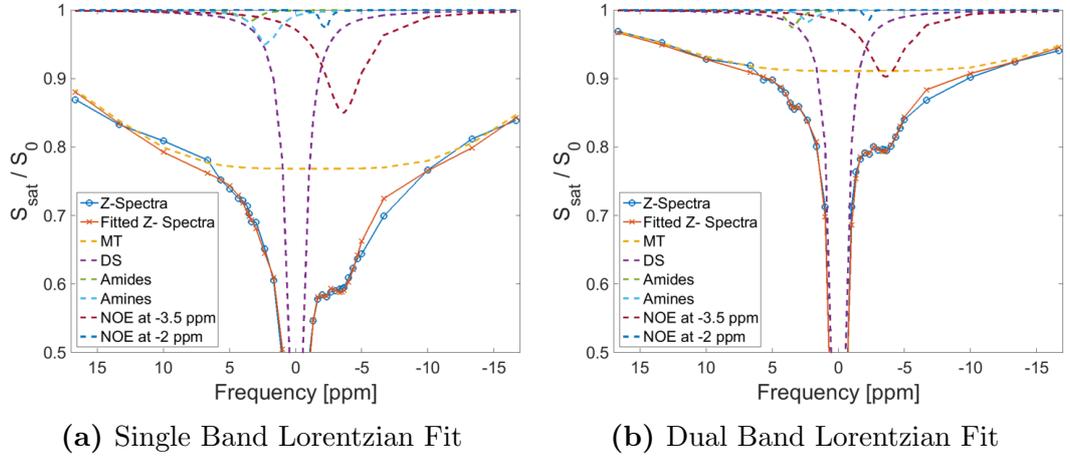
Figure 3.24: Multi-Lorentzian Fit for the (a) single band and (b) dual-frequency band z-spectra for an ROI in the corpus callosum.

Z-Spectra Noise Calculations

To calculate the noise σ_z in both the single and dual-band z-spectra ($Z = S_{sat}/S_0$), the variance in the S_0 signal, σ_{S0} at normalisation off-resonance frequencies (50 kHz for the single band and 6 kHz for the dual-band) and S_{sat} signal at -3.5 ppm, σ_{Ssat}, such that,

$$\sigma_z^2 = \left(\frac{\partial Z}{\partial S_0}\right)^2 \sigma_{S0}^2 + \left(\frac{\partial Z}{\partial S_{sat}}\right)^2 \sigma_{Ssat}^2, \qquad (3.22)$$

$$\sigma_z^2 = \frac{S_{sat}^2}{S_0^4}\sigma_{S0}^2 + \frac{1}{S_0^2}\sigma_{Ssat}^2 = \frac{S_{sat}^2 + S_0^2}{S_0^4}\sigma^2, \qquad (3.23)$$

if $\sigma_{S0} \approx \sigma_{Ssat}$ and the noise σ_z in the single and dual frequency band z-spectra was calculated and showed that the dual band z-spectra had 10% more noise compared to the single band z-spectra, as the S_0^4 denominator in Equ. 3.23 is a smaller value for the dual-frequency S_{sat} compared to the single band.

Multiple Components in NOE

Assessing the z-spectra ROIs for regions in the WM (which has higher concentrations of NOE and MT compared to GM), Figure 3.25 shows that for the (a-c) splenium, (d-f) genu and (g-l) normal WM there are two peaks (at -2 and -3.5 ppm) in the NOE across the three subjects. The subtraction of the fitted MT and DS lineshapes revealed the remaining CEST and NOE contrast and showed the two peaks in the NOE.

MTR$_{\mathrm{LD}}$ and AREX Maps for NOE and CEST

For both the single and dual band saturations, the MTR$_{\mathrm{LD}}$ and AREX (from Equ. 3.20 and 3.21) maps for two NOE peaks, amides and amines from the threes subject are shown in Figure 3.26, 3.27 and 3.28. The MTR$_{\mathrm{LD}}$ and AREX for the NOE at -3.5 ppm shows similar concentrations levels, however the dual-band appears sightly nosier. The second NOE peak around -2 ppm has higher concentration in the WM, and for the dual-frequency saturation in both the MTR$_{\mathrm{LD}}$ and AREX the NOE at -2 ppm appears to be less dependent on B_1 transmit field.

The amide and amine MTR$_{\mathrm{LD}}$ and AREX maps for the single band saturation show correlation with the B_1 transmit field, whereas for the dual band saturation the effective proton pool size measured by the MTR$_{\mathrm{LD}}$ and AREX appear more homogeneous.
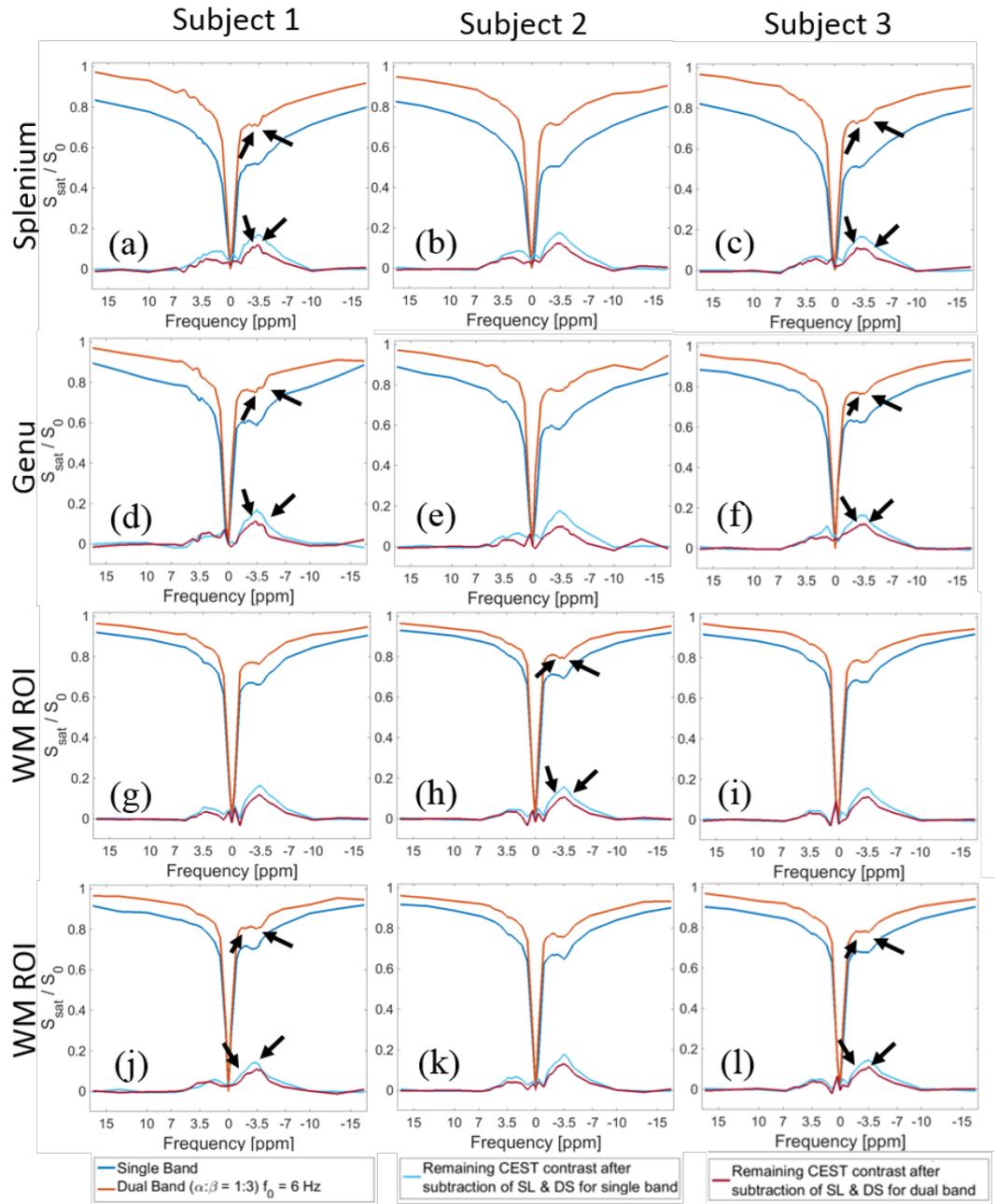
Figure 3.25: Z-spectra from WM ROIs in the corpus callosum: (a,b & c) splenium, (d,e & f) genu and (g, h, i, j ,k & l) WM ROIs away from the corpus callosum for both the conventional single band saturation and dual-frequency band saturation pulses for all three subjects. The fitted lineshapes for the MT and DS are subtracted from the z-spectra to reveal the remaining CEST contrast for all the z-spectra, and arrows indicating the two peaks in the NOE.
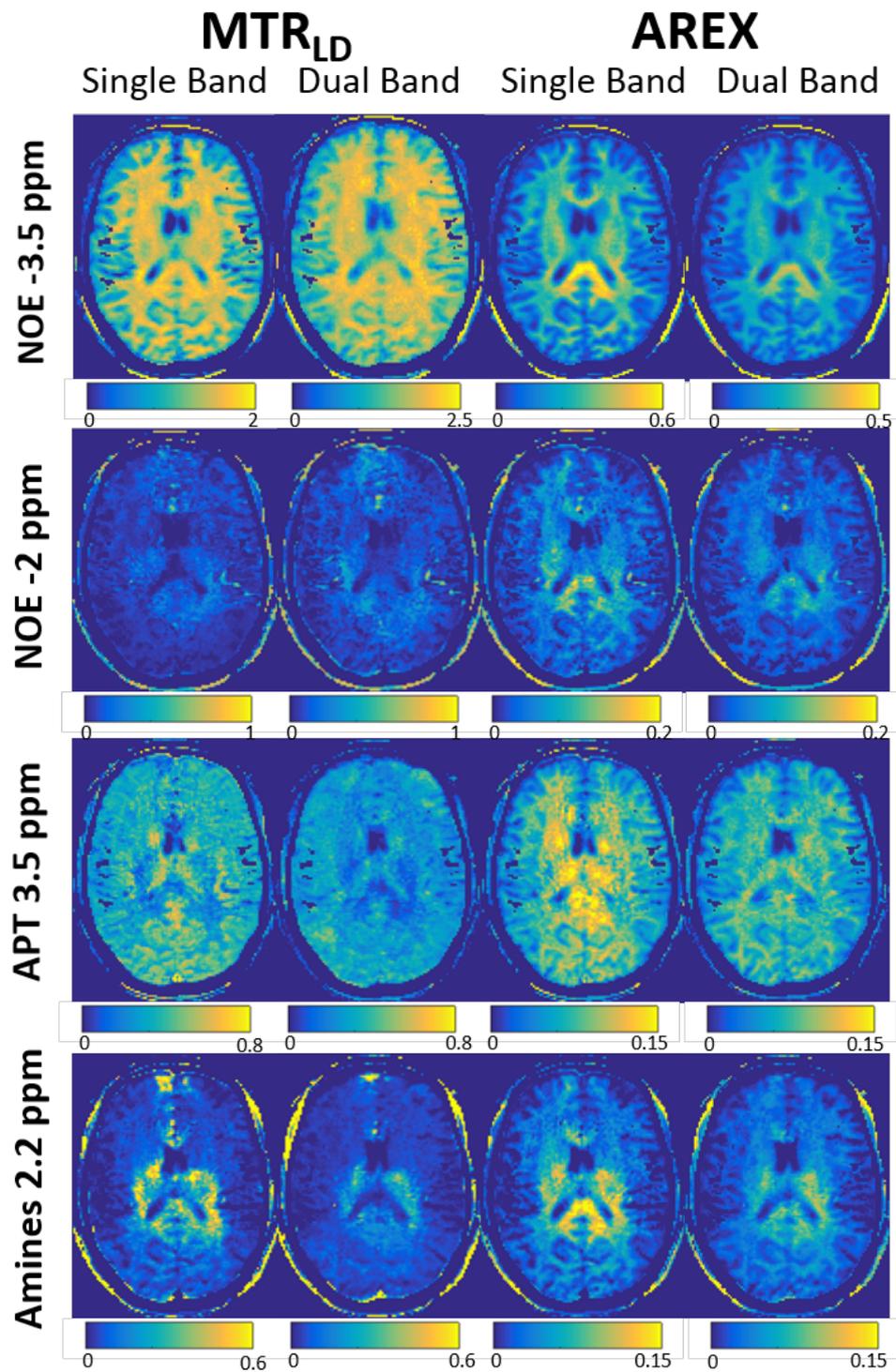
Figure 3.26: MTR$_{LD}$ and AREX maps for the NOEs (at -3.5 ppm and -2 ppm) and the APT and amines (at 3.5 ppm and 2.2 ppm) for the single and dual saturation z-spectra acquisition from subject one.
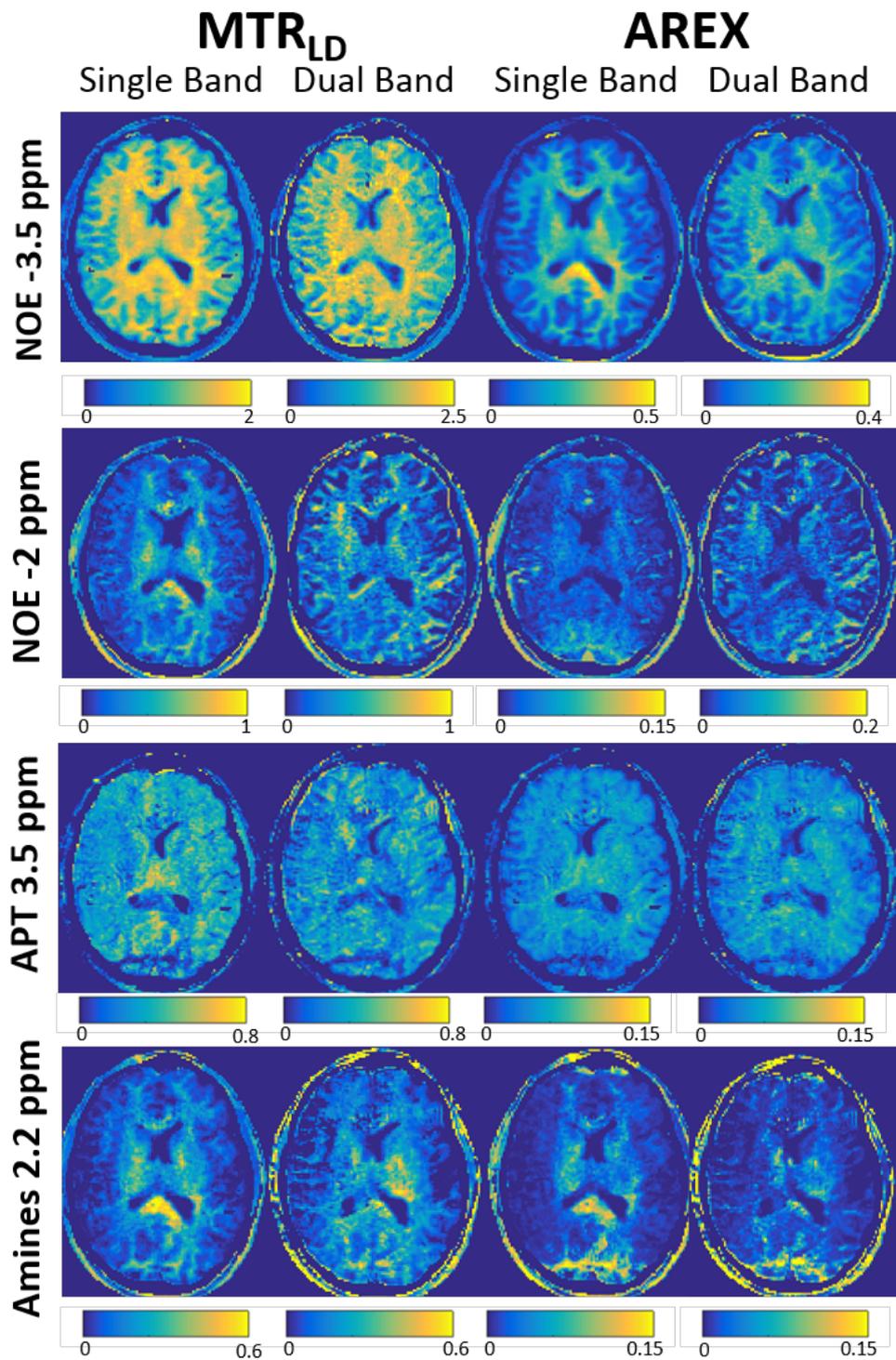
Figure 3.27: MTR$_{LD}$ and AREX maps for the NOEs (at -3.5 ppm and -2 ppm) and the APT and amines (at 3.5 ppm and 2.2 ppm) for the single and dual saturation z-spectra acquisition from subject two.
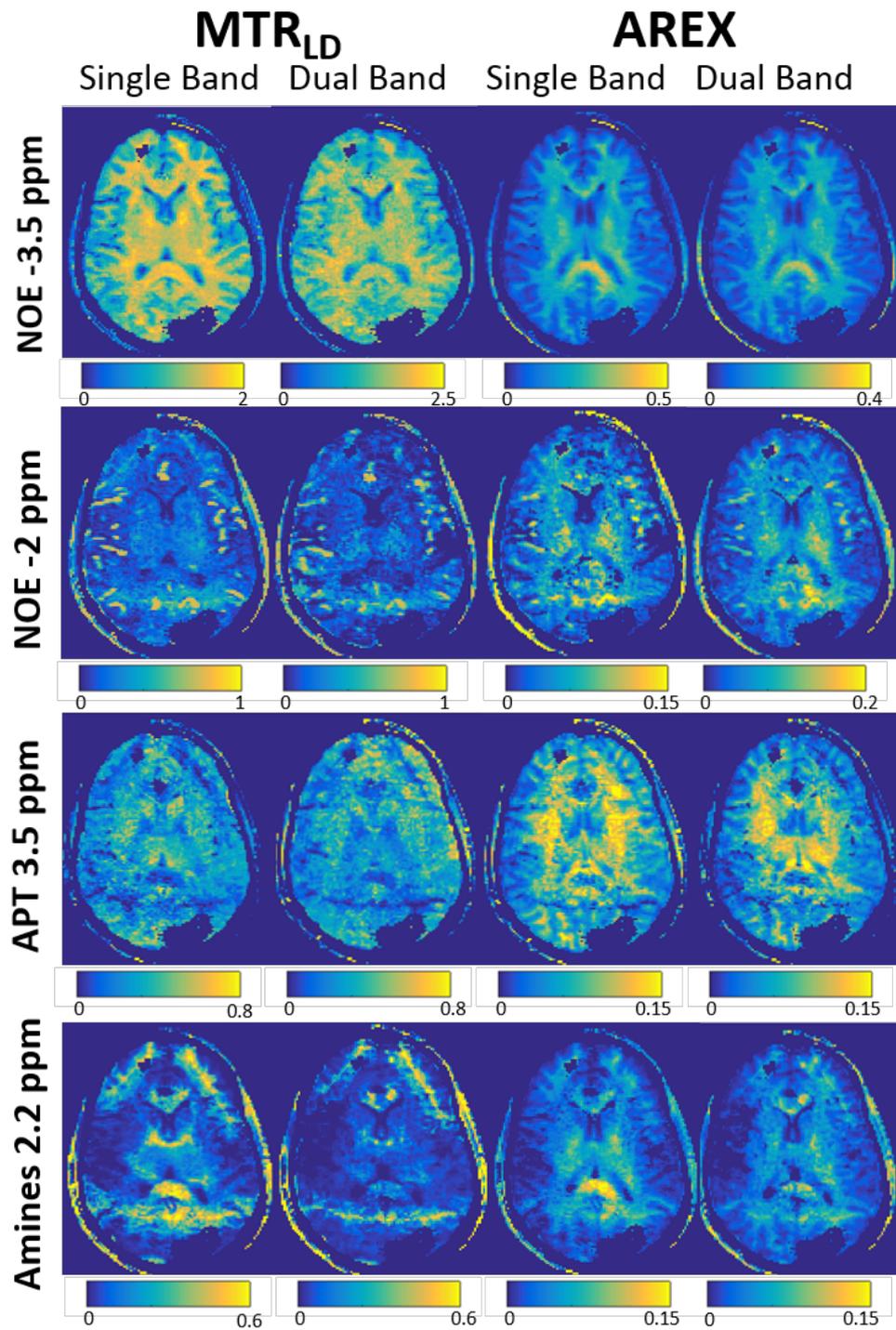
Figure 3.28: MTR_{LD} and AREX maps for the NOEs (at -3.5 ppm and -2 ppm) and the APT and amines (at 3.5 ppm and 2.2 ppm) for the single and dual saturation z-spectra acquisition from subject three.

3.9.10 Discussion

The dual-frequency saturation pulses are an efficient method of suppressing the MT across both the WM and GM z-spectra, uncoupling the CEST and NOE effects from the MT associated with the macromolecular bound pool. The suppression of the MT allowed enhanced visualisation of the CEST and NOE, and also highlighted a NOE peak around -2 ppm that was previously masked by the MT, in the mapping of the z-spectra using a single frequency saturation pulse.

Simulation of the dual-frequency band pulses indicated that 6 kHz was the optimal location of f_0, ensuring that the APT at 3.5 ppm (1050 Hz) remained unaffected by the fixed saturation. Validation of the pulses using a BSA (cross-linked with Glutaraldehyde) phantom suggested that the power distribution ratio α:β of 1:1 pulses suppressed the MT but higher values of β suppress more of the MT required for *in vivo* acquisition to uncouple the MT from CEST and NOE effects. The ratio of α:β of 1:3 was chosen after the phantom validation suggested that it offered the best suppression of MT whilst SAR constraints were not violated.

With $f_0 = 6$ kHz, 20 saturation pulses in the pulse train and a power distribution ratio of α:$\beta = 1:3$, the *in vivo* z-spectra acquisition successfully suppresses the MT by $46 \pm 8\%$ in WM and by $31 \pm 16\%$ in GM. The suppression of the MT, also enhances the visualisation of the NOE and CEST. The averaged whole head z-spectra standard deviation for the WM was much lower for the dual saturation, and would suggest that the effects that are seen in the z-spectra are less affected by the B_1 inhomogeneity, due to the MT and CEST pools being closer to full saturation. Noise calculations suggest that the dual-band z-spectra has 16% more noise but this is not seen in the z-spectra. The NOE and APT are suppressed less in the WM compared to the MT resulting in enhanced visualisation of these effects.

3.9. Dual-Frequency Magnetisation Transfer Suppression

The dual-frequency saturation also reveals an additional second peak in the NOE (around -2 ppm) that is most apparent in the corpus callosum. The peak at -2 ppm can clearly be seen in Figure 3.25(a) and we postulate that the second peak in the NOE, visually enhanced in the dual-frequency band z-spectra is NOE mediated magnetisation transfer that is in faster exchange compared to the NOE at -3.5 ppm. The conventional single frequency band saturation RF pulses applied at -2 ppm saturate the NOE and MT, so the NOE at -2 ppm, which has a faster exchange rate and therefore has quicker recovery, is not always visibly seen in z-spectra. The advantage of the dual-frequency saturation RF pulses is that the fixed saturation f_0 in every off-resonance acquisition on the z-spectrum solely saturates the MT, leaving the sweeping f_1 band to saturate more of the NOE at -2 ppm, and therefore allowing more of the faster exchanging NOE to be saturated. Consequently more of it can be observed in the z-spectra.

The *in vivo* MTR$_{LD}$ and AREX maps shown in Figure 3.26 indicate that the measured effective proton pool sizes using the dual-frequency saturation are less sensitive to the inhomogeneity in the B_1 transmit field. The NOE AREX maps at -3.5 ppm are very similar suggesting that the dual-frequency saturation pulses do not affect the NOE signal. The APT MTR$_{LD}$ and AREX maps for the dual-frequency saturation suggest they are less sensitive to B_1 inhomogeneities in comparison to the conventional single frequency saturation. Also the B_0 field for subject three (Figure 3.28) was not homogeneous, like the other subjects, and as a result the NOE peak at -2 ppm and amines at 2 ppm were not sampled at the right frequencies. This can be seen in both the MTR$_{LD}$ and AREX maps where a line appears across the images, and shows that a homogeneous B_0 field is required to achieve good CEST contrast.

The simulations suggest that the dual-frequency saturation pulses would suppress most of the MT, and for the cross-linked BSA phantoms (Figure 3.18) the MT is fully suppressed for $\alpha{:}\beta = 1{:}3$. However, *in vivo* the MT in the WM is only suppressed on average by $\sim$50%. Given the limitation of the RF power it is

not possible to go to high values of β or add more pulses in the saturation train to suppress more of the MT. Also it has recently been reported that the MT lineshape is inhomogenously broadened (ihMT) [47, 48] and at 1.5T inhomogeneous broadening of the MT lineshape of up to 15% in areas of high myelination was observed. The ihMT effect could potentially account for up to 15% of the unsuppressed MT in the z-spectra as the sweeping frequency saturation band attenuates the inhomogeneous MT line.

Potential Applications

The suppression of the baseline MT in z-spectra has potential to sufficiently improve the identification of CEST and NOE effect at low field strengths and advance CEST contrast imaging closer to a clinical setting. At lower field strengths the linewidth separation, $\Delta\omega$, between the free water and the exchange proton pools are smaller. The high saturation powers used to attenuate the CEST and NOE is confounded by the greater contamination by DS and dominating MT lineshape. The dual-frequency saturation pulses could therefore potentially be used to eliminate the MT, and leave just the DS to deal with in quantification.

Here, the dual-frequency saturation pulses have been used to suppress the MT contribution to the z-spectra. However, it is feasible that the pulses could also be used to measure cross-relaxation processes. The origins of the NOE signal at -3.5 ppm are understood to be a combination of dipole-dipole interactions and exchanged relayed interactions. However the contribution of the two processes that gives rise to the peak at -3.5 ppm is currently unknown. By moving the fixed saturation band to 3.5 ppm where the amide protons resonate, and then sweeping the other frequency band over the NOE peak, it should be possible to separate the exchange relayed interactions from the dipole-dipole interactions.

3.9.11 Conclusion

The dual-frequency saturation pulses successfully suppress the MT contribution in z-spectra in both the white and grey matter, enhancing detection of the NOE and CEST peaks. The suppression of the MT also revealed a NOE peak around -2 ppm which was previously masked by the MT.

3.10 Summary

This chapter has outlined the principles of magnetisation transfer and chemical exchange saturation transfer, including the sources of the magnetisation transfer observed in z-spectra, the mathematical model that describes the exchange and methods of quantifying exchanging proton pools. Also outlined is the detrimental effect that MT from the macromolecular bound pool has on z-spectra and quantification. Finally dual-frequency RF saturation pulses are designed to suppress the MT contribution in z-spectra to enhance visualisation and quantification of CEST and NOE effects.

Bibliography

[1] Morrison, C., Stanisz, G. & Henkelman, R. M. Modeling magnetization transfer for biological-like systems using a semi-solid pool with a super-Lorentzian lineshape and dipolar reservoir. *Journal of Magnetic Resonance, Series B* **108**, 103–113 (1995).

[2] Wolff, S. D. & Balaban, R. S. Magnetization transfer contrast (MTC) and tissue water proton relaxation in vivo. *Magnetic resonance in medicine* **10**, 135–144 (1989).

[3] Guivel-Scharen, V., Sinnwell, T., Wolff, S. & Balaban, R. Detection of proton chemical exchange between metabolites and water in biological tissues. *Journal of Magnetic Resonance* **133**, 36–45 (1998).

[4] van Zijl, P. *et al.* Mechanism of magnetization transfer during on-resonance water saturation. A new approach to detect mobile proteins, peptides, and lipids. *Magnetic resonance in medicine* **49**, 440–449 (2003).

[5] Ward, K., Aletras, A. & Balaban, R. A new class of contrast agents for MRI based on proton chemical exchange dependent saturation transfer (CEST). *Journal of magnetic resonance* **143**, 79–87 (2000).

[6] Zhou, J., Payen, J.-F., Wilson, D. A., Traystman, R. J. & van Zijl, P. C. Using the amide proton signals of intracellular proteins and peptides to detect pH effects in MRI. *Nature medicine* **9**, 1085–1090 (2003).

[7] van Zijl, P. C., Jones, C. K., Ren, J., Malloy, C. R. & Sherry, A. D. MRI detection of glycogen in vivo by using chemical exchange saturation transfer imaging (glycoCEST). *Proceedings of the National Academy of Sciences* **104**, 4359–4364 (2007).

[8] Sun, P. Z., Benner, T., Kumar, A. & Sorensen, A. G. Investigation of optimizing and translating pH-sensitive pulsed-chemical exchange saturation

transfer (CEST) imaging to a 3T clinical scanner. *Magnetic resonance in medicine* **60**, 834–841 (2008).

[9] Liu, G., Song, X., Chan, K. W. & McMahon, M. T. Nuts and bolts of chemical exchange saturation transfer MRI. *NMR in Biomedicine* **26**, 810–828 (2013).

[10] Jones, C. K. *et al.* Nuclear Overhauser enhancement (NOE) imaging in the human brain at 7T. *Neuroimage* **77**, 114–124 (2013).

[11] Jin, T., Wang, P., Zong, X. & Kim, S.-G. MR imaging of the amide-proton transfer effect and the pH-insensitive nuclear overhauser effect at 9.4 T. *Magnetic resonance in medicine* **69**, 760–770 (2013).

[12] Forsén, S. & Hoffman, R. A. Study of moderately rapid chemical exchange reactions by means of nuclear magnetic double resonance. *The Journal of Chemical Physics* **39**, 2892–2901 (1963).

[13] Levitt, M. H. *Spin dynamics: basics of nuclear magnetic resonance* (John Wiley & Sons, 2001).

[14] Woessner, D. E. Brownian motion and its effects in NMR chemical exchange and relaxation in liquids. *Concepts in Magnetic Resonance* **8**, 397–421 (1996).

[15] Ishima, R. & Torchia, D. A. Estimating the time scale of chemical exchange of proteins from measurements of transverse relaxation rates in solution. *Journal of biomolecular NMR* **14**, 369–372 (1999).

[16] Woessner, D. E., Zhang, S., Merritt, M. E. & Sherry, A. D. Numerical solution of the Bloch equations provides insights into the optimum design of PARACEST agents for MRI. *Magnetic resonance in medicine* **53**, 790–799 (2005).

[17] Li, A. X. *et al.* Four-pool modeling of proton exchange processes in biological systems in the presence of MRI–paramagnetic chemical exchange

saturation transfer (PARACEST) agents. *Magnetic resonance in medicine* **60**, 1197–1206 (2008).

[18] Cercignani, M., Symms, M. R., Ron, M. & Barker, G. J. 3D MTR measurement: from 1.5 T to 3.0 T. *Neuroimage* **31**, 181–186 (2006).

[19] Kim, M., Gillen, J., Landman, B. A., Zhou, J. & van Zijl, P. Water saturation shift referencing (WASSR) for chemical exchange saturation transfer (CEST) experiments. *Magnetic resonance in medicine* **61**, 1441–1450 (2009).

[20] Zhou, J., Wilson, D. A., Sun, P. Z., Klaus, J. A. & van Zijl, P. Quantitative description of proton exchange processes between water and endogenous and exogenous agents for WEX, CEST, and APT experiments. *Magnetic resonance in medicine* **51**, 945–952 (2004).

[21] McMahon, M. T. *et al.* Quantifying exchange rates in chemical exchange saturation transfer agents using the saturation time and saturation power dependencies of the magnetization transfer effect on the magnetic resonance imaging signal (QUEST and QUESP): Ph calibration for poly-L-lysine and a starburst dendrimer. *Magnetic resonance in medicine* **55**, 836–847 (2006).

[22] Henkelman, R., Stanisz, G. & Graham, S. Magnetization transfer in MRI: a review. *NMR in Biomedicine* **14**, 57–64 (2001).

[23] Hua, J. *et al.* Quantitative description of the asymmetry in magnetization transfer effects around the water resonance in the human brain. *Magnetic resonance in medicine* **58**, 786–793 (2007).

[24] Geades, N. *et al.* Quantitative analysis of the z-spectrum using a numerically simulated look up table: application to the healthy human brain at 7T. *Magnetic Resonance in Medicine* in print (2016).

[25] Zaiss, M. *et al.* A combined analytical solution for chemical exchange satu-

ration transfer and semi-solid magnetization transfer. *NMR in Biomedicine* **28**, 217–230 (2015).

[26] Närväinen, J., Hubbard, P. L., Kauppinen, R. A. & Morris, G. A. Z-spectroscopy with alternating-phase irradiation. *Journal of Magnetic Resonance* **207**, 242–250 (2010).

[27] Scheidegger, R., Vinogradov, E. & Alsop, D. C. Amide proton transfer imaging with improved robustness to magnetic field inhomogeneity and magnetization transfer asymmetry using saturation with frequency alternating RF irradiation. *Magnetic resonance in medicine* **66**, 1275–1285 (2011).

[28] Zu, Z. *et al.* Imaging amide proton transfer and nuclear overhauser enhancement using chemical exchange rotation transfer (CERT). *Magnetic resonance in medicine* **72**, 471–476 (2014).

[29] Xu, X. *et al.* Magnetization transfer contrast–suppressed imaging of amide proton transfer and relayed nuclear overhauser enhancement chemical exchange saturation transfer effects in the human brain at 7T. *Magnetic resonance in medicine* **75**, 88–96 (2016).

[30] Khlebnikov, V. *et al.* Comparison of pulsed three-dimensional CEST acquisition schemes at 7 tesla: steady state versus pseudosteady state. *Magnetic Resonance in Medicine* (2016).

[31] Schneider, E., Prost, R. W. & Glover, G. H. Pulsed magnetization transfer versus continuous wave irradiation for tissue contrast enhancement. *Journal of Magnetic Resonance Imaging* **3**, 417–423 (1993).

[32] Schmitt, B., Zaiß, M., Zhou, J. & Bachert, P. Optimization of pulse train presaturation for CEST imaging in clinical scanners. *Magnetic resonance in medicine* **65**, 1620–1629 (2011).

Bibliography

[33] Xu, J. *et al.* Variable delay multi-pulse train for fast chemical exchange saturation transfer and relayed-nuclear overhauser enhancement MRI. *Magnetic Resonance in Medicine* **71**, 1798–1812 (2014).

[34] Dixon, W. T. *et al.* A multislice gradient echo pulse sequence for CEST imaging. *Magnetic Resonance in Medicine* **63**, 253–256 (2010).

[35] Dula, A. N. *et al.* Development of chemical exchange saturation transfer at 7T. *Magnetic resonance in medicine* **66**, 831–838 (2011).

[36] Zaiss, M., Schmitt, B. & Bachert, P. Quantitative separation of CEST effect from magnetization transfer and spillover effects by Lorentzian-line-fit analysis of z-spectra. *Journal of magnetic resonance* **211**, 149–155 (2011).

[37] Morrison, C. & Mark Henkelman, R. A model for magnetization transfer in tissues. *Magnetic resonance in medicine* **33**, 475–482 (1995).

[38] Yarnykh, V. L. Fast macromolecular proton fraction mapping from a single off-resonance magnetization transfer measurement. *Magnetic resonance in medicine* **68**, 166–178 (2012).

[39] Müller, D., Pampel, A. & Möller, H. E. Orientation dependence of magnetization transfer in human white matter. In *Proc. Intl. Soc. Mag. Reson. Med*, vol. 18, 2996 (2010).

[40] Pampel, A., Müller, D. K., Anwander, A., Marschner, H. & Möller, H. E. Orientation dependence of magnetization transfer parameters in human white matter. *NeuroImage* **114**, 136–146 (2015).

[41] Desmond, K. L. & Stanisz, G. J. Understanding quantitative pulsed CEST in the presence of MT. *Magnetic resonance in medicine* **67**, 979–990 (2012).

[42] Pauly, J., Nishimura, D. & Macovski, A. A k-space analysis of small-tip-angle excitation. *Journal of Magnetic Resonance 1969* **81**, 43–56 (1989).

[43] Mougin, O., Clemence, M., Peters, A., Pitiot, A. & Gowland, P. High-resolution imaging of magnetisation transfer and nuclear Overhauser effect in the human visual cortex at 7 T. *NMR in Biomedicine* **26**, 1508–1517 (2013).

[44] Mougin, O. *et al.* Imaging gray matter with concomitant null point imaging from the phase sensitive inversion recovery sequence. *Magnetic resonance in medicine* (2015).

[45] Zaiss, M. & Bachert, P. Exchange-dependent relaxation in the rotating frame for slow and intermediate exchange–modeling off-resonant spin-lock and chemical exchange saturation transfer. *NMR in Biomedicine* **26**, 507–518 (2013).

[46] Windschuh, J. *et al.* Correction of B1-inhomogeneities for relaxation-compensated CEST imaging at 7 T. *NMR in Biomedicine* **28**, 529–537 (2015).

[47] Girard, O. M. *et al.* Magnetization transfer from inhomogeneously broadened lines (ihMT): experimental optimization of saturation parameters for human brain imaging at 1.5 Tesla. *Magnetic resonance in medicine* **73**, 2111–2121 (2015).

[48] Varma, G. *et al.* Interpretation of magnetization transfer from inhomogeneously broadened lines (ihMT) in tissues as a dipolar order effect within motion restricted molecules. *Journal of Magnetic Resonance* **260**, 67–76 (2015).

Chapter 4

Chemical Exchange Saturation Transfer Effect in Blood

4.1 Introduction and Motivation

Despite the considerable recent interest in CEST [1–3], so far only one study has been published on CEST in blood [4]. *Zheng et al* investigated the feasibility of using blood as a CEST contrast agent and found that blood does have a sufficient CEST contrast relative to the surrounding tissue [4]. However, in that work the CEST signal was observed via the MTR_{asym} metric, which has been shown to be insufficient at ultra high field due to the overlapping of the NOE (at -3.5 ppm) and the APT (at 3.5 ppm) in the asymmetry spectra. Interestingly, blood shows high CEST and NOE signals, and could help in understanding the origin of the CEST and NOE effects seen in tissue.

Amide proton transfer (APT) is associated with mobile amides in close proximity to cellular cytosol and its sensitivity to changes in pH [5] has led to it being used in the assessment of ischemia [6, 7] and glioma tumour grading [8, 9]. The origin of CEST effects, and in particular APT contrast, are not fully understood, particularly the enhanced contrast in tumours which have been attributed to an increase in the content of endogenous cellular proteins and peptides, although the total content of proteins has recently been shown to be relatively constant

in tumours [10]. In previous work, we observed that *in vivo* z-spectra acquired at 7T from the superior sagittal sinus had high APT signal compared to nearby grey and white matter. Lorentzian difference maps from *in vivo* z-spectra for the amides and amines are shown in Figures 4.1(a) and 4.1(b), and highlight the high concentrations of amides and amines in the sagittal sinus compared to white matter and grey matter. Figure 4.1(c) shows the respective z-spectra for the WM, GM and SS ROIs shown in Figure 4.1(a).

This work aims to investigate and quantify the CEST and NOE signals detectable from *ex vivo* blood, considering the effects of oxygenation, haematocrit levels and cell structure on CEST and NOE signals, and to quantify the results via the AREX method [11]. We hypothesise that the lysing of red blood cells (RBC) will break down the membranes of the cells and will stop any active transfer of water through the cell membranes, as lysing breaks the aquaporins.

(a) Amides at 3.5 ppm   **(b)** Amines at 2 ppm   **(c)** Z-spectra for WM, GM and SS ROIs
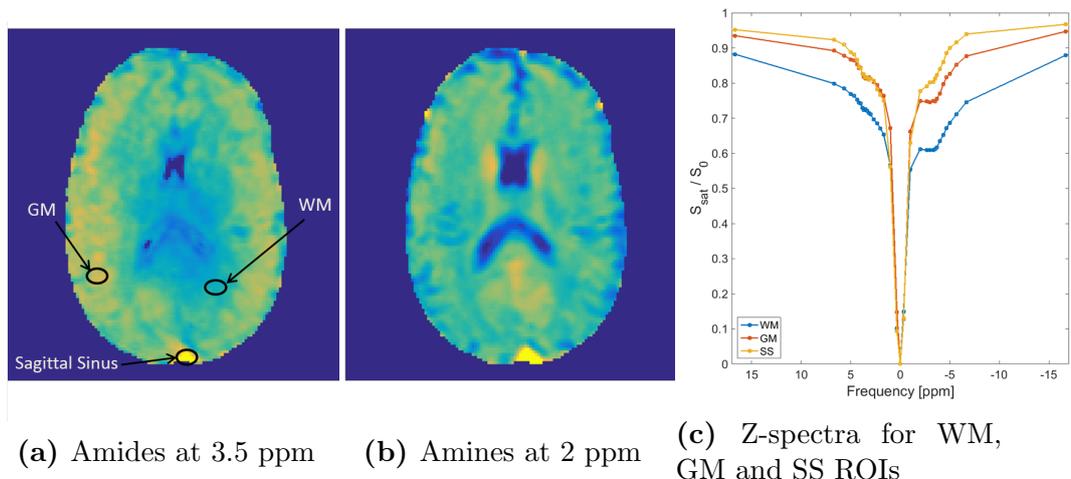
Figure 4.1: (a) Amide and (b) amine maps showing white matter (WM), grey matter (GM) and the superior sagittal sinus (SS) for $B_{1,rms} = 1$ μT. (b) The corresponding z-spectra for each ROI.

4.2 Methods

4.2.1 Blood Collection and Preparation

Following local ethical approval, 20 ml of venous blood was taken from four healthy male volunteers and stored in 4 ml heparinised blood collection tubes. The blood samples were prepared quickly so that scanning commenced within one hour, to ensure it was fresh, before being frozen and scanned within one week.

Blood Oxygenation Modulation

The oxygenation levels of two 4 ml blood samples from each volunteer were modulated immediately after the blood was collected by bubbling either 120 ml of nitrogen gas or 100% medical oxygen through the vials using a needle and syringe, to deoxygenate and oxygenate the blood respectively. The vials were regularly inverted and excess gas was removed from the sealed vials using a second needle and syringe. This process ensured good mixing, and a very low gas flow rate was used to prevent foaming [12]. A blood gas analyser (i-STAT, Abbott Point of Care) was used to measure the level of oxygen saturation (sO_2) and pH in the blood samples throughout, during one experiment. The sO_2 is a measure of the amount of oxyhaemoglobin in the blood, expressed as a fraction of the total amount of haemoglobin able to bind oxygen. A final blood sample was kept unchanged as a control sample.

Gadolinium

In one experiment the addition of Gadolinium (ProHance) was tested, with concentrations of 0.25 mM and 1 mM added to two 4 ml deoxygenated blood samples to lengthen the T_2^*.

4.2. Methods

Separating Blood

Blood is a suspension of cells dissolved in plasma. Plasma makes up approximately 55% of blood and consists of 92% water. The cells, once separated from the plasma, consist of platelets, white blood cells and red blood cells (RBCs). RBCs account for approximately 40-45% of whole blood and are a measure of the haematocrit. The ratio of cells in normal blood is 600 RBCs for each white blood cell and 40 platelets [13].

For a further blood sample (that was not oxygenatation modulated) the RBCs were extracted from the plasma by spinning it in a centrifuge. To avoid breaking the RBCs or cell membranes the blood was spun at a rate of 500 rpm for 20 minutes, yielding a sample consisting largely of concentrated RBCs with a haematocrit of approximately 80% [14], double the haematocrit of whole blood.

Lysing of Blood

Immediately after scanning, all fresh blood samples were frozen and then slowly defrosted to lyse the RBCs in the blood samples prior to repeated scanning. Lysing the cells breaks down the membrane of the RBCs. It also has the effect of stopping any active transfer of water through the cell membranes and the breaking of aquaporins [15].

Table 4.1: Overview of the blood samples used in the experiments described, and the number of preliminary and full datasets were collected.

	Fresh Blood	Lysed Blood
Oxygenated	3 Prelim & 1 Full datasets	3 Prelim & 1 Full datasets
Deoxygenated	3 Prelim & 1 Full datasets	3 Prelim & 1 Full datasets
Control	3 Prelim & 1 Full datasets	3 Prelim & 1 Full datasets
cRBCs	3 Prelim & 1 Full datasets	3 Prelim & 1 Full datasets
Deoxy + Gd	1 Prelim	-

4.2.2 MRI Acquisition

MRI experiments were conducted on a 7T Philips Achieva with a volume transmit RF coil and Nova 32 channel receive array. The blood vials were placed in a custom-made water phantom kept at a temperature of 37°C using a low temperature circulator (PMT Instruments). By rotating the phantom manually between scans before locking into position, the blood could be mixed during the experiments to remove settlement effects. The acquisition of the 58 off-resonance frequencies was paused every five dynamics ($\sim$4 mins) to allow the rotation of the water phantom to ensure that the blood did not settle. A separate experiment showed that the holder came back to its initial position after each rotation with a mean displacement of 0.01 ± 0.02 mm in the x-axis and 0.11 ± 0.05 mm in y-axis.

CEST Imaging

Each off-resonance data point on the z-spectrum was acquired using a saturation-prepared 3D-TFE sequence. The sequence consists of two parts, the saturation and the 3D-TFE readout shown in Figure 4.2. Three nominal levels of maximum RF amplitude saturation, $B_{1,sat} = 2.4$, 4.9 and 8.5 μT were achieved by applying a train of 20 Gaussian windowed sinc RF pulses with bandwidth 200 Hz and duty cycle of 50%, equivalent to $B_{1,rms} = 0.43$, 0.87 and 1.52 μT. The pulses were phase cycled and a spoiler gradient was applied at the end of the pulse train to remove the residual transverse magnetisation. The 3D-TFE readout consisted of a train of 300 gradient echoes for a FOV = $224 \times 224 \times 48$ mm^3 and $1.5 \times 1.5 \times 2$ mm^3 resolution, TE/TR/FA = 2.6 ms/5.55 ms/8° and SENSE factor (RL) = 2. The 3D volume acquisition required five repetitions of this cycle and a low-high k-space acquisition was used. The total sequence consisted of 58 off-resonance frequencies unevenly sampled between $\pm$ 17 ppm, including 50 kHz (166 ppm) for normalisation purposes.
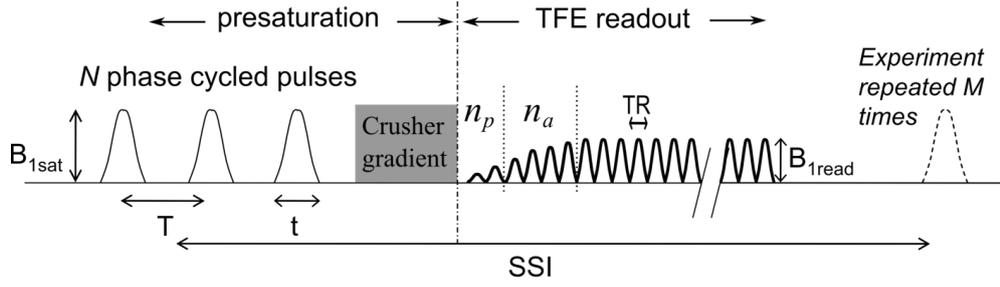
Figure 4.2: The magnetisation transfer-prepared turbo field echo (MT-TFE) sequence: presaturation period followed by the 3D-TFE readout. The presaturation period consists of $N = 20$ Gaussian windowed sinc pulses. The duty cycle of 50% was used such that $t = 30$ ms and $T = 60$ ms. The crusher gradient at the end of the saturation train removes any residual transverse magnetisation. $n_p = 2$ and $n_a = 4$ are the number of ramped RF pulses before and at the start of the acquisition, respectively. Adapted from [16].

A B_0 map (double echo) and B_1 map (dual TR method) were acquired immediately after the acquisition of the z-spectra for field inhomogeneity corrections. Both field mapping techniques used are described in Section 1.4.3 in more detail.

T_1 maps were acquired using an inversion recovery sequence for FOV = 224 $\times$ 224 $\times$ 48 mm^3 and 1.5 $\times$ 1.5 $\times$ 2 mm^3 resolution and TI = 150, 300, 500, 800, 1200, 1500, 2200, 3000, 3500, 4000, 4500 and 5000 ms, TR/TE = 6.9ms/3.2ms, and SENSE factor (RL) = 2.

T_2^* maps were acquired using a multi-gradient echo (echo=8) with FOV = 256 $\times$ 256 $\times$ 48 mm^3, 2 $\times$ 2 $\times$ 2 mm^3 resolution, TR/TE = 45/1.35 ms, and ΔTE = 1.8 ms.

4.2.3 Data-Preprocessing

Z-spectra were obtained for the 3 B_1 saturation powers by calculating the Z-value,

$$Z\left(\Delta\omega\right) = \frac{M_{z,sat}\left(\Delta\omega\right)}{M_0\left(\Delta\omega = 50\text{ kHz}\right)}, \tag{4.1}$$

at each off-resonance ($\Delta\omega$), with normalisation by M_0 at 50 kHz (166 ppm)

where it was assumed that no exchangeable magnetisation is saturated. On a voxel-by-voxel basis the z-spectra at each RF power were B_0 corrected by interpolating to 0.01 ppm resolution between $\pm$ 17 ppm, then shifting the entire spectrum by the difference between the B_0 map and the zero point at 0 ppm, and finally re-sampling back to the original off-resonance frequencies [2, 5].

B_1 Correction

Each of the z-spectra were B_1 corrected voxel-by-voxel using the three B_1 saturation powers after they were scaled to the nominal saturation powers using the B_1 maps, and an additional point for 0 μT was also included [17]. The z-spectra were interpolated between 0 μT and 1.5 μT, to estimate z-spectra for target B_1 saturations of 0.4 and 0.8 μT. The lysed concentrated RBCs blood sample's B_1 saturation field was approximately 60% of the average achieved flip angle during acquisition (according to the B_1 map) as it sat in a region of lower B_1 than the other samples, and so the target powers of 0.4 and 0.8 μT were chosen to allow the comparison of all the blood samples together, to avoid extrapolation in the B_1 correction method.

4.2.4 Quantification

T_1 and T_2^* Relaxation Times

The longitudinal T_1 relaxation time was calculated by fitting the signal acquired at the inversion times TI to a mono-exponential $M = M_0\left[1 - \alpha \exp\left(-TI/T_1\right)\right]$ where α takes account of inversion efficiency and incomplete signal recovery before the inversion. The transverse relaxation time T_2^* was calculated by fitting the 8 gradient echoes to a mono-exponential decay using a least-squares fitting algorithm.

4.2. Methods

Lorentzian Lineshape Model Fitting & AREX

To quantify CEST and NOE differences between the z-spectra, Lorentzian line-shape model fitting was performed [11], which assumes that the z-spectra could be approximated by a linear combination of Lorentzian lineshapes, corresponding to amides (at 3.5 pmm), amines (at 2.2 ppm), the NOEs at -3.5 and -1.7 ppm, and a super Lorentzian for the MT from macromolecules. The peak at -1.7 ppm was termed the aliphatic NOE, to differentiate between the two NOE signals. The Lorentzians were fitted to the B_1 corrected z-spectra using a least-squares fitting algorithm, and the fit allowed the positions of the CEST and NOE Lorentzian peaks be adjusted by $\pm$ 0.2 ppm around central resonance frequencies predicted from the literature. The amplitude and width of the Lorentzian peaks were allowed to vary to account for variable saturation powers and unknown exchange rates and proton pool sizes.

The relaxation parameters T_1 and T_2^* also affect the lineshape and amplitude of the features in the z-spectra. Using the Lorentzian lineshape fitting method, the difference in T_2^* between the oxygenated and deoxygenated blood samples were taken into account by the adjustment of the DS linewidth, and the $\pm$ 0.2 ppm allowed slight adjustment in placement of the CEST and NOE peaks relative to the water resonance. To account for changes in T_1, the AREX signal [3] was calculated,

$$AREX\left(\Delta\omega\right) = \left(\frac{1}{Z_{lab}\left(\Delta\omega\right)} - \frac{1}{Z_{ref}\left(\Delta\omega\right)}\right) \Big/ T_1, \qquad (4.2)$$

where T_1 is the observed longitudinal relaxation time. $Z_{lab}(\Delta\omega)$ is the measured Z-value (Equ. 4.1) at off-resonance frequency $\Delta\omega$ and $Z_{ref}(\Delta\omega)$ is the Z-value from the summation of all fitted Lorentzians, except the Lorentzian for the proton pool of interest at $\Delta\omega$. It is not possible to calculate AREX over the total width of the Lorentzian lineshape, as the AREX calculation breaks down when the amplitude of the z-spectrum drops to zero (generally at 0 ppm due to

the efficiency of direct water saturation). The AREX value was thus taken at the maximum peak location of the Lorentzian lineshape fitted for the CEST and NOE pools. In addition, the full width half maximums (FWHM) of the proton pools were measured, and this is important in the quantification of the amines and the aliphatic NOE that are close to the DS water peak and are confounded due to the broadening of DS.

Bloch-McConnell Fitting Model

The observed chemical exchange effects in the fresh concentrated RBCs sample were also quantified by fitting the z-spectra for the three B_1 saturation (non-B_1 corrected) using the 6-pool Bloch-McConnell model [2] which provides the pure proton concentrations, T_2s, and exchange rates of each exchanging proton pool. The model only incorporates the exchange between the proton pools: NOE, aliphatic NOE, amides, amines and MT and free water, and assumes that direct exchange between the other pools is negligible. The model was free to fit for the concentration M_0^i/M_0^f, T_2^i and exchange rate k_{ex}^i of the proton i pools. In total there were 162 off-resonance frequencies across the three z-spectra fitted, and the model searched for the best combination of M_0^i/M_0^f, T_2^i and k_{ex}^i parameters for each off-resonance in turn, until a set of parameters could fit for every off-resonance frequency in the three z-spectra, within the tolerance of the fit. The fitting took several days to complete, so only the fresh concentrated RBCs were fitted due to their highest concentrations of CEST and NOE effects, and the results were used to validate the AREX results.

Using the obtained parameters from the 6-pool Bloch-McConnell model fit, z-spectra were simulated for a range of free water T_1s between 0.2-2.2 seconds to account for the change in T_1 observed between the fresh and the lysed concentrated RBCs blood samples at the target B_1 saturation powers (0.4μT and 0.8μT). The simulated z-spectra were then fitted with the Lorentzian lineshape fitting algorithm, and the simulated AREX for each of the proton pools were

calculated. These simulated AREX were then compared to the acquired *ex vivo* AREX results to check for agreement.

4.3 Results

4.3.1 B_1 Correction

The z-spectra from all the blood samples were B_1 corrected to compare and quantify the CEST and NOE effects occurring at the same saturation power. Figure 4.3 shows the non-linear variations of the CEST and NOE signals in the concentrated RBCs as a function of the target B_1 saturation power. For the results presented in this chapter, the B_1 target saturation powers of 0.4 and 0.8 μT were used to avoid any extrapolation.
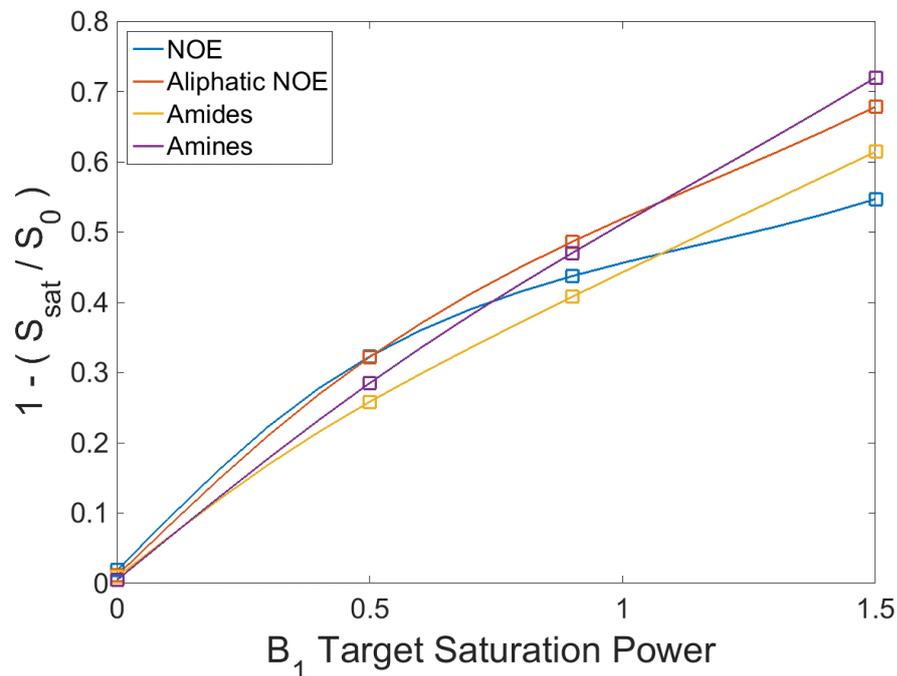
Figure 4.3: Mean MTR for NOEs, amides and amines at the maximum peak amplitude of each fitted proton pool Lorentzian for target B_1 saturation powers between 0.1 μT and 1.5 μT for the fresh concentrated RBCs blood sample. The square points indicate the acquired data points in the z-spectra used in the correction, plus the fixed data point at 0μT.

4.3.2 Oxygenation Effects on T_1 and T_2^* for Fresh and Lysed Blood

The saturation of oxygen (sO_2) and pH were measured for the oxygenated, deoxygenated and control blood samples in the first experiment and are shown in Figure 4.4. The sO_2 of the oxygenated blood post gas modulation reached 100% and maintained this level for the duration of the experiments. The sO_2 of deoxygenated blood was approximately 45% sO_2 for fresh blood and fell to 25% after lysing. The fresh control blood samples increased in sO_2 from 60% to 90% over the course of the experiment and stayed this level post-lysing. The pH dropped by ~ 0.3 throughout the experiments for all the blood samples.
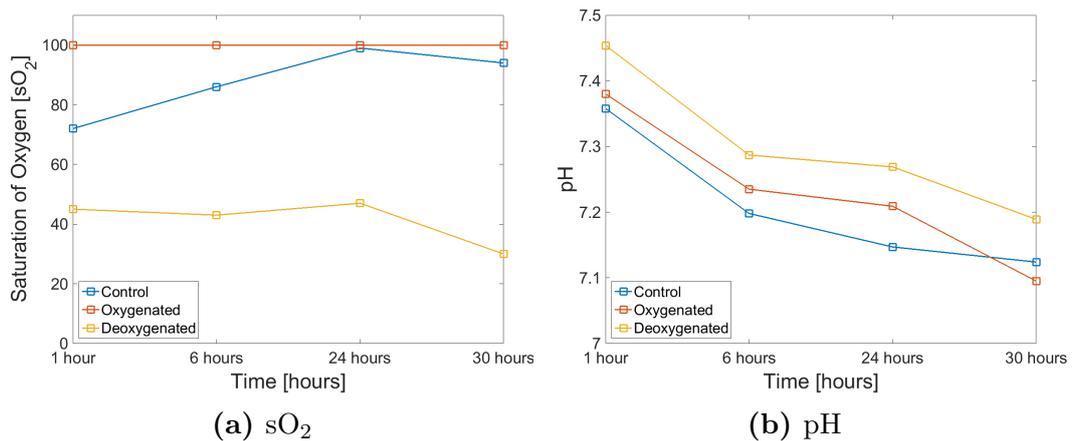
Figure 4.4: The (a) saturation of oxygen (sO_2) and (b) pH of oxygenated, deoxygenated and control blood samples.

The longitudinal T_1 and transverse T_2^* relaxation times measured for the fresh and lysed blood samples are shown in Tables 4.2 & 4.3 respectively. The T_1 times of the fresh whole blood samples were similar to the T_1 of GM at 7T [18]. Lysing the blood shortened the T_1, by approximately a half for fresh whole blood T_1s, two-thirds for the fresh concentrated RBCs T_1, and the plasma sample T_1 did not change after freezing.

The T_2^* of the deoxygenated blood was approximately five times shorter than that of the oxygenated and control blood samples. The concentrated RBCs had

a slightly shorter T_2^* than the oxygenated and control blood, and the plasma had a much longer T_2^* than all the other samples. Post-lysing, the T_2^* for the whole blood samples and concentrated RBCs increased in all cases, with the oxygenated blood having the longest T_2^* of all the blood samples. The T_2^* of the plasma sample after freezing remained above 200 ms.

Table 4.2: The T_1 and T_2^* relaxation times for fresh oxygenated, deoxygenated, control, concentrated RBCs and plasma blood samples.

Fresh Blood	Oxy	Deoxy	Control	cRBCs	Plasma
T_1 [ms]	1703 ± 23	1827 ± 93	1993 ± 51	1479 ± 26	2615 ± 75
T_2^* [ms]	32 ± 3	6 ± 1	33 ± 4	24 ± 4	254 ± 12

Table 4.3: The T_1 and T_2^* relaxation times for lysed oxygenated, deoxygenated, control, concentrated RBCs and plasma blood samples.

Lysed Blood	Oxy	Deoxy	Control	cRBCs	Plasma
T_1 [ms]	831 ± 36	640 ± 22	846 ± 31	549 ± 35	2622 ± 65
T_2^* [ms]	53 ± 7	45 ± 4	44 ± 6	43 ± 3	219 ± 17

4.3.3 Concentrated RBCs and Plasma Z-Spectra

The z-spectra (not B_1 corrected) for the concentrated RBCs and the plasma were examined and are shown in Figure 4.5 for $B_{1,rms}$ saturation powers of 0.43, 0.87 and 1.52 μT. The longer T_2^* of plasma (Table 4.2) can be observed in the z-spectra as a narrower lineshape around 0 ppm. These plots indicate that the largest source of the MT, CEST and NOE signal in the blood is from the RBCs rather than the plasma.
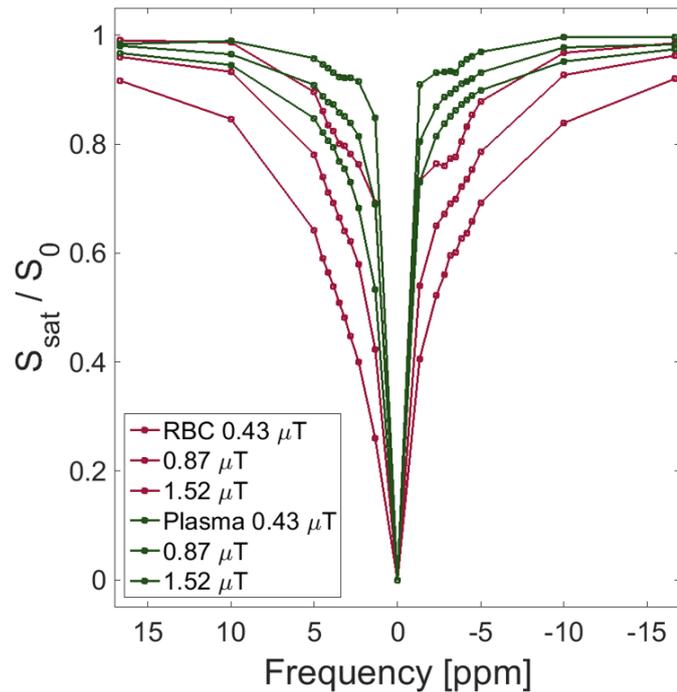
Figure 4.5: Z-spectra obtained for the concentrated RBCs and plasma blood samples for $B_{1,rms}$ saturation powers of 0.43, 0.87 and 1.52 μT.

4.3.4 Oxygenation Effects on Z-spectra for Fresh and Lysed Blood

The z-spectra after B_0 and B_1 correction for the fresh and lysed oxygenated and deoxygenated blood are shown in Figure 4.6. There is no obvious difference in NOE and CEST peaks between the fresh oxygenated and deoxygenated blood. The only observed difference between the oxygenated and deoxygenated z-spectra was the wider DS linewidth of the deoxygenated blood which is expected due to the shorter T_2^*. Post-lysing, the differences in z-spectra between the oxygenated and deoxygenated blood (Figure 4.6(b)) can be explained by the significantly faster T_1 recovery of the lysed deoxygenated blood.

(a) Fresh Blood   **(b)** Lysed Blood
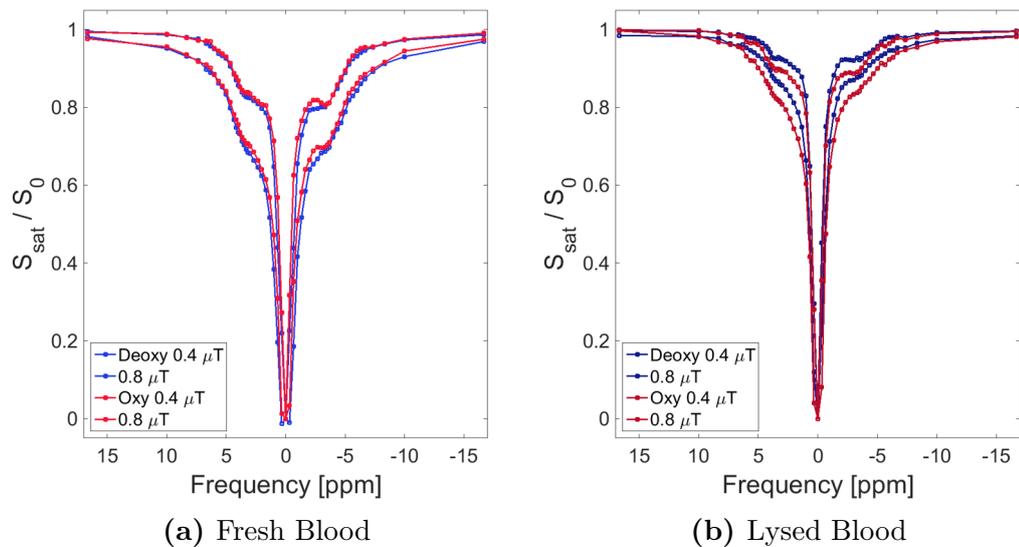
Figure 4.6: Z-spectra for the oxygenated and deoxygenated (a) fresh and (b) lysed blood for target B_1 powers of 0.4 and 0.8 μT.

Addition of Gadolinium

The broadened DS linewidth of deoxygenated blood had a detrimental effect on the quantification of the amines and aliphatic NOE. The addition of Gadolinium results in increased T_2^* times, as the mismatch in local field gradients between the RBCs and plasma reduces, and eventually plateaus (at $\sim$1 mM concentrations) where the gradient fields match [19]. Figure 4.7 shows that the effect of the Gadolinium lengthened the T_2^* to bring it to the same order of magnitude as the T_2^* of the oxygenated sample, which resulted in the z-spectrum lineshape becoming narrower. However, there is also an apparent loss of MT and baseline signal due to the shortening of T_1 of the blood samples ($T_1 = 791 \pm 10$ s and 300 ± 5 s for the 0.25 mM and 1 mM deoxygenated blood samples respectively). The recovery of the signal was very fast, however the NOE and CEST signals appeared less affected by the change in T_1. Therefore the addition of Gadolinium could be used to probe the compartmental T_1s by slowing the water exchange rate to observe whether the NOE and CEST are in fast exchange.
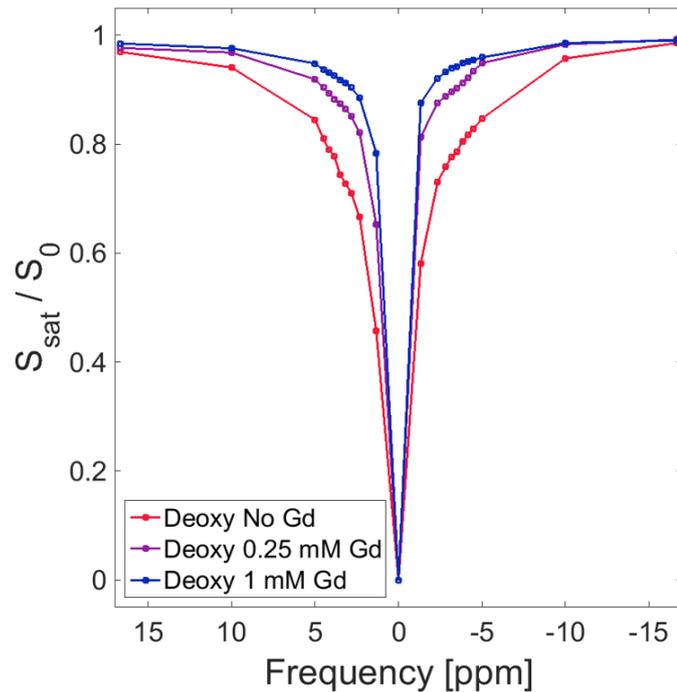
Figure 4.7: Z-spectra obtained in experiments for the deoxygenated blood with 0.25 mM and 1 mM of Gadolinium (ProHance) for $B_{1,rms}$ saturation power of 0.87 μT.

4.3.5 Fresh and Lysed Blood Z-spectra for the Concentrated RBCs

The z-spectra (after B_0 and B_1 correction) for the fresh and lysed concentrated RBCs are shown in Figure 4.8(a) and it is clear that there are less observed MT, NOE and CEST effects in the concentrated RBCs after lysing. The T_1 for the lysed concentrated RBCs was shorter which could account for the reduced observed magnetisation transfer but the NOE and CEST appear less affected. Figure 4.8(b) shows the z-spectra for the fresh concentrated RBCs and control blood, both of which should have the same oxygenation level. It is noticeable that the CEST and NOE peaks are more visible in the concentrated RBCs sample, when compared to the oxygenated whole blood sample.
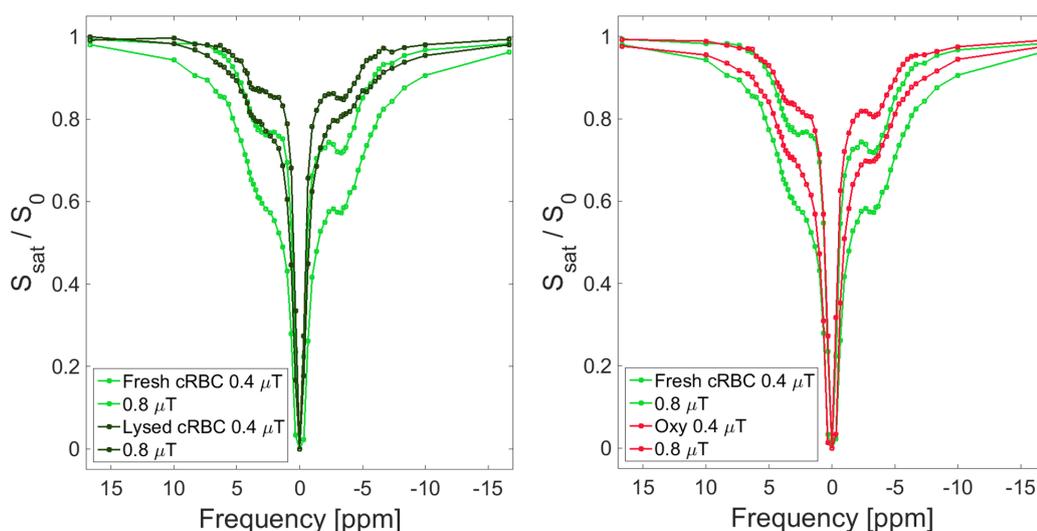
(a) Fresh & lysed concentrated RBCs blood samples **(b)** Concentrated RBCs and oxygenated blood samples

Figure 4.8: Z-spectra for the (a) the fresh and lysed concentrated RBCs, (b) the fresh concentrated RBCs and fresh oxygenated blood samples.

4.3.6 Quantification

The Lorentzian lineshape model fitting results are shown in Figure 4.9 for the (a) oxygenated, (b) deoxygenated and (c) concentrated RBCs for the B_1 corrected target saturation power of 0.8 μT. The fitting was very good with less than 1% difference between the B_1 corrected z-spectra and the Lorentzian fit for all of the blood samples. The amine peak at 2.2 ppm and the aliphatic NOE at -1.7 ppm in the deoxygenated blood in Figure 4.9(b) are clearly affected by the short T_2^* and the broadening of the DS linewidth. These fitted Lorentzian lineshapes were subsequently used for AREX quantification.

Figure 4.10 shows the AREX value for the (a) NOE, (b) aliphatic NOE, (c) amides and (d) amines at each of the central off-resonance frequencies of the proton pools and the full-width half maximum (FWHM) of the Lorentzian fitted peaks for just (e) aliphatic NOE and (f) amines that are affected by the broad DS linewidth, which has potentially impacted the measurement of the amines and aliphatic NOE in deoxygenated blood.

(a) Oxygenated   **(b)** Deoxygenated   **(c)** Concentrated RBCs
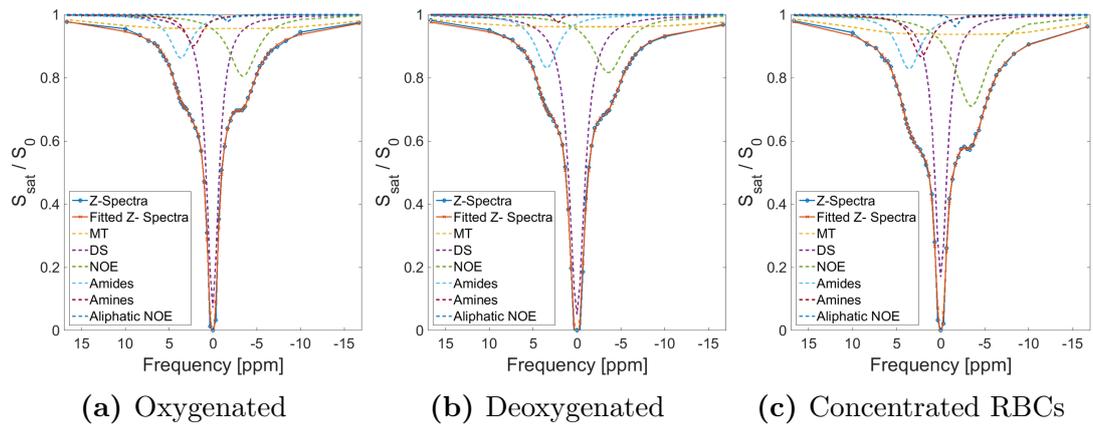
Figure 4.9: The Lorentzian lineshape fitting for DS, MT, amides, amines, NOE and aliphatic NOE for (a) oxygenated (b) deoxygenated blood and (c) the concentrated RBCs for B_1 corrected saturation power 0.8 μT.

The NOE AREX (at -3.5 ppm) for all blood samples increased with B_1 power, and there was no significant change with oxygenation levels of the whole blood samples. Comparing the concentrated RBCs sample with the oxygenated, de-oxygenated and control blood samples (the latter of which has the same oxygenation level as the concentrated RBCs as both were not oxygenation modulated), it is apparent that there is approximately double the NOE AREX which correlates to the increase in haematocrit.

The aliphatic NOE AREX results in Figure 4.10(b) show that the signal increases with the oxygenation level of the whole blood, but as already discussed, deoxygenated blood has a shorter T_2^* which results in the broadening of the DS lineshape. The DS signal dominates over the aliphatic NOE, due to its close proximity to 0 ppm, and therefore in this case the Lorentzian lineshape fitting model struggles to fit even a narrow Lorentzian for the aliphatic NOE (Figure 4.9(b)), confounding the AREX results for the deoxygenated blood. The oxygenated blood with a longer T_2^* has a narrower DS lineshape and the aliphatic NOE Lorentzian is fitted better in the Lorentzain model fit (Figure 4.9(a)). However, the aliphatic NOE AREX decreases with B_1 saturation power for both the fresh and lysed oxygenated blood samples, which is the opposite of what is observed in the concentrated RBCs. This can be explained by the broadening of

(a) NOE at -3.5 ppm

(b) Aliphatic NOE at -1.7 ppm

(c) Amides at 3.5 ppm

(d) Amines at 2.2 ppm

(e) Aliphatic NOE FWHM

(f) Amines FWHM
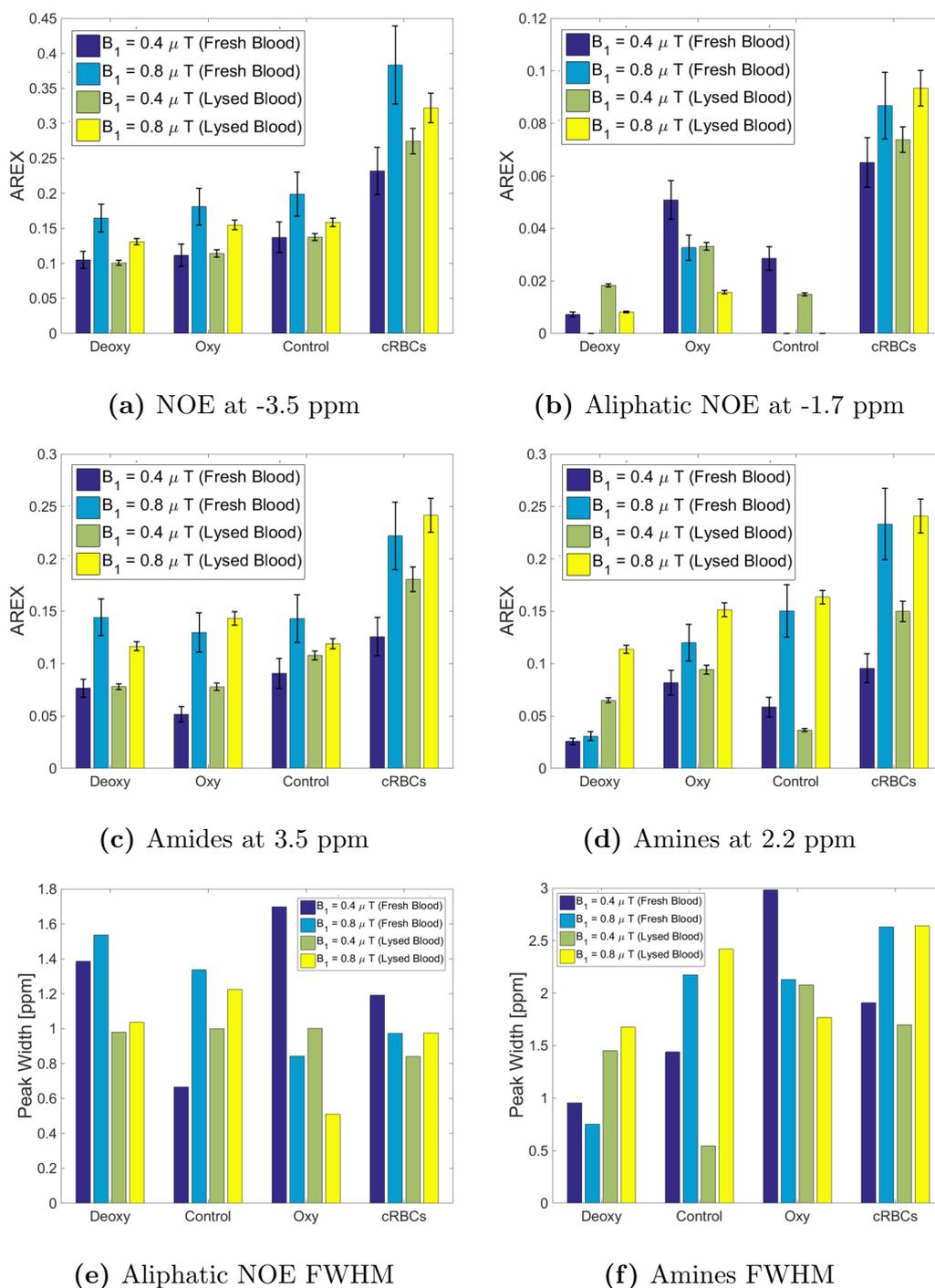
Figure 4.10: (a) NOE AREX, (b) aliphatic NOE AREX, (c) amides AREX and (d) amines AREX and (e & f). The full width half maximums of the fitted Lorentzian for aliphatic NOE and amines respectively, for the 0.4 and 0.8 μT target B_1 saturation powers for both the fresh and lysed deoxygenated, oxygenated, control and concentrated RBCs blood samples.

the DS lineshape with increased B_1 saturation power causing the Lorentzian fitting model to struggle to fit a narrow Lorentzian. The aliphatic NOE AREX has increased signal in the concentrated RBCs sample. However, the Lorentzain fitting model struggles to fit a narrow Lorentzian for the aliphatic NOE, in whole blood samples due to the lower concentration. Therefore it is not possible to say whether the AREX has doubled for the concentrated RBCs, like the NOE at -3.5 ppm.

The amide proton transfer AREX in Figure 4.10(c) for the oxygenated, de-oxygenated and control blood samples do not differ significantly, and increased amides AREX are observed for higher B_1 saturation powers, as expected [20]. Again, there was an increase in detected amides in the fresh concentrated RBCs compared to the whole blood sample, which indicates that the exchanging labile protons that result in the amide signal are mainly from the cells. Upon lysing, there is little change in the calculated AREX, indicating that lysing has little effect on amide protons exchange.

The amines (at 2.2 ppm) are in faster exchange than the amides and require more B_1 saturation power to observe the magnetisation transfer of the exchanging protons. This effect is seen in Figure 4.10(d), where for all the blood samples the measured amine AREX increases in all of the samples with higher saturation power, and the amount of amine signal roughly doubles between the whole blood and concentrated RBCs samples. As for the aliphatic NOE, the measured amine AREX for the deoxygenated blood is significantly lower as the broadened DS lineshape confounds the fitting of the amine Lorentzian, due to its close proximity to the water frequency. The fitted Lorentzian for the fresh deoxygenated blood is shown in Figure 4.9(b), and comparing the fit to the oxygenated and concentrated RBCs fits in Figures 4.9(a) and 4.9(c) respectively, it can be seen that the Lorentzian lineshape model struggles to fit Lorentzians for the amines and aliphatic NOE due to the short T_2^* that results in the boarding of the DS. This effect causes the FWHM of the amines peak shown in Figure 4.10(f) for

4.3. Results

the fresh deoxygenated blood (for both saturation powers) to be approximately half that of the oxygenated, control and the concentrated RBCs FWHMs.

Bloch-McConnell Model Fitting

The *ex vivo* non-B_1 corrected fresh concentrated RBCs z-spectra (square points) for the B_1 saturation powers of 0.43, 0.87 and 1.52 μT are shown in Figure 4.11, along with the fitted z-spectra (solid line) from the 6-pool Bloch-McConnell simulation. The concentration, exchange rate and T_2 parameters for each of the proton pools that the Bloch-McConnell model used to simulate the z-spectra, seen in Figure 4.11, are shown in Table 4.4.
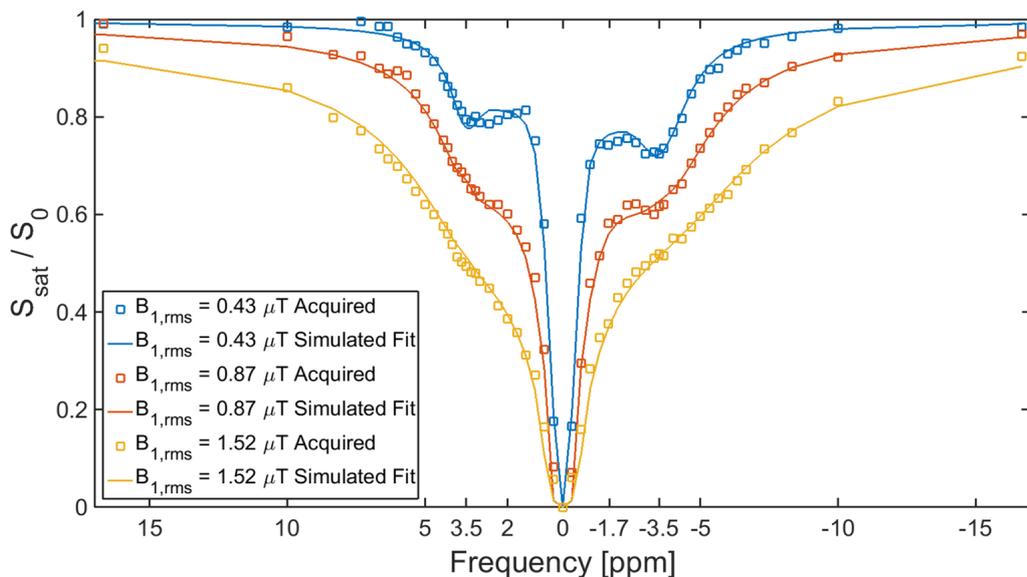
Figure 4.11: The *ex vivo* and the Bloch McConnell fitted z-spectra for the fresh concentrated RBCs for $B_{1,rms}$ saturation powers of 0.43, 0.87 and 1.52 μT.

Validating AREX

The AREX values for different T_1s of the free water pool for the NOE, aliphatic NOE, amides and amines are shown in Figure 4.12, and illustrate that for T_1s between one and two seconds, which the T_1s for healthy WM and GM fall between, the AREX is stable (i.e. remains unchanged for variations in T_1) for each pro-

4.3. Results

Table 4.4: The proton pool concentrations (M_0^i/M_0), exchange rate (k_i) and the transverse relaxation time (T_2^i) for each of the exchanging i proton pools in the fresh concentrated RBCs

Parameters	MT	Amides	Amines	NOE	Aliphatic NOE
Chemical Shift	-2.3 ppm	3.5 ppm	2.2 ppm	-3.5 ppm	-1.7 ppm
M_0^i/M_0	1.1 %	1.8 %	0.9 %	3.4 %	2.3 %
k_i	41 Hz	10 Hz	138 Hz	5 Hz	10 Hz
T_2^i	4.4 μs	2.7 ms	0.5 ms	1.0 ms	1.3 ms
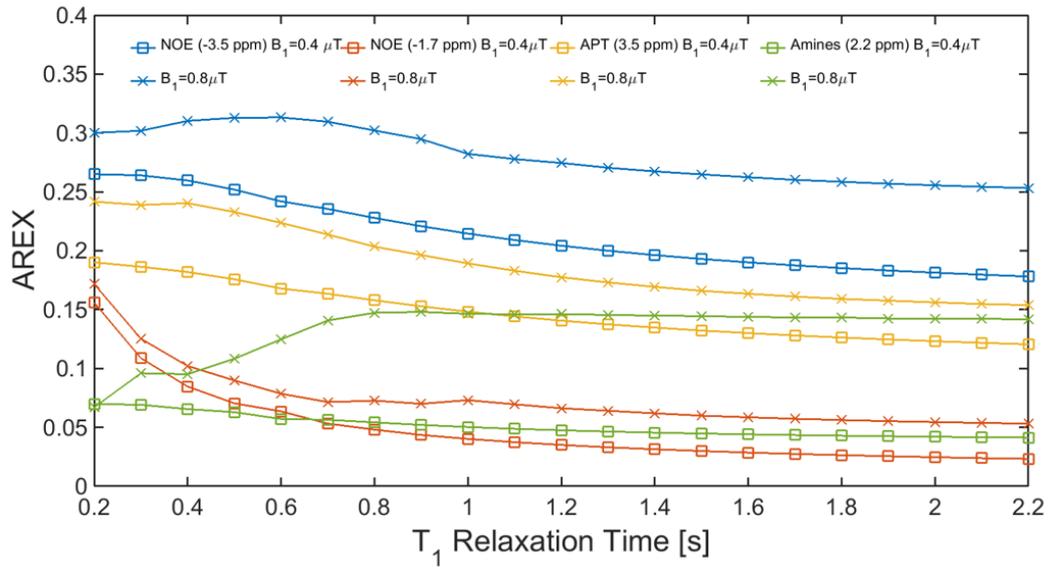
Figure 4.12: The simulated AREX values over a range of T_1 between 0.2s to 2.2s for the NOE, aliphatic NOE, amides and amines. The Lorentzian lineshape model fit used on the *ex vivo* blood samples, was applied to simulated concentrated RBCs z-spectra for $B_{1,rms} = 0.4$ & 0.8 μT. The simulated z-spectra had the parameters found in Table 4.4

ton pool. However, when the T_1 of free water falls below one second the AREX signal for the proton pools, particularly the aliphatic NOE and amines, which are close to the water frequency, become unstable and their AREX results are not in agreement. Figure 4.13 shows the comparison of the acquired *ex vivo* and simulated NOE, aliphatic NOE, amides and amines AREXs for the concentrated RBCs. The acquired and simulated amide AREXs for both the fresh and lysed concentrated RBCs are agreeable due to the similarity in calculated values for the Lorentzian lineshape model fitting. However, the comparison of the NOE at

high power suggests that the AREX results could be misleading. The acquired and simulated aliphatic NOE and amines AREXs are contradictory and place doubt on the calculated *ex vivo* AREX results.
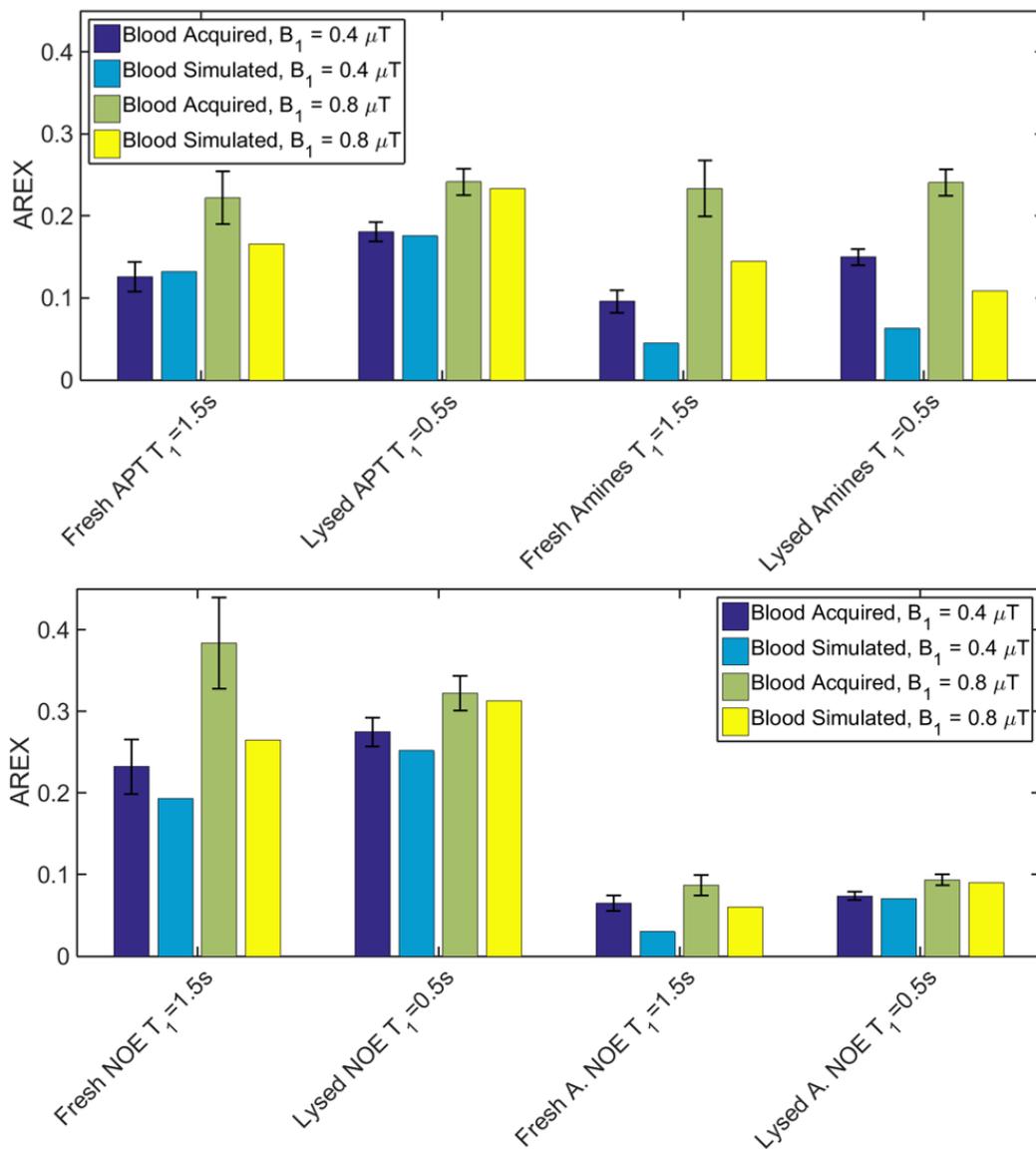
Figure 4.13: The *ex vivo* acquired AREXs for the NOE, aliphatic NOE, amides and amines are compared to the simulated AREXs for the proton pools, from a Lorentzian lineshape fitting model applied to a 6-pool Bloch-McConnell using the exchange rates, T_2s and concentrations for the concentrated RBCs (Table 4.4).

4.4 Discussion

Human blood produces a significant amount of CEST and NOE, which does not appear to be dependent upon the level of blood oxygenation. More significantly, the amides, amines and NOE signals originate from the RBCs within the blood as the proton pool AREXs increased for blood samples with a higher percentage of haematocrit/cells. Furthermore, there is no significant change in the measured AREX of the amides, amines and NOE effects upon the lysing of the blood.

The variations in the B_1 transmit field at 7T, discussed in Chapter 3, result in the blood samples placed in the water phantom having different B_1 saturation. The CEST, NOE and MT effects do not scale linearly with B_1 and their maximum effects occur at different B_1 saturation powers [20]. Therefore to allow the comparison and quantification, the z-spectra were B_1 corrected using spline interpolation that was successfully used to correct for B_1 field inhomogenties at 7T [17].

Deoxygenated blood is highly paramagnetic, compared to oxygenated blood that is diamagnetic. In absence of oxygen, the haemoglobin becomes highly paramagnetic, resulting in local macroscopic magnetic field gradients [21]. As a result T_2^* of deoxygenated blood ($\sim$5 ms) is shorter than oxygenated blood (Table 4.2) and the resultant water proton lineshape broadens, and has also been reported to shift upfield by 0.48 ppm [22]. The z-spectra collected for oxygenated and deoxygenated blood, Figure 4.6(a), clearly show that for the B_1 corrected saturation powers, the DS lineshape around 0 ppm broadens as expected, for a shorter T_2^*, but there is no other noticeable difference between the oxygenated and deoxygenated blood. The T_1s for oxygenated and deoxygenated blood are similar in magnitude with no noticeable difference observed between the z-spectra obtained. Gadolinium was used to lengthen the T_2^* of the deoxygenated blood and resulted in narrowing the DS lineshape around the central water frequency. Gadolinium also decreased the T_1 which resulted in quicker signal recovery, al-

though the CEST and NOE effects appeared less affected by the faster T_1 recovery in the z-spectra. Gadolinium is confined to the plasma in the extracellular space [23]. As already discussed, the main source of the NOE and CEST signal is from the concentrated RBCs and not the plasma, and therefore the addition of Gadolinium may affect the signal exchanging within them to a lesser degree. Further experiments could be undertaken to determine if the CEST and NOE signals relate to contents of the cell membrane.

The NOE AREX at -3.5 ppm showed little difference between the oxygenated, deoxygenated and control blood samples indicating that the oxygen that binds to the haemoglobin does not influence the chemical exchange processes observed. The source of NOE signal visible at -3.5 ppm is currently debatable but is believed to be a combination of direct dipole-dipole interactions and exchanged relayed interactions [24, 25]. This is further supported by the z-spectra of plasma for the three saturation powers in Figure 4.5 which show that there was no notable NOE contribution from the plasma itself. The aliphatic NOE at -1.7 ppm is more difficult to quantify due to the narrow lineshape and its close proximity to the DS line around 0 ppm. The lineshape broadens with higher saturation power and shortened T_2^* and results in little to zero aliphatic NOE AREX in the deoxygenated blood sample being observed. The narrower DS lineshape of the oxygenated blood allows more accurate measurement of the aliphatic NOE.

Focusing on the amides and amines at 3.5 and 2.2 ppm respectively, there is again little significant difference between oxygenated, deoxygenated and control blood samples. The changes in pH of the blood samples were measured with a blood gas analyser throughout the course of the first experiment and a drop in pH of 0.2-0.3 for all the blood samples was detected. Reported exchange rate of the amides (and indeed to amines but to a lesser extent) are dependent upon the pH level [5] and therefore a drop in pH would account for a reduced amount of APT. However, the AREX results for the amides and amines (Figures 4.10(c) and

4.4. Discussion

4.10(d) do not seem to indicate significantly that this is the case, although the change in pH is small. For the amides, the AREX increases with B_1 saturation power as expected [20], and for deoxygenated blood samples the amines AREX was confounded, like the aliphatic NOE, due to broadened DS linewidth. To allow the quantification of the amines in the deoxygenated blood, Gadolinium could be added to bring the T_2^* into line with the oxygenated blood.

The only apparent difference between the fresh oxygenated and deoxygenated z-spectra (Figure 4.6(a)) is the DS lineshape. Upon lysing, the T_2^* difference between the oxygenated and deoxygenated blood significantly decreases as the deoxygenated T_2^* becomes similar to the T_2^* of the oxygenated sample. This can be explained by the fact that the lysing breaks the red blood cell membranes which then flood the extracellular water, which in turn reduces the local field gradients that generate the rapid T_2^* in deoxygenated blood. The T_1 of deoxygenated blood is shorter than oxygenated blood, which is expected given the negative linear dependence with percentage of O_2 [26]. The T_1 of plasma is similar to CSF and has a longer T_1 than whole blood and the concentrated RBCs. Post lysing, deoxygenated blood has a shorter T_1 than that of oxygenated and control blood samples, which could be due to the creation of a single compartment containing the paramagnetic ions, rather than two exchanging compartments that exist within cells.

Bloch-McConnell Fitting Model

The results for the fresh concentrated RBCs in Table 4.4 show that the NOE signals at -1.7 and -3.5 ppm are highest in amplitude, which for the aliphatic NOE at -1.7 ppm constricts the AREX result shown in Figure 4.10(b). Also the amide and amine AREX results suggest that they have similar concentrations (Figures 4.10(c) and 4.10(d)) which also contradicts the Bloch-McConnell fitting results.

For future blood experiments, we will quantify all the CEST and NOE effects

4.4. Discussion

using Bloch-McConnell model fitting which can, unlike AREX, account for effects overlapping 0 ppm and the non-linear T_1 effects seen in the blood z-spectra. Also beneficial is that the *ex vivo* z-spectra given to the Bloch McConnell fitting model do not have to be B_1 corrected, as the fitting model can account for the variation in B_1 saturation for each z-spectrum individually. However, given the time constraints, the fitted parameters (Table 4.4) were used to validate the AREX results.

The choice of quantification metrics used to isolate the CEST and NOE effects from other saturation effects (previously discussed in Section 3.7) depends upon the experimental setting. As the T_1 relaxation time of all the blood samples varied, this had to be taken into account in the measurement of CEST and NOE signal and AREX does this. However, in a recent simulation and rat tumour study by *Heo et. al* in which they compared MTR_{LD}, MTR_{Rex} and AREX, they showed that MTR_{Rex} and AREX both revealed substantially more CEST signal at higher B_1 saturation power than MTR_{LD} at 3T & 4.7T. Also, for B_0 field strengths of 3T, 4.7T, 7T and 9.4T, higher MTR_{Rex} and AREX were recorded around the water frequency because of the small denominators in Equ. 4.2. Given the reported variance in AREX shown by *Heo et.al.* and in the disparity seen between the full Bloch-McConnell fit and AREX results, the acquired *ex vivo* blood AREX results were compared to a Bloch-McConnell 6-pool simulated fit for the concentrated RBCs to check for agreement between the results.

The NOE and amides AREX, for both the fresh and lysed concentrated RBCs, are in agreement with the simulated AREXs, although at higher power the NOE does differ somewhat, which was reported by *Heo et.al.*. The aliphatic NOE and amines, acquired and simulated AREXs are not in agreement for both the fresh and lysed concentrated RBCs, which was also reported by *Heo et. al.*, and the Lorentzian fitting model and AREX quantification give inaccurate results close to the direct water saturation [27].

Given the present differences between the simulated and *ex vivo* AREX results for variations in the T_1, it is hard to fully quantify the CEST and NOE effects between the fresh and lysed blood. So in the future, the Bloch-McConnell model fitting will be used to quantify the CEST and NOE effects between the fresh and lysed blood samples as it can deal with the non-linear T_1 variations that occur. Also now that the T_2 and k_{ex} of the exchanging proton pools have been approximately found, the future blood z-spectra fits can have exchange rate k_{ex} and T_2 fixed, and thus speed up the fitting process.

4.4.1 Further Experiments

The large concentration of CEST and NOE effects in the blood means that there is still a lot more to investigate.

Field Strength

At higher fields, such as 9.4 T, the DS lineshape is narrower for the same B_1 saturation allowing better quantification of the aliphatic NOE and amines. Previous work assessing the origins of chemical exchange saturation transfer at 9.4T [28] found that in rat brains, the aliphatic NOE at -1.7 ppm was reduced upon the growth of a glioma tumour, which the study of blood could help explain.

However, the CEST and NOE effects in blood should also be studied at 3T as the clinical benefit is greater. For example, organs like the placenta contain large amounts of blood and CEST could be used to examine the complex processes taking place here.

Clotted Blood

The development of CEST in pathological studies, has a potential future, as a biomarker for disease or illness. A recent study by *Zhang et al*, examined a 'NOE

mediated MT effect' around -1.6 ppm and observed a strong contrast difference between healthy and stoke tissue in rats [29] and this could be explained by active blood concentration in the tissue. The next blood experiments should investigate the change in CEST signals once the blood has clotted. If there is a measurable difference in CEST signal there is potential to develop the technique to monitor stroke tissue.

pH

The role of pH and its effect on CEST contrast imaging, particular in tumours, has made it an active area of research. Tumour intracellular pH is more alkaline compared to normal tissue [30], however many studies have assumed a constant exchange rate and associated increased CEST contrast to the increased content of mobile cytosolic proteins and peptides [31–33]. This has been contradicted by other recent studies which show no difference in the total protein content, and only a marginal increase in the tumour cytosolic protein content that was found previously [10, 28]. Modulating the pH of *ex vivo* blood to different conditions could help in understanding the role of pH and its effect on the CEST and NOE effects observed *in vivo*.

4.5   Conclusion

The work presented in this chapter indicates that the main source of the NOE, amides and amines is from the cells within the blood and that the plasma does not contribute to the CEST effects. Neither the oxygenation level of blood nor lysing affect the CEST and NOE signals. There has been some doubt cast on the non-linear T_1 effect on the AREX result of the lysed blood, when the T_1 falls below one second for the proton pools in close proximity to the water frequency. Quantification using the Bloch-McConnell equations removes the doubt cast and will be used in future but the process is time-consuming.

Bibliography

[1] van Zijl, P. & Yadav, N. N. Chemical exchange saturation transfer (CEST): what is in a name and what isn't? *Magnetic resonance in medicine* **65**, 927–948 (2011).

[2] Zaiss, M. & Bachert, P. Chemical exchange saturation transfer (CEST) and MR Z-spectroscopy in vivo: a review of theoretical approaches and methods. *Physics in medicine and biology* **58**, R221 (2013).

[3] Zaiss, M. *et al.* Relaxation-compensated CEST-MRI of the human brain at 7T: unbiased insight into NOE and amide signal changes in human glioblastoma. *Neuroimage* **112**, 180–188 (2015).

[4] Zheng, S. *et al.* Chemical exchange saturation transfer effect in blood. *Magnetic resonance in medicine* **71**, 1082–1092 (2014).

[5] Zhou, J., Payen, J.-F., Wilson, D. A., Traystman, R. J. & van Zijl, P. C. Using the amide proton signals of intracellular proteins and peptides to detect pH effects in MRI. *Nature medicine* **9**, 1085–1090 (2003).

[6] Tietze, A. *et al.* Assessment of ischemic penumbra in patients with hyperacute stroke using amide proton transfer (APT) chemical exchange saturation transfer (CEST) MRI. *NMR in Biomedicine* **27**, 163–174 (2014).

[7] Sun, P. Z., Cheung, J. S., Wang, E. & Lo, E. H. Association between pH-weighted endogenous amide proton chemical exchange saturation transfer MRI and tissue lactic acidosis during acute ischemic stroke. *Journal of Cerebral Blood Flow & Metabolism* **31**, 1743–1750 (2011).

[8] Sagiyama, K. *et al.* In vivo chemical exchange saturation transfer imaging allows early detection of a therapeutic response in glioblastoma. *Proceedings of the National Academy of Sciences* **111**, 4542–4547 (2014).

Bibliography

[9] Scheidegger, R., Wong, E. T. & Alsop, D. C. Contributors to contrast between glioma and brain tissue in chemical exchange saturation transfer sensitive imaging at 3Tesla. *Neuroimage* **99**, 256–268 (2014).

[10] Yan, K. *et al.* Assessing amide proton transfer (APT) MRI contrast origins in 9 L gliosarcoma in the rat brain using proteomic analysis. *Molecular Imaging and Biology* **17**, 479–487 (2015).

[11] Zaiss, M., Schmitt, B. & Bachert, P. Quantitative separation of CEST effect from magnetization transfer and spillover effects by Lorentzian-line-fit analysis of z-spectra. *Journal of magnetic resonance* **211**, 149–155 (2011).

[12] Gardener, A. G., Francis, S. T., Prior, M., Peters, A. & Gowland, P. A. Dependence of blood R2 relaxivity on CPMG echo-spacing at 2.35 and 7 T. *Magnetic resonance in medicine* **64**, 967–974 (2010).

[13] Tortora, G. J. & Grabowski, S. R. Principles of Anatomy and Physiology. Ninth.

[14] Hanson, M. S. *et al.* Phosphodiesterase 3 is present in rabbit and human erythrocytes and its inhibition potentiates iloprost-induced increases in cAMP. *American Journal of Physiology-Heart and Circulatory Physiology* **295**, H786–H793 (2008).

[15] Kuchel, P. W. & Benga, G. Why does the mammalian red blood cell have aquaporins? *Biosystems* **82**, 189–196 (2005).

[16] Mougin, O., Clemence, M., Peters, A., Pitiot, A. & Gowland, P. High-resolution imaging of magnetisation transfer and nuclear Overhauser effect in the human visual cortex at 7 T. *NMR in Biomedicine* **26**, 1508–1517 (2013).

[17] Windschuh, J. *et al.* Correction of B1-inhomogeneities for relaxation-compensated CEST imaging at 7 T. *NMR in Biomedicine* **28**, 529–537 (2015).

Bibliography

[18] Wright, P. *et al.* Water proton T1 measurements in brain tissue at 7, 3, and 1.5 T using IR-EPI, IR-TSE, and MPRAGE: results and optimization. *Magnetic Resonance Materials in Physics, Biology and Medicine* **21**, 121–130 (2008).

[19] Blockley, N. *et al.* Field strength dependence of R1 and R 2* relaxivities of human whole blood to prohance, vasovist, and deoxyhemoglobin. *Magnetic resonance in medicine* **60**, 1313–1320 (2008).

[20] Jones, C. K. *et al.* In vivo three-dimensional whole-brain pulsed steady-state chemical exchange saturation transfer at 7 T. *Magnetic resonance in medicine* **67**, 1579–1589 (2012).

[21] Weisskoff, R. M. & Kiihne, S. MRI susceptometry: Image-based measurement of absolute susceptibility of MR contrast agents and human blood. *Magnetic Resonance in Medicine* **24**, 375–383 (1992).

[22] Gasparovic, C. & Matwiyoff, N. A. The magnetic properties and water dynamics of the red blood cell: A study by proton-NMR lineshape analysis. *Magnetic resonance in medicine* **26**, 274–299 (1992).

[23] Koenig, S. H., Spiller, M., Brown, R. D. & Wolf, G. L. Relaxation of water protons in the intra-and extracellular regions of blood containing Gd (DTPA). *Magnetic resonance in medicine* **3**, 791–795 (1986).

[24] Jin, T., Wang, P., Zong, X. & Kim, S.-G. MR imaging of the amide-proton transfer effect and the pH-insensitive nuclear overhauser effect at 9.4 T. *Magnetic resonance in medicine* **69**, 760–770 (2013).

[25] Jones, C. K. *et al.* Nuclear Overhauser enhancement (NOE) imaging in the human brain at 7T. *Neuroimage* **77**, 114–124 (2013).

[26] d'Othée, B. J., Rachmuth, G., Munasinghe, J. & Lang, E. V. The effect of hyperoxygenation on T1 relaxation time in vitro 1. *Academic radiology* **10**, 854–860 (2003).

Bibliography

[27] Heo, H.-Y. *et al.* Insight into the quantitative metrics of chemical exchange saturation transfer (CEST) imaging. *Magnetic resonance in medicine* (2016).

[28] Xu, J. *et al.* On the origins of chemical exchange saturation transfer (CEST) contrast in tumors at 9.4 T. *NMR in biomedicine* **27**, 406–416 (2014).

[29] Zhang, X.-Y. *et al.* A new NOE-mediated MT signal at around- 1.6 ppm for detecting ischemic stroke in rat brain. *Magnetic resonance imaging* **34**, 1100–1106 (2016).

[30] Griffiths, J. Are cancer cells acidic? *British journal of cancer* **64**, 425 (1991).

[31] Zhou, J. *et al.* Practical data acquisition method for human brain tumor amide proton transfer (APT) imaging. *Magnetic resonance in medicine* **60**, 842–849 (2008).

[32] Zhou, J. *et al.* Differentiation between glioma and radiation necrosis using molecular magnetic resonance imaging of endogenous proteins and peptides. *Nature medicine* **17**, 130–134 (2011).

[33] Zhou, J., Lal, B., Wilson, D. A., Laterra, J. & van Zijl, P. Amide proton transfer (APT) contrast for imaging of brain tumors. *Magnetic resonance in medicine* **50**, 1120–1126 (2003).

Conclusion

The work presented in this thesis investigates the chemical exchange and magnetisation transfer effects seen in CEST experiments *in vivo* and in human blood *ex vivo* at ultra high field.

Ultra high field MRI is hampered by the spatially varying B_1 transmit field, and in Chapter 2, two methods of alleviating the inhomogeneities in the B_1 field are presented. First, two set of dielectric pads are used to improve the B_1 transmit field in the small regions of interest, where typically the B_1 is low. The dielectric pads can improve the signal by up to 200% in MPRAGE images in the peripheral regions, such as the cerebellum and temporal lobes. Multi-transmit technology has also seen a development in RF pulse design methods to improve the B_1 transmit field, and a simulation study in Chapter 2 shows that the flip angle variation across a transverse slice can be reduced by 50% by using a slice-selective sequence with five RF spokes instead of a conventional slice-selective pulse. Eight channel multi-transmit technology is now available at ultra high field, and has the ability to further improve the B_1 field through shimming methods which were outlined and discussed in Chapter 2.

The visualisation and quantification of chemical exchange processing observed in CEST contrast imaging are affected by the magnetisation transfer from macro-molecules. The design of dual-frequency RF saturation pulses presented in Chapter 3, show that they successfully suppress the MT contribution in z-spectra in both the white and grey matter, enhancing detection of the NOE and CEST peaks, and also reveal a NOE peak around -2 ppm which was previously masked by the MT. The dual-frequency saturation pulses could also be used to probe cross-relaxation chemical exchange effects if the location of the fixed saturation, used to suppress the MT, is moved to 3.2 ppm.

The work presented in Chapter 4 indicates that the main source of the NOE,

amides and amines is from the cells within the blood and that the plasma does not contribute to the CEST effects. The CEST and NOE proton pools are also unaffected by the oxygenation level of the blood or by lysing. Non-linear T_1 effects around the central water frequency impact upon the AREX result of the lysed blood, and quantification using the Bloch-McConnell equations removes the doubt cast by the AREX, and will be used in the future. However, the process is time-consuming. The CEST and NOE effects in the blood have only been investigated for differing oxygenation, haematocrit levels, and cell structure. The CEST effects observed under different physiological conditions such as pH and clotting still require further investigation.